



University of HUDDERSFIELD

University of Huddersfield Repository

Thornton, Roger D.

Atomistic simulation of green rust, its structure, composition and potential in nuclear waste storage and reprocessing.

Original Citation

Thornton, Roger D. (2022) Atomistic simulation of green rust, its structure, composition and potential in nuclear waste storage and reprocessing. Doctoral thesis, University of Huddersfield.

This version is available at <http://eprints.hud.ac.uk/id/eprint/35717/>

The University Repository is a digital collection of the research output of the University, available on Open Access. Copyright and Moral Rights for the items on this site are retained by the individual author and/or other copyright owners. Users may access full items free of charge; copies of full text items generally can be reproduced, displayed or performed and given to third parties in any format or medium for personal research or study, educational or not-for-profit purposes without prior permission or charge, provided:

- The authors, title and full bibliographic details is credited in any copy;
- A hyperlink and/or URL is included for the original metadata page; and
- The content is not changed in any way.

For more information, including our policy and submission procedure, please contact the Repository Team at: E.mailbox@hud.ac.uk.

<http://eprints.hud.ac.uk/>

ATOMISTIC SIMULATION OF GREEN RUST,
ITS STRUCTURE, COMPOSITION AND
POTENTIAL IN NUCLEAR WASTE STORAGE
AND REPROCESSING.

Author:

Roger D. Thornton

A thesis submitted to the University of Huddersfield for
the degree of Doctor of Philosophy

February 2022



University of
HUDDERSFIELD

Copyright statement

- i. The author of this thesis (including any appendices and/or schedules to this thesis) owns any copyright in it (the “Copyright”) and s/he has given The University of Huddersfield the right to use such copyright for any administrative, promotional, educational and/or teaching purposes.
- ii. Copies of this thesis, either in full or in extracts, may be made only in accordance with the regulations of the University Library. Details of these regulations may be obtained from the Librarian. This page must form part of any such copies made.
- iii. The ownership of any patents, designs, trademarks and any and all other intellectual property rights except for the Copyright (the “Intellectual Property Rights”) and any reproductions of copyright works, for example graphs and tables (“Reproductions”), which may be described in this thesis, may not be owned by the author and may be owned by third parties. Such Intellectual Property Rights and Reproductions cannot and must not be made available for use without the prior written permission of the owner(s) of the relevant Intellectual Property Rights and/or Reproductions

Abstract

The aim of this thesis is to use computer simulation techniques to model the bulk structure and low index Miller surfaces of green rust 1 and green rust 2, along with uranyl minerals which could form in the interlayers of green rust, and thus provide a potential mechanism to sequester uranium from polluted groundwater in the environment. The intention is that transferable potential models be developed that can be used in further studies or alternative works.

In Chapter 1 the historic use of nuclear material and its subsequent reprocessing and storage is introduced. The aqueous contamination of groundwater by uranium is discussed, changing the oxidation state of the uranyl ion is examined and possible methods of remediation are investigated. Laboratory synthesis of green rust is reviewed along with the techniques used in experimentally determining the structure of green rust. The natural occurrence of green rust is explained and potential uses of the material are described, with a discussion of the difficulties involved in working with green rust; this leads on to a review of the benefits of computer simulation at an atomistic level, and the drawbacks associated with such techniques. Finally the questions which drive the objectives of this work are stated.

Chapters 2 and 3 discuss the methodologies applied in this work and describe the theory behind them. Chapter 2 introduces computational modelling techniques and the theoretical methods which underpin them; the use of the potential model, which is key to this work, is described in detail. Energy minimisation and molecular dynamics are the theoretical methods used in this thesis and they are described in Chapter 3. Chapter 3 also introduces

surfaces, which are critical in the aims of this work, and describes different methods of surface energy calculation.

Chapter 4 describes the work on testing and refining the interatomic potential models for $\text{Fe}(\text{OH})_2$ and goethite. While $\text{Fe}(\text{OH})_2$ has few experimentally reported structures, the ones which are documented were reproduced with excellent results using the potential model; the potential model outperformed density functional theory (DFT) in its ability to match the structural parameters of the cell. Five low index Miller surfaces of $\text{Fe}(\text{OH})_2$ were modelled and the (0 0 1) proved to be the most stable. The potentials were then used in similar modelling of goethite; again the potential model was able to better reproduce experimentally determined structures than was the DFT model, with cell dimensions within 1% of reported structures. This demonstrated the viability of the potential sets to be used interchangeably in modelling larger systems and that sophisticated fitting procedures were not necessary.

Chapter 5 documents the work on atomistic modelling of uranyl minerals. The need for a reliable set of interatomic potentials for a range of uranyl minerals is introduced. Existing potentials are fitted to known mineral structures from the International Crystal Structural Database (ICSD) and compared to the results of DFT calculations; the methods used to develop these potentials are described in detail. Results show that the set of potentials produced are capable of working successfully and that these potentials can be validated by reference to empirical data or DFT calculations.

In Chapter 6 the potentials developed in Chapters 4 and 5 are developed further and used to model one example of each of green rust 1 and green

rust 2. It was shown that sulfate green rust 2 could successfully be modelled using interatomic potentials and that the sulfate group, with respect to the oxygen atoms, takes up a tridentate orientation toward the hydroxide layer. Modelling low index Miller surfaces of sulfate green rust 1 showed the (0 0 1) surface to be the most stable of those modelled. The bulk structure of chloride green rust 1 was modelled without water in the interlayers but when water was added there was some dissociation of the H atoms from the hydroxide layers; resolution of this dissociation and progression to surface modelling was prevented by the research period coming to an end.

Lastly, Chapter 7 summarises the results presented in this thesis and the conclusions that can be drawn, with a suggestion of further work that could be carried out built upon these results and the potentials developed therein.

Acknowledgements

I would firstly like to thank my supervisor Dr David Cooke for all his support and guidance; his willingness to help, always with patience and good humour, has been invaluable.

I gratefully acknowledge the School of Applied Sciences at the University of Huddersfield for funding this work and the HPC-RG at the university for the provision of computer time. Additionally, via our membership of the UK's HEC Materials Chemistry Consortium, which is funded by EPSRC (EP/L000202), this work used the ARCHER UK National Supercomputing Service (<http://www.archer.ac.uk>). Via our membership of the UK's HEC Materials Chemistry Consortium, which is funded by EPSRC (EP/L000202), this work used the UK Materials and Molecular Modelling Hub for computational resources, MMM Hub, which is partially funded by EPSRC (EP/P020194).

Contents

1	Introduction	33
2	Theoretical Methods and Computational Techniques	50
2.1	Periodic Boundary Conditions	51
2.2	Electronic Structure Calculations	52
2.2.1	Density Functional Theory	54
2.2.2	Kohn-Sham Equations	62
2.2.3	K-point Sampling	63
2.2.4	Plane Wave Basis Sets and Pseudopotentials	64
2.3	The Potential Model - Theory and Derivation	65
2.4	The Born Model of Ionic Solids	67
2.5	Coulombic Summation	70
2.5.1	Ewald Summation	70
2.5.2	Smooth Particle Mesh Ewald Summation	77
2.6	Parry Summation	77
2.7	Short-range Potentials	78
2.8	Intramolecular Interactions	82
2.8.1	Bonding Interactions	82
2.8.2	Three-Body Potentials	85
2.8.3	Four-Body Potentials	86
2.9	Polarisability	86
2.9.1	The Shell Model	87
3	Energy Minimisation	89

3.1	Energy Minimisation	90
3.1.1	Conjugate Gradients	90
3.1.2	Newton-Raphson Method	93
3.2	Molecular Dynamics	95
3.2.1	Integration Algorithms	98
3.2.2	Ensembles	103
3.3	Surfaces	111
3.3.1	Mineral Surface Types	111
3.3.2	Surface Energy Calculations - Two-dimensional Ap- proach	115
3.3.3	Surface Energy Calculations - Three-dimensional Ap- proach	117
4	Iron (II) Hydroxide and Goethite	119
4.1	Iron (II) Hydroxide Crystal Structure	119
4.2	Iron (II) Hydroxide Surfaces	128
4.3	Goethite Crystal Structure	137
4.4	Goethite Surfaces	143
4.5	Conclusions	153
5	Uranyl Minerals	155
5.1	Methodology	156
5.1.1	Development of Potentials	157
5.1.2	Example: Uranyl Chloride	159
5.2	Results	170
5.2.1	Uranyl Chloride	170

5.2.2	Uranyl Carbonate	172
5.2.3	Uranyl Iron Oxide	177
5.2.4	Uranyl Hydroxide	180
5.2.5	Uranyl sulfate	184
5.3	Water and UO_2^{2+}	188
5.4	Conclusions	207
6	Modelling Green Rust 1 and 2 Using DFT and Interatomic Potentials	210
6.1	Green Rust 2	210
6.1.1	Green Rust 2 Surfaces	235
6.2	Green Rust 1	240
6.3	Conclusions	260
7	Conclusions	262

List of Figures

1	Contaminant movement through groundwater at the Sellafield site ^[8]	36
2	Structure and stacking arrangement of green rust 1 (a) and green rust 2 (b) ^[30]	39
3	Image of a typical LDH ^[51]	41
4	Microscope image of green rust ^[53]	42
5	Chart of length-scale vs. simulation techniques ^[82]	50
6	Illustration of the periodic boundary condition principle ^[83]	51
7	Schematic of LDA in two dimensions ^[91]	58
8	Schematic of local and semi-local density approximation by LDA and GGA ^[91]	60
9	Comparison of a wavefunction in the Coulomb potential of the nucleus (blue) to the one in the pseudopotential (red). The real and the pseudo wavefunction and potentials match above a certain cut-off radius, r_c	65
10	Fourier transformation summation ^[118]	71
11	The Lennard-Jones potential ^[122]	79
12	Harmonic oscillator curve of energy versus interatomic distance; in a true vibration system the lowest energy the bond can have is $E_0 = \frac{1}{2}h\nu$	83
13	Comparison of energy versus interatomic distance curves for the harmonic oscillator and the Morse potential	85

14	Representation of the shell model. (a) shows an unpolarised ion where the centre of the core and the shell are at the same point. (b) shows a polarised ion where an asymmetric field causes the core and shell to be centred on different points.	87
15	Implementation of the Verlet scheme, showing the successive steps in the method	101
16	Verlet leapfrog velocity sampling ^[142]	103
17	The three types of stacking surface described by Tasker ^[151]	112
18	Scanning electron microscope image showing faceting of the polar (1 1 1) MgO surface to produce neutral (1 0 0) surfaces ^[152]	113
19	Schematic showing how faceting produces a non-polar surface . . .	113
20	Type 3 surface reconstructed to remove the dipole ^[154]	114
21	Schematic representation of the two-region approach used by METADISE for surfaces and interfaces ^[84]	115
22	Layered double hydroxide typical structure. In the a and b directions are planes of Fe(OH) ₂ , in the c direction the structure is dominated by weaker hydrogen bonds from the OH groups in the gaps between the layers.	120
23	Schematic of a hexagonal Bravais lattice, where $a = b \neq c$ and $\alpha = \beta = 90^\circ$ and $\gamma = 120^\circ$	121
24	Graphical representation of convergence testing for the bulk structure of Fe(OH) ₂	123
25	Fe(OH) ₂ (0 0 1) surface, perpendicular to lattice vector a, generated from CLAYFF potentials. The spacing between the layers of Fe is 4.63 Å	135

26	Fe(OH) ₂ (0 1 1) surface, perpendicular to lattice vector a, generated from CLAYFF potentials. The spacing between the layers of Fe is 4.97 Å	136
27	Fe(OH) ₂ (0 0 1) surface, perpendicular to lattice vector a, generated from DFT. The spacing between the layers of Fe is 4.57 Å	136
28	Fe(OH) ₂ (0 1 1) surface, perpendicular to lattice vector a, generated from DFT. The spacing between the layers of Fe is 4.90 Å	137
29	Goethite structure. The planes of Fe are linked by bonds to oxygen atoms. Weaker hydrogen bonds from the OH groups are present in the structure.	138
30	Schematic of an orthorhombic Bravais lattice, where $a \neq b \neq c$ and $\alpha = \beta = \gamma = 90^\circ$. An orthorhombic lattice may be either primitive or centred in one of three different ways: C-face centred, body-centred, or all-face centred	139
31	Graphical representation of convergence testing for the bulk structure of goethite	142
32	Goethite (0 0 1) surface, perpendicular to lattice vector a, generated from CLAYFF potentials. The spacing between the Fe atoms in adjacent layers is 3.46 Å	152
33	Goethite (0 0 1), perpendicular to lattice vector a, surface generated from DFT. The spacing between the Fe atoms in adjacent layers is 3.11 Å	153

34	Uranyl chloride, UO_2Cl_2 , $a = 5.725\text{\AA}$, $b = 8.409\text{\AA}$, $c = 8.720\text{\AA}$ $\alpha = \beta = \gamma = 90^\circ$	160
35	Graph of recast Buckingham potential for Cl-Cl as a Lennard-Jones 12-6 potential	163
36	Uranyl carbonate, UO_2CO_3 , $a = 4.840\text{\AA}$, $b = 9.273\text{\AA}$, $c = 4.298\text{\AA}$ $\alpha = \beta = \gamma = 90^\circ$	172
37	Uranyl iron oxide, UO_2FeO_2 , $a = 4.888\text{\AA}$, $b = 11.937\text{\AA}$, $c = 5.110\text{\AA}$ $\alpha = \beta = \gamma = 90^\circ$	177
38	Uranyl hydroxide, $\text{UO}_2(\text{OH})_2$, $a = 5.644\text{\AA}$, $b = 6.287\text{\AA}$, $c = 9.937\text{\AA}$ $\alpha = \beta = \gamma = 90^\circ$	180
39	Uranyl sulfate, UO_2SO_4 , $a = 6.760\text{\AA}$, $b = 5.711\text{\AA}$, $c = 12.824\text{\AA}$ $\alpha = \gamma = 90^\circ$, $\beta = 102.91^\circ$	185
40	TIP3P water model at 300K.	192
41	Uranyl ion at 300K. The U—O bond length is 1.81\AA	193
42	The U—O radial distribution function for a Uranyl ion in water using the potential parameters of Guilbaud and Wipff with a charge of $+2.5 e$ on the central uranium ion. $g(r)$ (solid line) is the RDF, $n(r)$ (dotted line) is the integrated value showing the number of water molecules	195
43	The change in free energy as a water molecule approaches the hydration layer of the uranyl ion	197
44	The change in free energy as a water molecule approaches the hydration layer of the uranyl ion	198

45	Uranyl ion in water at 300K, showing four coordinated water molecules and an exchange of the fifth coordinated water molecule (adjacent water molecules removed for clarity). Potentials as Guilbaud and Wipff.	199
46	The U—O radial distribution function for a Uranyl ion in water using the potential parameters of Rai <i>et al</i> with a charge of +2.0 <i>e</i> on the central uranium ion. $g(r)$ (solid line) is the RDF, $n(r)$ (dotted line) is the integrated value showing the number of water molecules	203
47	The change in free energy as a water molecule approaches the hydration layer of the uranyl ion	204
48	The change in free energy as a water molecule approaches the hydration layer of the uranyl ion	205
49	Uranyl ion in water at 300K, showing four coordinated water molecules and, where the bond is elongated, an exchange of the fifth coordinated water molecule (adjacent water molecules removed for clarity). Potentials as Rai <i>et al</i>	206
50	Projection of the lattice of sulfate GR2 on the (0 0 1) plane ^[214] .	212
51	General view of the ordered representation of the crystal structure of sulfate GR2 ^[214]	213
52	Projection along the (1 1 0) plane of sulfate GR2 showing sulfate tetrahedrons orientated down toward Fe^{3+} ^[219]	214
53	Layered double hydroxysulfate, $(Fe_2^{2+} Fe^{3+})(OH)_6(SO_4)_{0.5}(H_2O)_{3.85}$ ^[219]	216
54	sulfate GR2 from DFT calculation from monodentate orientation, showing sulfate tetrahedron orientation towards hydroxide layer .	218

55	sulfate GR2 with water, from DFT calculation	221
56	sulfate green rust with tridentate oxygen orientation toward hydroxide layer	225
57	sulfate green rust with tridentate oxygen orientation toward hydroxide layer, with H-H derived from 9-6 potential	230
58	sulfate green rust with tridentate oxygen orientation toward hydroxide layer, with H-H derived from 9-6 potential and water added	234
59	sulfate green rust bulk structure from (1 0 0) surface	236
60	sulfate green rust (1 0 0) surface structure	237
61	sulfate green rust bulk structure from (0 0 1) surface	238
62	sulfate green rust (0 0 1) surface structure	239
63	Crystal structure of chloride GR1. (a) Stacking sequence. (b) Disposition of chloride ions and water molecules in interlayer, viewed along (0 0 1) One interlayer, one OH ⁻ and one Fe layer below shown. ^[224]	241
64	<i>E</i> -pH equilibrium diagram of the system Fe/chloride containing solution at 25°C for an activity $\alpha[\text{Cl}^-] = 0.55$, corresponding to a 1 M KCl solution ^[226] . Chloride GR1 was taken at Fe ₄ (OH) ₈ Cl · nH ₂ O ^[224]	243
65	Crystal structure of chloride GR1 from DFT, with 2 chloride ions.	244
66	Crystal structure of chloride GR1 from DFT, with 3 chloride ions.	245
67	Crystal structure of chloride GR1 using modified CLAYFF potentials, with 3 chloride ions.	248
68	Chloride GR1 with oxygen atom positions refined in METADISE, without potentials.	251

69	Chloride GR1 with oxygen and hydrogen atom positions refined in METADISE, without potentials.	252
70	Crystal structure of Chloride GR1 from DFT, with 3 chloride ions and water added.	253
71	Crystal structure of Chloride GR1 with water, showing H dissociation and Fe layer distortion.	258
72	Crystal structure of Chloride GR1 with water, with fixed cell dimensions.	259

List of Tables

1	Fe(OH) ₂ experimentally determined cell parameters ^[162]	121
2	Fe(OH) ₂ convergence testing of DFT calculations	122
3	Fe(OH) ₂ experimentally determined cell parameters compared to DFT modelling results (experimental: $a = b \neq c$ and $\alpha = \beta \neq \gamma$)	124
4	Partial charges (q_u) on ions used in the testing and development of interatomic potentials for Fe(OH) ₂ , CLAYFF potentials	124
5	Lennard-Jones potentials for Fe(OH) ₂ , CLAYFF potentials	125
6	Harmonic potentials for Fe(OH) ₂ , CLAYFF potentials	125
7	Partial charges (q_u) on ions used in the testing and development of interatomic potentials for Fe(OH) ₂ , based on the shell model of Lewis and Catlow	125
8	Buckingham potentials for Fe(OH) ₂ , based on the shell model of Lewis and Catlow	126
9	Morse potentials for Fe(OH) ₂ , based on the shell model of Lewis and Catlow	126
10	Harmonic potentials for Fe(OH) ₂ , based on the shell model of Lewis and Catlow	126
11	Partial charges (q_u) on ions used in the testing and development of interatomic potentials for Fe(OH) ₂ , based on the rigid ion model of Baram and Parker	127
12	Lennard-Jones potentials for Fe(OH) ₂ , based on the rigid ion model of Baram and Parker	127

13	Morse potentials for $\text{Fe}(\text{OH})_2$, based on the rigid ion model of Baram and Parker	127
14	$\text{Fe}(\text{OH})_2$ experimentally determined cell parameters compared to interatomic potential modelling results (experimental: $a = b \neq c$ and $\alpha = \beta \neq \gamma$)	128
15	Vacuum gap convergence testing for the low index Miller surfaces of $\text{Fe}(\text{OH})_2$	129
16	Region 1 thickness convergence testing for the (0 0 1) Miller surface of $\text{Fe}(\text{OH})_2$	131
17	Region 1 DFT thickness convergence testing for the (0 1 0) Miller surface of $\text{Fe}(\text{OH})_2$	131
18	Region 1 DFT thickness convergence testing for the (0 1 1) Miller surface of $\text{Fe}(\text{OH})_2$	132
19	Region 1 DFT thickness convergence testing for the (1 1 0) Miller surface of $\text{Fe}(\text{OH})_2$	132
20	Region 1 DFT thickness convergence testing for the (1 1 1) Miller surface of $\text{Fe}(\text{OH})_2$	133
21	Surface energy trend comparison for the low index Miller surfaces of $\text{Fe}(\text{OH})_2$. Figures in square brackets represent the lowest to highest energy trends within each set of results.	134
22	Goethite (α - FeOOH) experimentally determined cell parameters ^[166]	
	140	

23	Goethite experimentally determined cell parameters compared to DFT modelling results, for amended and unamended Hubbard d values, using PBE_pseudo_D potentials (experimental: $a \neq b \neq c$ and $\alpha = \beta = \gamma$)	141
24	Goethite convergence testing of DFT calculations	141
25	Goethite experimentally determined cell parameters compared to interatomic potential modelling results (experimental: $a \neq b \neq c$ and $\alpha = \beta = \gamma$)	143
26	Vacuum gap convergence testing for the low index Miller surfaces of goethite	145
27	Region 1 DFT thickness convergence testing for the (0 0 1) Miller surface of goethite	146
28	Region 1 DFT thickness convergence testing for the (0 1 0) Miller surface of goethite	146
29	Region 1 DFT thickness convergence testing for the (0 1 1) Miller surface of goethite	147
30	Region 1 DFT thickness convergence testing for the (1 1 0) Miller surface of goethite	147
31	Region 1 DFT thickness convergence testing for the (1 1 1) Miller surface of goethite	148
32	Region 1 DFT thickness convergence testing for the (1 0 0) Miller surface of goethite	148
33	Region 1 DFT thickness convergence testing for the (1 0 1) Miller surface of goethite	149

34	Surface energy trend comparison for the low index Miller surfaces of goethite. Figures in square brackets represent the lowest to highest energy trends within each set of results	150
35	Surface energy ratio comparison for the low index Miller surfaces of goethite. Figures in square brackets represent the lowest to highest energy trends within each set of results	151
36	Nonbond Parameters for the CLAYFF Force Field	160
37	Lennard-Jones 12-6 parameters, with CLAYFF chloride potential	161
38	Buckingham Potentials - Spagnoli <i>et al</i>	162
39	Lennard-Jones 12-6 parameters, revised with chloride potentials from Spagnoli <i>et al</i>	163
40	Buckingham potential parameters	165
41	Buckingham potential parameters	169
42	Partial charges (q_u) on ions used in the testing and development of interatomic potentials	170
43	UO ₂ Cl ₂ simulation results comparing experimental data with results generated from CASTEP (DFT) and GULP (using interatomic potentials)	171
44	Partial charges (q_u) on ions used in the testing and development of interatomic potentials	173
45	Lennard-Jones potentials for UO ₂ CO ₃	173
46	Buckingham potentials for UO ₂ CO ₃	174
47	Morse potentials for UO ₂ CO ₃	174
48	Harmonic potentials for UO ₂ CO ₃	174
49	Three-body potentials for UO ₂ CO ₃	175

50	Four-body potentials for UO_2CO_3	175
51	UO_2CO_3 simulation results comparing experimental data with results generated from CASTEP (DFT) and GULP (using interatomic potentials)	176
52	Partial charges (q_u) on ions used in the testing and development of interatomic potentials	178
53	Buckingham potentials for UO_2FeO_2	178
54	UO_2FeO_2 simulation results comparing experimental data with results generated from CASTEP (DFT) and GULP (using interatomic potentials)	179
55	Partial charges (q_u) on ions used in the testing and development of interatomic potentials	181
56	Lennard-Jones potentials for $\text{UO}_2(\text{OH})_2$	182
57	Buckingham potentials for $\text{UO}_2(\text{OH})_2$	183
58	Morse potentials for $\text{UO}_2(\text{OH})_2$	183
59	Harmonic potentials for $\text{UO}_2(\text{OH})_2$	183
60	Three-body potentials for $\text{UO}_2(\text{OH})_2$	184
61	$\text{UO}_2(\text{OH})_2$ simulation results comparing experimental data with results generated from CASTEP (DFT) and GULP (using interatomic potentials)	184
62	Partial charges (q_u) on ions used in the testing and development of interatomic potentials	186
63	Lennard-Jones potentials for UO_2SO_4	186
64	Harmonic potentials for UO_2SO_4	187
65	Three-body potentials for UO_2SO_4	187

66	UO ₂ SO ₄ simulation results comparing experimental data with results generated from CASTEP (DFT) and GULP (using interatomic potentials)	188
67	Partial charges (q_u) on ions used in molecular dynamics modelling of the uranyl ion in water, using potentials as Guilbaud and Wipff ^[192]	190
68	Lennard-Jones potentials used in molecular dynamics modelling of the uranyl ion in water, using potentials as Guilbaud and Wipff ^[192]	191
69	Harmonic potentials used in molecular dynamics modelling of the uranyl ion in water, using potentials as Guilbaud and Wipff ^[192]	191
70	Three-body potentials used in molecular dynamics modelling of the uranyl ion in water, using potentials as Guilbaud and Wipff ^[192]	192
71	Varied partial charges (q_u) on uranyl ion used in molecular dynamics modelling of the uranyl ion in water, using potentials as Guilbaud and Wipff ^[192]	194
72	Partial charges (q_u) on ions used in molecular dynamics modelling of the uranyl ion in water, using potentials as Rai <i>et al</i> ^[209]	200
73	Lennard-Jones potentials used in molecular dynamics modelling of the uranyl ion in water, using potentials as Rai <i>et al</i> ^[209]	200
74	Harmonic potentials used in molecular dynamics modelling of the uranyl ion in water, using potentials as Rai <i>et al</i> ^[209]	201
75	Three-body potentials used in molecular dynamics modelling of the uranyl ion in water, using potentials as Rai <i>et al</i> ^[209]	201

76	Varied partial charges (q_u) on uranyl ion used in molecular dynamics modelling of the uranyl ion in water, using potentials as Rai <i>et al</i> ^[209]	202
77	Summary of cell parameters for uranyl minerals, comparing the results from potential sets with experimentally determined values	208
78	Layered double hydroxysulfate cell parameters ^[219]	215
79	sulfate green rust DFT modelling results for monodentate sulfate orientation, using PBE_pseudo_D potentials	217
80	sulfate green rust DFT modelling results for monodentate, tridentate and tridentate (with constrained cell angles) sulfate orientation, using PBE_pseudo_D potentials. Tridentate with constrained cell angles did not optimise.	219
81	sulfate green rust DFT modelling results for tridentate sulfate orientation with water, using PBE_pseudo_D potentials	221
82	Partial charges (q_u) on ions used in the testing and interatomic potential modelling of sulfate green rust ($\text{Fe}_6(\text{OH})_6\text{SO}_4$)	222
83	Lennard-Jones potentials for sulfate green rust ($\text{Fe}_6(\text{OH})_6\text{SO}_4$), modified CLAYFF potentials	223
84	Harmonic potentials for sulfate green rust ($\text{Fe}_6(\text{OH})_6\text{SO}_4$), modified CLAYFF potentials	223
85	Three-body potentials for sulfate green rust ($\text{Fe}_6(\text{OH})_6\text{SO}_4$), modified CLAYFF potentials	224
86	sulfate green rust experimentally determined cell parameters compared to interatomic potential modelling results, for tridentate sulfate orientation	224

87	Lennard-Jones potentials for sulfate green rust ($\text{Fe}_6(\text{OH})_6\text{SO}_4$), modified CLAYFF potentials	226
88	sulfate green rust experimentally determined cell parameters com- pared to interatomic potential modelling results, for tridentate sulfate orientation with LJ 9-6 H-Os potential added	226
89	Lennard-Jones potentials for sulfate green rust ($\text{Fe}_6(\text{OH})_6\text{SO}_4$), modified CLAYFF potentials with H-H added	227
90	sulfate green rust experimentally determined cell parameters com- pared to interatomic potential modelling results, for tridentate sulfate orientation with H-H potential added	228
91	Lennard-Jones potentials for sulfate green rust ($\text{Fe}_6(\text{OH})_6\text{SO}_4$), modified CLAYFF potentials with H-H derived from 9-6 potential added	229
92	sulfate green rust experimentally determined cell parameters com- pared to interatomic potential modelling results, for tridentate sulfate orientation with H-H derived from 9-6 potential added . . .	230
93	Partial charges (q_u) on ions used in the testing and interatomic po- tential modelling of sulfate green rust with water ($\text{Fe}_6(\text{OH})_6\text{SO}_4 \cdot 0.5\text{H}_2\text{O}$)	231
94	Lennard-Jones potentials for sulfate green rust ($\text{Fe}_6(\text{OH})_6\text{SO}_4$), modified CLAYFF potentials with H-H derived from 9-6 poten- tial, with water	231
95	Harmonic potentials for sulfate green rust with water ($\text{Fe}_6(\text{OH})_6\text{SO}_4 \cdot 0.5\text{H}_2\text{O}$), modified CLAYFF potentials	233
96	Three-body potentials for sulfate green rust with water ($\text{Fe}_6(\text{OH})_6\text{SO}_4 \cdot 0.5\text{H}_2\text{O}$), modified CLAYFF potentials	233

97	sulfate green rust experimentally determined cell parameters compared to interatomic potential modelling results, for tridentate sulfate orientation with H-H derived from 9-6 potential and water added	234
98	sulfate green rust surfaces: surface areas and energies	239
99	Layered double hydroxychloride (GR1) cell parameters as reported by Refait <i>et al</i> and by Bernal <i>et al</i> using X-ray diffraction studies	242
100	Chloride ion fractional coordinates used to generate Cartesian coordinates for chloride GR1	245
101	Chloride green rust DFT modelling results using PBE_pseudo_D potentials	246
102	Partial charges (q_u) on ions used in the testing and interatomic potential modelling of chloride green rust ($\text{Fe}_4(\text{OH})_8\text{Cl}$)	247
103	Lennard-Jones potentials for chloride green rust ($\text{Fe}_4(\text{OH})_8\text{Cl}$), modified CLAYFF potentials	247
104	Harmonic potentials for chloride green rust ($\text{Fe}_4(\text{OH})_8\text{Cl}$), modified CLAYFF potentials	248
105	Oxygen atom initial fractional coordinates used to generate Cartesian coordinates for chloride GR1 with water	249
106	Oxygen atom refined fractional coordinates used to generate Cartesian coordinates for chloride GR1 with water	250
107	Chloride green rust DFT with water modelling results using PBE_pseudo_D potentials.	254
108	Partial charges (q_u) on ions used in the testing and interatomic potential modelling of chloride green rust with water ($\text{Fe}_4(\text{OH})_8\text{Cl} \cdot 2\text{H}_2\text{O}$)	255

109	Lennard-Jones potentials for chloride green rust ($\text{Fe}_4(\text{OH})_8 \text{Cl} \cdot 2 \text{H}_2\text{O}$), modified CLAYFF potentials	256
110	Harmonic potentials for chloride green rust ($\text{Fe}_4(\text{OH})_8 \text{Cl} \cdot 2 \text{H}_2\text{O}$), modified CLAYFF potentials	257
111	Three-body potentials for chloride green rust ($\text{Fe}_4(\text{OH})_8 \text{Cl} \cdot 2 \text{H}_2\text{O}$), modified CLAYFF potentials	257

List of equations

1	Periodic boundary condition	52
2	Schrödinger equation	53
3	Schrödinger equation	53
4	Schrödinger Hamiltonian Operator	54
5	Total Energy 1	55
6	Total Energy 2	55
7	Total Energy 3	56
8	Total Energy 4	56
9	Total Energy 5	56
10	Total Energy 6	57
11	Total Energy 7	58
12	Generalised gradient approximation	60
13	Kohn-Sham equation	62
14	The potential model	66
15	The potential model - intramolecular interactions	67
16	The potential model - intermolecular interactions	67
17	Born-Mayer interaction energy between ions	68
18	Overall interaction energy of a system	68
19	Gaussian distribution of screening charge cloud	72
20	Total energy of screened Coulombic interactions	72
21	Complementary error function	72
22	Poisson's equation	73
23	Poisson's equation component	73

24	Poisson's equation in Fourier form	74
25	Poisson's equation with Fourier transform of charge density	74
26	Poisson's equation, variant	74
27	Poisson's equation, variant	74
28	Electrostatic potential in real space	75
29	Contribution of ϕ_1 to the interaction energy	75
30	Interaction energy, $\rho(k)$	75
31	Self interaction energy	76
32	Total contribution to potential energy 1	76
33	Total contribution to potential energy 2	76
34	Lennard-Jones potential 1	78
35	Lennard-Jones potential 2	79
36	Lennard-Jones potential 3	80
37	Buckingham potential 1	81
38	Intramolecular forces	82
39	Harmonic oscillator	83
40	Morse potential	84
41	Three-body potential	86
42	Four-body potential	86
43	The shell model	88
44	The shell model - ion polarisability	88
45	Ionic positions at energy minimum	90
46	Method of steepest descent	91
47	Steepest descent displacement vector 1	91
48	Steepest descent displacement vector 2	91

49	Steepest descent gradient value 1	92
50	Steepest descent gradient value 2	92
51	Steepest descent gradient value 3	92
52	Newton-Raphson Taylor expansion	93
53	Newton-Raphson ion displacement	93
54	Newton-Raphson second derivative matrix	93
55	Newton-Raphson system equilibrium	94
56	Newton-Raphson δr	94
57	Newton-Raphson r_{n+1}	94
58	Newton-Raphson Hessian matrix approximation	95
59	Molecular dynamics initial conditions 1	96
60	Molecular dynamics initial conditions 2	96
61	Newton's equations of motion 1	97
62	Newton's equations of motion 2	97
63	Newton's equations of motion 3	97
64	Taylor expansion of particle positions, velocities and accelerations .	99
65	Taylor expansion of particle position 1	99
66	Taylor expansion of particle positions 2	99
67	Taylor expansion of particle positions 3	99
68	Taylor expansion of particle positions 4	100
69	Taylor expansion of velocity 1	100
70	Taylor expansion of velocity 2	100
71	Verlet leapfrog algorithm 1	101
72	Verlet leapfrog algorithm 2	102
73	Verlet leapfrog algorithm 3	102

74	Verlet leapfrog algorithm 4	102
75	Verlet leapfrog algorithm 5	102
76	Verlet leapfrog algorithm current velocities	103
77	NVE ensemble	104
78	Nosé-Hoover algorithm	105
79	Nosé-Hoover friction coefficient	105
80	Verlet leapfrog NVT modification 1	105
81	Verlet leapfrog NVT modification 2	106
82	Verlet leapfrog NVT modification 3	106
83	Verlet leapfrog NVT modification 4	106
84	Verlet leapfrog NVT modification 5	106
85	NVT conserved quantity	107
86	Melchionna modification to the Hoover algorithm	107
87	Melchionna modification friction coefficient	107
88	Melchionna modification volume change	108
89	Verlet leapfrog Melchionna modification 1	108
90	Verlet leapfrog Melchionna modification 2	108
91	Verlet leapfrog Melchionna modification 3	108
92	Verlet leapfrog Melchionna modification 4	109
93	Verlet leapfrog Melchionna modification 5	109
94	Verlet leapfrog Melchionna modification 6	109
95	Verlet leapfrog Melchionna modification 7	109
96	Verlet leapfrog NPT new volume derivation	110
97	Verlet leapfrog NPT new cell vectors derivation	110
98	NPT conserved quantity	110

99	Block surface energy	116
100	Block bulk energy	116
101	Surface energy	117
102	12-6 Lennard-Jones input format	161
103	Lorentz-Berthelot E_0	161
104	Lorentz-Berthelot R_0	161
105	Simultaneous equation 1	164
106	Simultaneous equation 2	164
107	Simultaneous equation 3	165
108	Simultaneous equation 4	165
109	Buckingham potential, (var. 1)	166
110	A_{ij} ; Gilbert	166
111	Born-Mayer repulsive potential; Gilbert	167
112	Cl-Cl Born-Mayer repulsive potential; Gilbert	167
113	A_{Cl-Cl} ; Gilbert	167
114	A_{U-Cl} ; Gilbert	168
115	System Free Energy	195

List of abbreviations

AGR	Advanced gas-cooled reactor
BFGS	Broyden-Fletcher-Goldfarb-Shanno
CASTEP	Cambridge Serial Total Energy Package
DFP	Davidon-Fletcher-Powell
DFT	Density functional theory
eV	Electron volts
FFT	Fast Fourier transform
GGA	Generalised gradient approximation
GR	Green rust
ICSD	International Crystal Structural Database
KS	Kohn-Sham
LDA	Local-density approximation
LDH	Layered double hydroxide
LJ	Lennard-Jones
MM	Molecular mechanics
MSD	Mean squared displacement
OTF	On-the-fly
PBE	Perdew-Burke-Ernzerhof
PMF	Potential of mean force
QM	Quantum mechanics
RDF	Radial distribution function
SPME	Smooth particle mesh Ewald
VAF	Velocity auto-correlation function

XC Exchange-correlation

1 Introduction

Historic use of nuclear material for weapons and power production means that there is a need for reprocessing of spent nuclear fuel and decommissioning of nuclear facilities^[1]. Decommissioning of a nuclear facility must facilitate a situation where radioactive protection measures are no longer required; any radioactive material may require transport off site, further processing and it will need a safe manner of storage^[2]. Decommissioning plans have time frames in decades with the decommissioning taking place in stages^[3], which means that radioactive material is present, and must be processed and stored, over these periods of time. Decommissioning projects in the UK include historic civil nuclear legacy sites such as first generation power reactors and research sites; at Sellafield there are a number of reprocessing plants which require decommissioning^[4].

There are several needs for, and types of, nuclear reprocessing. Nuclear reprocessing was originally undertaken in the UK to extract plutonium from spent nuclear fuel so as to provide fissile material for atomic weapons production^[5]. All the UK Magnox power reactors are closed down, with the final one shut down in 2015; defueling was completed in 2019 when the last fuel was removed from Wylfa power station^[4]. Magnox fuel has a magnesium-aluminium alloy casing around a metallic uranium bar; Magnox fuel needs to be reprocessed as it corrodes if stored underwater and no method of dry storage has been established^[4]. All future Magnox reprocessing in the UK will be undertaken at Sellafield in the Magnox Reprocessing Plant^[6]. Advanced Gas-Cooled Reactors (AGR's) followed on from Magnox reactors in

the UK; the Windscale Advanced Gas-Cooled Reactor in the UK, which was shut down in 1981, is sited within the Sellafield complex and is undergoing decommissioning. AGR's use uranium dioxide pellets in stainless steel tubes as fuel and used AGR fuel is held in ponds until it is dismantled, with the fuel pins being consolidated to reduce the storage volume. This waste from AGR's is currently reprocessed, but this reprocessing is scheduled to cease in 2018 and fuel which has not been reprocessed will be placed into wet storage for around 60 years until it can be geologically disposed of^[4]. When reprocessing of the AGR fuel ceases the remaining AGR fuel, and any produced in the future, will be stored in existing wet storage facilities rather than any new facility.

Because spent fuel is stored on decommissioning sites for such a long time the storage facilities must be monitored for leaks to the groundwater; surveys need to be made of the grounds, structures and components to determine the nature and the location of any radioactive contamination. In the USA, for example, the federal government has licenced over 100 nuclear power reactors but has not licenced a single storage site for the tens of thousands of tons of highly radioactive waste produced by these sites. Thus decommissioned sites in the USA often have storage areas of highly radioactive waste with nowhere to dispose of it^[3]. In the UK the high level waste is vitrified and stored in stainless steel canisters at Sellafield in Cumbria. They are stored for at least 50 years, to cool and allow some of the radioactivity to decay, with the intention of later being transported to a geological disposal site for permanent disposal. However, these permanent disposal sites do not yet exist and the UK government has still to develop a safe disposal route for high level waste.

It has also been noted that there is a requirement for geochemically reducing conditions to be maintained for the required timescale so that uranium is maintained as the more insoluble uranium (IV), such that oxidation to the more soluble uranium (VI) is prevented^[7].

Aqueous uranium contamination of groundwater is a widespread problem at sites where reprocessing of uranium for nuclear fuel takes place, for example it is estimated that over 13 million cubic metres of soil at Sellafield is radioactive waste^[5], being classed as very low level or low level^[8]. The surface contamination is carried downward by infiltrating surface water until it reaches the aquifer, forming a contaminant plume as shown in Figure 1.

The Sellafield nuclear reprocessing site in the UK has the largest area of contaminated land in the estate of the UK Nuclear Decommissioning Authority^[5] and uranium is present as a contaminant in Sellafield groundwater^[8]. Uranium is mobile in the aqueous phase as the uranyl ion, UO_2^{2+} , though if the oxidation state is reduced from U(VI) to U(IV) then it is insoluble; it can thus be contained and the spread through groundwater halted. There are other causes of uranium pollution, including the use of depleted uranium weapons in warfare. Depleted uranium is extensively used in military applications due to its low cost and high density; it is used in the manufacture of armour-piercing bombs, tank armour and incendiary devices^[9]. Uranium can potentially lead to long-term harm with regard to mammalian reproduction and development; it can reduce fertility and cause slow or abnormal development of the embryo due to its metabolic and chemical toxicity^[10]. Large scale pollution over the long term also produces risks to ecology. Mining and processing of uranium-containing minerals in the south east of Siberia, where

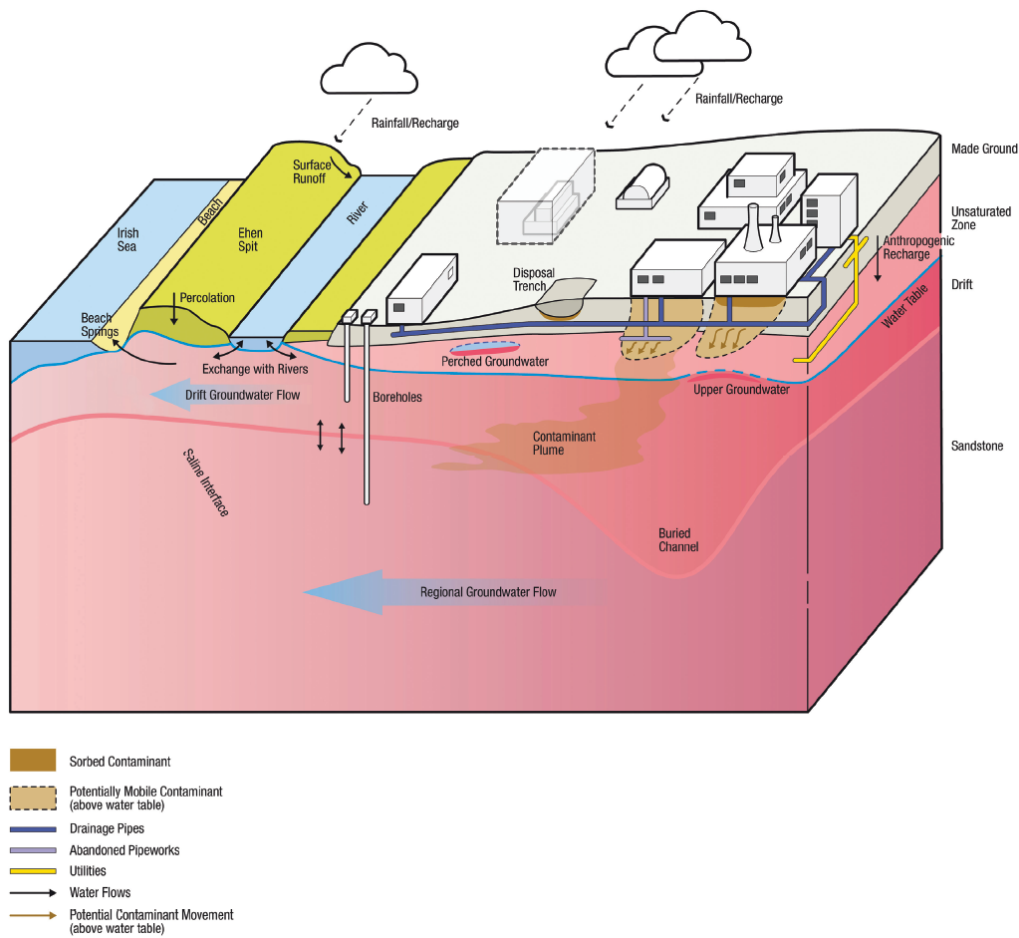


Figure 1: Contaminant movement through groundwater at the Sellafeld site^[8]

uranium has been mined for over 30 years, has resulted in the surrounding soil on the prairies having a uranium concentration which is approaching 600 times the background value. A 2003 study by Gongalsky found the concentration of uranium to be 2.6 mg kg^{-1} in a soil sample taken at 0-10 cm depth from a control site; in one of the test sites affected by mining operations the uranium concentration was $1474.0 \text{ mg kg}^{-1}$ from a soil sample taken at the same depth. This has caused a reduction of biodiversity and wildlife abun-

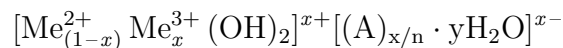
dance of between 3 and 37 times in macroinvertebrates^[11]. Naturally occurring uranium is found as uranium-238 (the most common isotope, accounting for almost 99.3% of uranium), uranium-235 (around 0.7%) and uranium-234 (a very small fraction, around 0.005%). Uranium has an extremely long half-life, meaning it will remain in the environment for a long time, and so poses a long-term health risk; the half-life of uranium-238 is around 4.47 billion years and the half-life of uranium-235 is approximately 704 million years^[12]. In a 2012 review by Li *et al*, current remediation technologies for environments polluted with uranium were separated into three categories; physical, chemical and biological^[13]. Chemical methods are experimental at present and have yet to be developed for any large scale application. An example of the method is the use of zero valent iron to remove uranium from contaminated water, as proposed by Noubactep *et al*^[14], where co-precipitation of iron corrosion products and uranium is shown to be the initial mechanism of uranium removal.

Biological methods involving bacterial and fungal micro-organisms have been used to remove uranium pollution from the environment^[15,16]. In 2002 it was demonstrated by Malekzadeh and co-workers that pseudomonas MGF-48 can absorb uranium ranging from 50 to 200 mg/l; one gram of bacterial biomass was able to take up 174mg of uranium^[17]. Phytoremediation of low concentrations of uranium has been demonstrated using sunflower and Indian mustard, where the roots uptake uranium even though it has not yet been shown to be a nutrient for the plants^[18]. Sunflowers have been used in pilot studies^[19] whilst other experiments have shown the efficacy of willow moss, celery and small duckweed^[20]. Absorption and accumulation of uranium has

also been demonstrated using cabbage, tumbleweed, mustard, sunflowers and reeds in other studies^[21,22,23], with results suggesting the aerial parts of the plants accumulate the most uranium^[24]. These categories of remediation can be combined, which has been demonstrated by Zhou *et al*, utilising zero valent iron and sulfate-reducing bacteria to remove uranium from waste water^[25].

Physical remediation methods such as precipitation, coagulation, evaporation and membrane separation can be used on a very small scale, but they are too expensive to use on large scale pollution^[26]. Synthetic hydroxyapatite ($\text{Ca}_5(\text{PO}_4)_3\text{OH}$), which is a naturally occurring mineral form of calcium apatite, has been demonstrated to adsorb 95% of uranium from waste water^[27]; neutral to acidic conditions were shown to be favourable for this adsorption. It is the potential use of naturally occurring minerals, namely green rusts, for uranium pollution remediation that is the overarching tenet of this work; if this is found to be viable then the possibility of using green rust for long-term nuclear waste storage or contaminant remediation can be further investigated.

Layered double hydroxides (LDH) include the group know as green rusts, which have a structure of stacked layers of edge-sharing metal octahedra; the metal ions are a mixture of divalent and trivalent cations and the layers are separated by anions within the interlayer spaces. LDHs have a limited composition range and the nature of the anions in the interlayer is often the main difference^[28]. They have the general formula:



where Me^{2+} could for example be Fe^{2+} , Ni^{2+} or Mg^{2+} and Me^{3+} could be

Fe^{3+} , Al^{3+} or Cr^{3+} [29].

All sites within the layer are occupied so each formula unit exhibits a nett positive formula charge of x . This charge is balanced by the negative charge from the anions in the interlayer, such as Cl^- , Br^- or CO_3^{2-} . The interlayers also contain water molecules; the typical structure is shown in Figure 2.

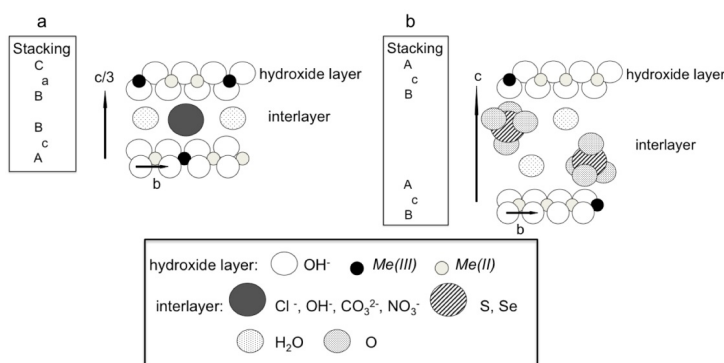
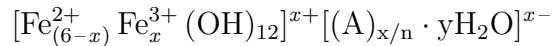


Figure 2: Structure and stacking arrangement of green rust 1 (a) and green rust 2 (b) [30]

LDH preparation in the laboratory is usually by oxidation of hydroxylated Fe(II) species or by the co-precipitation of dissolved species [31,32]. Delamination (or top-down) methods and controlled nucleation (or bottom-up) methods of LDH nanosheet preparation are described in detail in the work of Wang and O'Hare [33], with the latter method also discussed and utilised by Lv and co-workers [34]. Applications for LDHs include reduction of anionic pollutants and degradation of organic pollutants [31]. LDH synthesis and chemistry is an important area of study because of the use of LDHs in, for example, fire retardant additives [35,36], as cement additives [37], as drug delivery media [38], as ion exchange hosts [39,40,41], as polymer/LDH nanocomposites [42], as catalysts [43] and as precursors for CO₂ adsorbents [44,45,46,47,48].

Green rust (GR) compounds (iron(II)-iron(III) hydroxy-salts) are members of the family of layered double hydroxides (LDH)^[49]. Within their structure, positively charged, Fe(II)/Fe(III), hydroxide layers alternate with negatively charged inter-layers of water molecules and anions. They can be represented with the general formula:



where $x = 0.9 - 4.2$, A is an n -valent anion (typically CO_3^{2-} , Cl^- or SO_4^{2-} and y denotes the varying amounts of interlayer water (typically $y = 2$ to 4 for most GRs)^[50].

Figure 3 shows a snapshot of the equilibrium structure of hydrotalcite ($\text{Mg}_2 \text{Al}(\text{OH})_6 \text{Cl} \cdot 2 \text{H}_2\text{O}$) derived from an NPT (particle number, pressure and temperature are constant) molecular dynamics simulation at 300 K and 1 bar; this is a good example of a LDH and is isostructural with green rust. The simulation cell is composed of 18 crystallographic unit cells. The blue polyhedra represent octahedral magnesium and the pink ones indicate aluminium octahedra. The green spheres represent interlayer chloride ions with water molecules represented by bent cylinders. Oblique view slightly offset from the $[100]$ ^[51]

Two distinct forms are known to exist, namely GR1 and GR2^[52]. GR1 has a dark blue-green colour and has analogous structure to the Mg(II)-Al(III) LDHs hydrotalcite ($\text{Mg}_6 \text{Al}_2 \text{CO}_3 (\text{OH})_{16} \cdot 4 \text{H}_2\text{O}$) and pyroaurite ($\text{Mg}_6 \text{Fe}_2 (\text{OH})_{16} \text{CO}_3 \cdot 4 \text{H}_2\text{O}$). It is the favoured form of chloride and carbonate GRs. When the interlayer anions are SO_4^{2-} , the favoured structure is GR2, in which the nature of the hydroxide layers is more closely related to that of $\text{Fe}(\text{OH})_2$. GR2

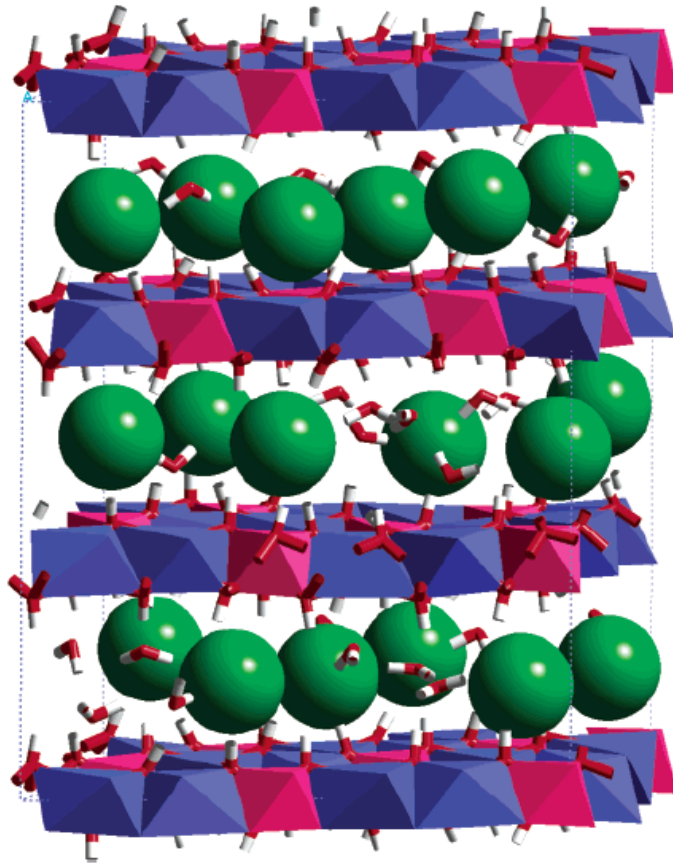


Figure 3: Image of a typical LDH^[51]

Key: octahedral magnesium, blue; octahedral aluminium, pink; chlorine, green; water molecules, bent red and white cylinders.

exhibits a slightly dulled dark green colouration.

Green rusts can be synthesised in the laboratory; Kim and co-workers used polypyrrole as a conducting polymer to facilitate crystal growth of GR via controlled electron transfer^[54]. In 2018 Usman *et al* reviewed several methods of GR synthesis, including biotic and abiotic pathways along with methods of characterisation^[55]. Fredrickson *et al* demonstrated that biogenic iron mineralisation was viable to produce GR, though poorly crystalline, us-

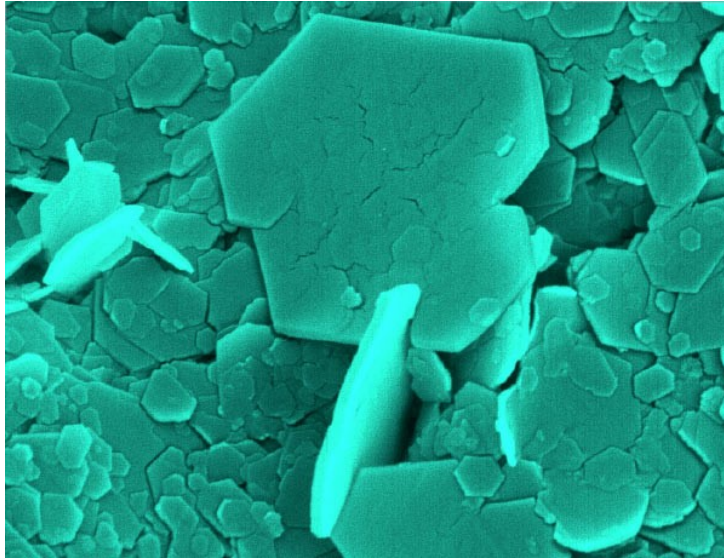


Figure 4: Microscope image of green rust^[53]

ing iron-reducing bacteria in a buffer solution of piperazinediethanesulfonic acid to reduce hydrous ferric oxide; the solid compounds were characterised using X-ray diffraction, scanning electron microscopy, transmission electron microscopy with energy-dispersive X-ray spectroscopy and selected area electron diffraction^[56]. Microbially induced corrosion of steel, resulting in the formation of GR2, has also been studied by Génin *et al*, using Mössbauer spectroscopy and X-ray diffraction to investigate the rust products^[57]. Coprecipitation by mixing solutions of iron (II) and iron(III) salts in a solution of NaOH was effective in producing iron (II-III) hydroxysulfate precipitates (GR2), as exhibited by Génin *et al*; the precipitates were characterised using Mössbauer spectroscopy, X-ray diffraction, transmission electron microscopy and atomic force microscopy^[58].

Under anaerobic conditions GR can form naturally in hydromorphic soils^[59]; however in the presence of air GRs will oxidise quickly (a time of less than

10 seconds was determined by Drissi *et al*^[60]) and precautions must be taken. The presence of Fe(II) means that GR is chemically reactive; Génin *et al* measured the electrode potential (E_h) of carbonate GR as approaching 300mV^[61]. The redox potential of GR offers interesting environmental applications; GR particles can reduce many contaminants to create insoluble and less mobile forms. This can prevent the spread of contaminants and thus reduce their bioavailability. An example is municipal waste dumps, where contaminants can be encapsulated to prevent the escape of radioactive waste into the environment^[62] Previous work with synthetic GR, incorporating SO_4^{2-} , has demonstrated an ability to reduce pollutants such as nitrites^[63] and heavy metal ions^[64,59]; as the GR is oxidised the pollutants are either immobilised or degraded. Whilst the composition and structure of GR has been established by this previous work^[52], the mechanisms by which these redox processes occur are still little understood, whether occurring on the surface or within the bulk structure. The reason is that although GR is relatively easy to synthesise, when it is exposed to air it oxidises to normal brown rust within minutes; this makes it very difficult to study via experiment without using expensive controlled atmosphere facilities or a synchrotron radiation source; a GR intermediate in the formation of magnetite (Fe_3O_4) is reported under O_2 -free conditions at pH 9, followed by corrosion of the GR as magnetite formation occurs. At pH 7 the stable phase was reported as sulfate GR. These results were identified using synchrotron-based time-resolved energy dispersive X-ray diffraction.^[65] An alternative method of investigation of such processes is to use computer modelling at an atomistic level; this allows study of the structure, stability and reactivity of the

materials under a variety of conditions, whilst removing the timescale problems associated with physical experiment. Such a modelling study forms the basis of this project.

All theoretical approaches to modelling have their drawbacks. Ab initio methods using quantum mechanical (QM) techniques, such as density functional theory (DFT)^[52], are accurate but they are slow and expensive; as such they are often limited to modelling a few hundred or so atoms and thus the scale of some processes can be difficult to model. QM calculations will however be used to gain understanding of the fundamental nature of the system and to test the atomistic model for accuracy.

Mesoscale modelling can produce useful data but may lack detail for direct atomic interactions and the chemistry therein.

A molecular mechanical (MM) model uses interatomic potentials (also known as force fields) and can model larger systems than DFT, of many thousands or millions of atoms, simulating each atom as one particle. The MM calculations are quicker to execute, though they require the derivation of a reliable and robust set of potential parameters that can model the atom-level interactions. The potentials must be able to do this for the minerals, molecules and solvent (which is water in this case) and must do so for the interactions between them all. The potential model describes the interactions in a system between two or more species using parameterised potential functions. These are simulations at the atomistic level and they allow modelling of larger systems than DFT. To make sure that variations in geometry still provide accurate interactions in the model, the parameterisation requires care. There are also methods such as dissipative particle dynamics where the

particle is more than one atom (such as an amino acid) or where the particle is less than one atom, such as in the shell model of an atom or the TIP4P water model^[66].

Using existing potential sets where possible is sensible as much work has already been done in their development; there will however be a need to develop potentials where they do not already exist. Where mixing of Lennard-Jones (LJ) potentials is required to produce new potentials the Lorentz-Berthelot mixing rules would seem an ideal starting point, though as can be seen in the methodology of Chapter 5 there are occasions when the type of potential being used necessitates a variation in method.

Whilst atomistic simulation packages have been previously used by other research groups in similar areas they have not been used for the research described in this project. Cooke, Redfern and Parker used atomistic simulation to study the segregation of ten isovalent impurities (such as Al^{3+} and La^{3+}) to the $(0\ 1\ \bar{1}\ 2)$ and the $(0\ 0\ 0\ 1)$ surfaces of haematite ($\alpha\text{-Fe}_2\text{O}_3$)^[67]; they showed that segregation was energetically favourable in virtually every case, with the $(0\ 1\ \bar{1}\ 2)$ surface showing the most favourable surface concentration of the impurity to be 33.33%. If the $(0\ 0\ 0\ 1)$ surface was terminated by iron atoms the energy minimum was also found to be at 33.33% impurity coverage, though if the $(0\ 0\ 0\ 1)$ surface was terminated by oxygen atoms the energy minimum was between 16.67 and 33.33% coverage, depending on which cation was being considered.

Chroneos *et al*, whilst examining the significance of hydroxide-containing systems to materials science, modelled a number of hydroxides and oxyhydroxides, including iron hydroxide ($\text{Fe}(\text{OH})_2$ and $\text{Fe}(\text{OH})_3$) and iron oxyhy-

droxide ($\text{FeO}(\text{OH})$), and were able to report two internally consistent transferable atomic scale models that were capable of modelling such systems^[68]. In further work, building on this study, Chronos and co-workers addressed the problem of X-ray diffraction having difficulty in identifying hydrogen atom positions due to hydrogen scattering X-rays only very weakly^[69]; they used two models to predict the hydrogen atoms positions, one based on ionic potentials and one based on DFT. They demonstrated the effectiveness of these approaches by comparison to experimental data for minerals whose hydrogen positions are already known.

Kerisit *et al* investigated interfaces of the hydroxide terminated $(1\ 0\ 0)$ surface of goethite ($\text{FeO}(\text{OH})$) with aqueous solutions of sodium chloride and were able to demonstrate that classical models of the electrical double layer are not accurate in their description of ions near the surface^[70]; they found that to adequately describe the effects of the surface on the liquid phase the solvent molecules needed to be treated explicitly. The group performed similar simulations of sodium chloride solutions in contact with the $(1\ 0\ \bar{1}\ 4)$ surface of calcite (CaCO_3) and the $(0\ 1\ \bar{1}\ 2)$ surface of haematite (Fe_2O_3) and demonstrated the same principles, suggesting the nature of the observations is not dependent on the nature of the mineral surface. This demonstrated the ability of atomistic simulations to consider and extend phenomenological models to provide more in-depth insight into the solid-liquid interface.

The interaction between the surfaces of polar solids and aqueous solutions was also investigated by Spagnoli *et al* when considering the $(1\ 0\ \bar{1}\ 4)$ surface of calcite (CaCO_3) and the $(0\ 0\ \bar{1}\ 1)$ surface of haematite (Fe_2O_3) in contact with aqueous electrolyte solutions of NaCl, of varying concentration^[71]. They

found the two surfaces showed different bonding mechanisms with the water but that both produced particular layering of the water; this modified some surface behaviours such as diffusivity and charge distribution. The charge distribution within the solvent generally provided greater control of the dissolved ion arrangement than ionic strength or surface charge. A double layer was demonstrated at neutral surfaces and the charge distribution was shown to oscillate into the bulk of the water. Atomistic simulation based on the Born model of solids was used in the study^[72], with potentials derived by reproducing the structure and energetics from *ab initio* calculations.

The hydration of surfaces of white rust ($\text{Fe}(\text{OH})_2$), goethite ($\alpha\text{-FeO}(\text{OH})$) and haematite ($\alpha\text{-Fe}_2\text{O}_3$) were investigated using surface simulations by de Leeuw *et al* using energy minimisation techniques based on the Born model of solids^[73]. A potential model, polarisable *via* the shell model of Dick and Overhauser^[74], was developed and initially tested by reproducing the bulk structures of eight iron oxides and oxyhydroxides, before being used to model the surfaces of the minerals under investigation. It was shown that the major interaction at the surfaces was between the oxygen atoms of adsorbing water molecules and surface iron ions, followed by hydrogen bonding of the water hydrogen atoms with surface oxygen ions. The atomistic models were shown to be in good agreement with experimental results for the thermodynamic morphologies of the minerals. The (0 0 1) surface of $\text{Fe}(\text{OH})_2$ was shown to be the most stable surface by a considerable margin, the (0 1 0) surface was the most stable goethite surface and the (0 0 0 1) surface of haematite was studied (along with other surfaces) having previously been shown to be one of the most stable surfaces of haematite^[75,76,77,78,79]. These results proved

the viability of the derived iron oxyhydroxide interatomic potential model in aqueous environment and its suitability for transfer to other iron oxide phases.

During the investigation of jarosite ($\text{KFe}_3(\text{SO}_4)_2(\text{OH})_6$) dissolution at pH 2 and pH 8, Smith and co-workers used batch experiments on aqueous and residual solid and computational modelling^[80]; the modelling was used to study the mechanism and specific product formation of the conversion of jarosite to goethite ($\text{FeO}(\text{OH})$); it was also utilised as a means to elucidate dissolution mechanisms at the atomic level. Atomistic simulation based on the Born model of solids was used, utilising interatomic potentials which were derived by fitting to experimental data such as structure, elastic constants and vibrational spectra. Energy minimisation of the lattice was then used to determine the equilibrium position of the ions in the structure, and the potentials refined to better reproduce experimental data.

Wander *et al* explored structure and charge hopping dynamics in green rust, using periodic slab models and cluster representations^[81]; $\text{Fe}(\text{OH})_2$ was used as a structural analogue for reduced green rust. They were able to provide a first-principles assessment of the valence interchange reaction rate for Fe^{2+} - Fe^{3+} . The modelling used Hartree-Fock calculations to provide *ab initio* optimisations of the periodic slab structure. Small clusters were then used for calculation of reorganisation energies, due to the high computational overhead of *ab initio* methods. The results suggested that solid state charge transport in green rust is facile, meaning that charge redistribution could have a major influence in directing electron transfer from green rust and into adsorbed redox-active species.

There are key questions which are as yet unanswered when considering computational modelling in the investigation of green rust as a tool for remediation of nuclear pollution and storage of nuclear waste, such as; can reliable potential sets be derived to model the bulk structure of green rust 1 and green rust 2, can atomistic modelling be used to determine the stability (thus most likely to form) of different Miller surfaces of green rust, can interatomic potentials be used to model the counter-ions and associated uranyl compounds present in the interlayers of green rust (there has been limited modelling of the uranyl ion; this is discussed in Chapter 5), can existing potential sets be used to allow simplified modelling of larger systems without complex fitting procedures, could interchangeable potential models be derived which would allow the investigation of the adsorption and absorption of actinyl ions onto and into the interlayers of green rust? The work presented in this thesis addresses these questions; however, before describing the work it is necessary to consider the theoretical methods and computational techniques utilised in the research.

2 Theoretical Methods and Computational Techniques

When performing computer modelling, the chosen method must adequately describe the system being modelled at the appropriate level of theory. This project uses both quantum mechanical (QM) and molecular modelling (MM) methods; this allows consideration of systems ranging from tens of atoms to thousands of atoms. The length scales involved range from the Angstrom level (0.1nm) to around 100nm in periodicity.

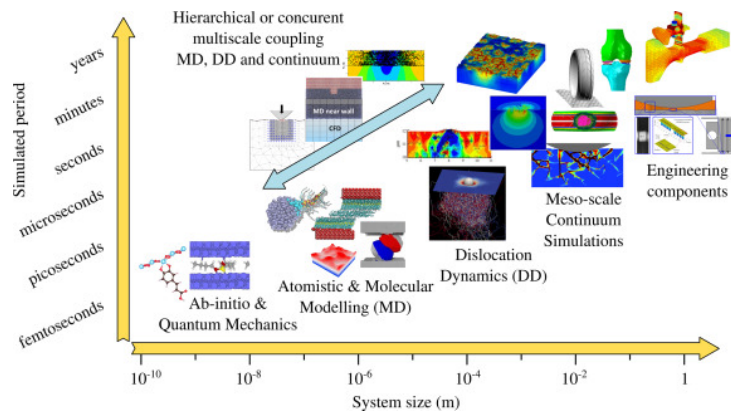


Figure 5: Chart of length-scale vs. simulation techniques^[82]

Exact solutions for solving the Schrödinger equation exist only for single electron systems, the equation cannot be solved for multi-electron systems. This means that a numerical approach is necessary; this can be a quantum mechanical approach such as DFT or a classical approach using interatomic potentials.

Whilst atomic simulation methods are used for the main parts of this project, quantum calculations are used as an aid to verifying the results.

2.1 Periodic Boundary Conditions

Periodic boundary conditions are used in all simulations in this project. This method assumes that the simulation cell is surrounded on all sides by an infinite number of identical cells. The system is periodic and when any particle leaves the simulation cell, it simultaneously enters the same cell at the opposite side.

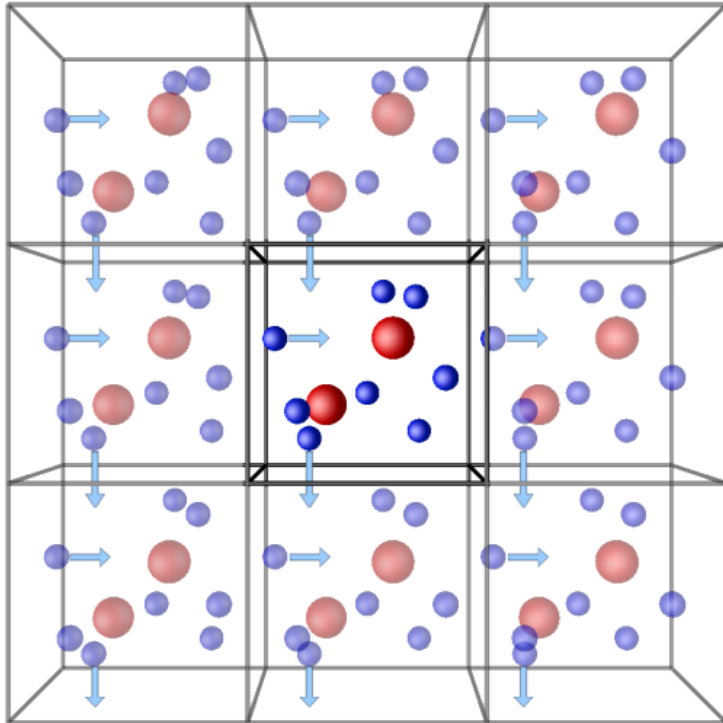


Figure 6: Illustration of the periodic boundary condition principle^[83]

The maximum inter-atomic distance r_{cut} which is taken into account in the calculations is therefore equal to half of the edge of the simulation box (this applies to MD simulations, where the atoms move):

$$r_{cut} = \frac{L}{2} \quad (1)$$

The surface or finite model size effects would therefore be small, if any. In general, the larger the simulation box and the number of molecules/atoms in it, the smaller the surface or size effects will be. This method is excellent for crystalline solids and can be used for liquids if the simulation cell is large enough. Because of the infinite periodicity there is no surface to the system; this enables the simulation of bulk crystals. If a liquid is being modelled, it prevents the presence of outer molecules that could boil off and leave the simulation. Where the simulation requires a surface to be present there are two methods to achieve this. The first is to have periodicity only in two directions, which means that the simulation would have no periodicity perpendicular to the surface (this method can be utilised in the METADISE code^[84]). The second, known as the slab method, is to still use three-dimensional periodicity but make the simulation cell very large; this results in the interactions between the cell and its periodic images being very small. In both surface and bulk calculations, this project will use energy minimisation techniques.

2.2 Electronic Structure Calculations

Electronic structure calculations endeavour to solve the Schrödinger equation for all the electrons in the system. However, an exact solution can only be obtained for one electron and so computer simulation is used for larger systems.

Solving the Schrödinger equation, (equation 2), is impossible for an N -body system.

$$H\Psi = i\hbar\frac{\partial\Psi}{\partial t} \quad (2)$$

where i is an imaginary number, \hbar is the Planck constant, Ψ is the state vector of the system, t is time and H is the Hamiltonian.

The Born-Oppenheimer approximation is most often used to simplify solving the equation; the electronic and nuclear degrees of freedom are separated from each other and the ground state of the electrons determines the energy of a given system^[85]. This approximation is based on the fact that the same forces act on the nuclei and electrons, but because they are so different in mass to each other, the electrons' response to the motion of the nuclei is immediate. The equation to be solved is therefore:

$$H\Psi = E\Psi \quad (3)$$

where Ψ is the many-body wave function for the N electronic eigenstates and E is the total energy. The Hamiltonian operator, H , is defined as:

$$H = \sum_i -\frac{\hbar^2}{2m_e} \nabla^2 r_i + V_{EXT}(\{R_I\}) + V_{e-e}(\{r_i\}) \quad (4)$$

where the first term represents the kinetic energy of the electrons, V_{EXT} is the external potential imposed by the nuclear configuration R_I and V_{e-e} denotes the Coulombic electron-electron interaction.

2.2.1 Density Functional Theory

The computer code CASTEP (Cambridge Serial Total Energy Package)^[86] was used to perform DFT calculations in this work. CASTEP is a materials modelling code based on a first-principles quantum mechanical description of electrons and nuclei. It uses the robust methods of a plane-wave basis set and pseudopotentials^[52]. DFT investigates the ground state electronic structure of many-body systems. It is particularly useful for condensed phases, as studied in this project, though difficulties are encountered if using it to model dispersion systems or intermolecular interactions such as van der Waals forces as these are not included in the standard DFT model^[87]. DFT uses functionals (functions of another function) to determine system properties.

In DFT the functional is the electron density, which is a function of space and time. The electron density is used in DFT as the fundamental property, whereas Hartree-Fock theory^[88] deals directly with the many-body wavefunction. Using the electron density significantly speeds up the calculation; the

many-body electronic wavefunction is a function of $3N$ variables (the coordinates of all N atoms in the system) but the electron density is only a function of 3 spatial coordinates, x , y and z . The Hohenberg-Kohn^[89] theorem states that all ground-state properties of the system can be determined from the density of any system; here the total ground state energy of a many-electron system is a functional of the density; if the electron density functional is known, the total energy of the system can be determined. The total energy is therefore expressed as a functional of the total electron density, dependent upon the atomic positions:

$$E = E[\rho(r), R_\alpha] \tag{5}$$

where R_α is the position of all atoms α in the system. The total energy is written as:

$$E[\rho] = T_0[\rho] + U[\rho] + E_{xc}[\rho] \tag{6}$$

$T_0[\rho]$ is the kinetic energy of non-interacting electrons; these are defined as having an analogous one-particle wave function which produces the same density as the interacting many-electron system.

$$T_0[\rho] = \sum_i n_i - \int \Psi_i^*(r) \left[-\frac{\hbar^2}{2m} \nabla^2 \right] \Psi_i(r) dr \quad (7)$$

and

$$\rho(r) = \sum_i n_i |\Psi(r)|^2 \quad (8)$$

The second term in equation 6 is the Coulombic energy; it is the total electrostatic energy from the Coulombic attraction between electrons and nuclei, the repulsion between nuclei and the repulsion between electrons; it is the sum of all the Coulombic forces in the system.

$$U[\rho] = U_{en} + U_{ee} + U_{nn} \quad (9)$$

or

$$U[\rho] = \sum_{\alpha} Z_{\alpha} \int \frac{\rho(r)}{|r - R_{\alpha}|} dr + \int \int \frac{\rho(r)\rho(r')}{|r - r'|} dr dr' + \sum_{\alpha\alpha'} \frac{Z_{\alpha}Z_{\alpha'}}{|R_{\alpha} - R_{\alpha'}|} \quad (10)$$

where Z_α is the atomic number of atom α at position R_α . The summations extend over all the atoms in the system and the integrations extend over all space.

The final term of equation 6 is the exchange-correlation energy (XC); this consists of all the remaining electronic contributions to the energy of the system. XC energy is usually less than 10% of the total energy of the system. XC energy represents the activities of electrons among each other in a multi-electron system. Because the Schrödinger equation can only be solved exactly for a single electron system the XC energy in DFT is an approximation of the energies; the quality of the DFT results depends upon the quality of the approximation. The exchange interactions change the expectation value of the distance between identical particles, such as electrons of parallel spin. The correlation energy is a measure of how much the movement of one electron is influenced by all the other electrons in the system.

Local-density approximations (LDA)^[90] are one method used as approximations to the XC energy in DFT; they depend only on the electronic density at each point in space. The assumption is made that electrons see the overall electronic landscape in the same way as they see it locally. The complex larger system can then be broken down into many pieces of uniform electron densities, each with different values. Thus the XC energy can be calculated for each electron using the assumed constant electron density in the area surrounding it. The local density elements can then be summed to provide the

total XC energy for the system. This is represented in Figure 7; the actual electron density distribution on the left is represented by the four areas of uniform electron density on the right.

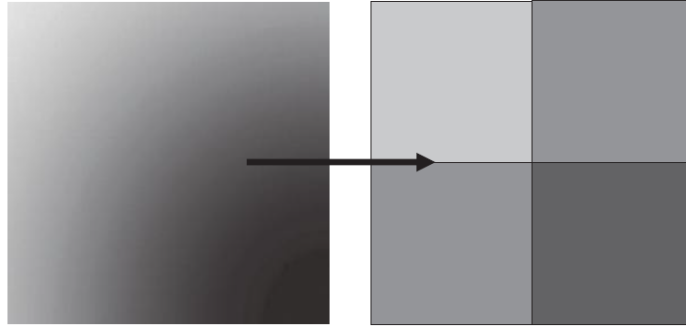


Figure 7: Schematic of LDA in two dimensions^[91]

The XC energy thus depends only on the local electron density around each volume element dr .

$$E_{xc}[\rho] = \int \rho(r)\epsilon_{xc}[\rho(r)]dr \quad (11)$$

where ϵ_{xc} is the XC energy density for a homogeneous electron gas of density $\rho(r)$.

The homogeneous electron gas is a model within which electrons are evenly distributed, with a uniformly distributed positive potential preserving the overall charge neutrality. This is a highly simplified system but it does allow convenient identification of energy terms with reasonably accurate determination. Considering that the homogeneous electron gas model is far

from the reality of actual systems, the LDA is most accurate when describing covalent systems and simple metals, where the charge density only varies relatively slowly. LDA typically underestimates E_c and overestimates E_x and the cancellation effect of these errors is partly responsible for the overall result often proving satisfactory, even though the individual exchange and correlation values do not. Significant errors and problems begin to occur when the system deviates from the LDA model; typical problems presented by LDA functionals include:

- The lattice parameters are underestimated resulting in over-binding; this results in overestimation of the cohesive energy and bulk modulus of solids.
- Spin and orbital moments are underestimated.
- Band gaps are underestimated or even absent.
- Adsorption energy values are calculated too high.
- It does not work well for materials with van der Waals attractions or weak hydrogen bonds.
- It cannot describe transition metals or their oxides which have narrow d and f bands with strongly localised electrons; for example it predicts non-magnetic ground states for some ferromagnetic and antiferromagnetic materials.

Because real systems are not homogeneous and they have varying electronic density around electrons, there is a need for more accurate XC functionals. The generalised gradient approximation (GGA)^[92,93] is able to utilise

local information and semi-local information *i.e.* at a given point it can approximate both the electron density and its gradient. Figure 8 shows a schematic representation of how LDA and GGA function. Thus the GGA method should, in principle, produce better results with the use of an additional variable for density gradient:

$$E_{xc}^{GGA}[\rho(r)] = \int \rho(r) \epsilon_{xc}^{GGA}[\rho(r), \nabla\rho(r)] dr \quad (12)$$

where $\nabla\rho(r)$ is the gradient of the electron density.

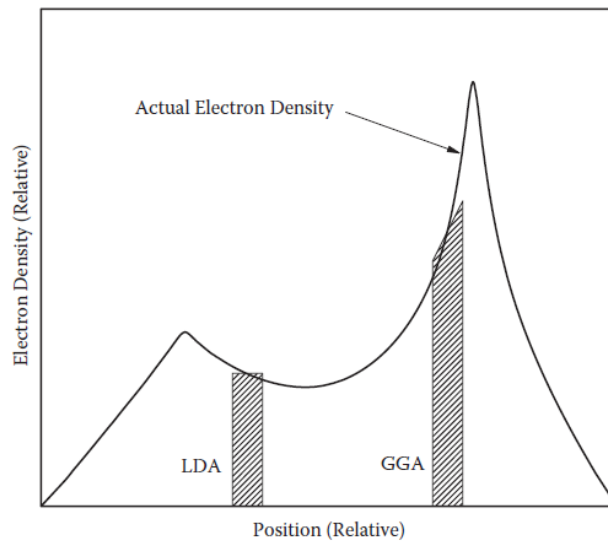


Figure 8: Schematic of local and semi-local density approximation by LDA and GGA^[91]

The general form of GGA in practice is therefore based on the LDA but with an additional factor which modifies the LDA energy. This enhancement

factor is fitted to different physical constraints and there are many different expressions of GGA, such as PW91^[93] and PBE^[92]; these functionals are incorporated into available pseudopotential files. PW91 has been very widely used because of its broad applicability and reasonable accuracy. It uses data from the uniform electron gas to provide the physics and constraints of the XC hole, but it can produce inaccuracies in the XC potential at high and low electron densities. PBE is based on PW91 but is improved and has no empirical composition. It includes local electron density and the gradient and has been shown to be accurate and computationally efficient. It does not suffer the same inaccuracies as PW91 at high and low electron densities. However, PBE almost always overestimates the lattice constants of solids (the LDA consistently underestimates the volume); typical errors are in the region of 1-2%^[94]. Alternative functionals have been developed for use with solids such as PBEsol^[95] and WC^[96]; both of these were shown to yield lattice constants in excellent agreement with experimental results by Haas *et al*, though they concluded that neither could be considered as good as PBE for all the investigated solids^[97]. By contrast, He and co-workers found that PBEsol and WC functionals reproduced most closely the structural properties of a wide variety of materials including a semiconductor (silicon), a metal (copper), and various insulators^[94]. Weck *et al* compared the measured elastic constants of zirconium tungstate (α -ZrW₂O₈) and found that PBE reproduced these to around 6% accuracy and PBEsol to around 2%^[98]. GGA does exhibit the underestimation of band gaps, similarly to LDA. PBE_pseudo_D pseudopotentials incorporate functionals that include damped atom-pairwise Grimme dispersion corrections, to mitigate for the

lack of dispersion modelling in DFT^[99]. Further development of accounting for van der Waals interactions by empirical method, termed DFT-D, is discussed by Grimme *et al*^[100], and a broader discussion of dispersion-corrected methods is undertaken by Grimme *et al* to assess the properties, advantages and disadvantages of these methods^[101]; a more detailed discussion here is beyond the scope of this work.

2.2.2 Kohn-Sham Equations

Minimising the energy of a system can be achieved by determining a self-consistent solution to a set of one-electron Kohn-Sham (KS) equations, where the orbitals are subject to constraints of the fixed number of electrons. To achieve self-consistency the KS orbitals calculate the electron densities, the electron densities calculate the KS Hamiltonian and the KS Hamiltonian will calculate the new electron densities and KS orbitals - the solution will be the KS orbitals that were started with, when self-consistency is achieved. The Hamiltonian operator corresponds to the sum of the kinetic energies plus the potential energies for all the particles in the system. The Kohn-Sham equations map the one-electron non-interacting system onto an n-electron interacting system. It is necessary to determine the set of wave functions Ψ_i which minimise the total energy functional, given by the solutions to equation 13.

$$H\Psi_i(r) = \epsilon_i\Psi_i(r) \tag{13}$$

where Ψ_i is the wave function of electronic state i and ϵ_i is the Kohn-Sham eigenvalue.

2.2.3 K-point Sampling

The periodic boundary conditions means that the system is considered as infinite, so the number of electrons is also infinite and a wave function must be calculated for each one. This cannot be achieved; Bloch's theorem allows a plane wave to be multiplied by a periodic function and so overcomes this problem^[102]. This allows calculation of a finite number of electronic wave functions, though at an infinite number of k-points. K-points are points in k-space (the reciprocal lattice of the crystal). A finite number of electronic states are occupied at each k-point. The infinite number of k-points would require an infinite number of calculations to determine the electronic potential, but the electronic wave functions of k-points that are close together will be practically identical. Thus, a region of k-space can be represented by a wave function at a single k-point. It follows that a finite number of k-points can then be used to calculate the electronic potential and so deduce the total energy of the system^[103]. The density of k-points is proportional to the volume of the system. As the density of k-points increases, the energy values calculated for the system will begin to converge. For reasons of computational efficiency, the minimum number of k-points to achieve convergence is desired. Convergence tests were used in this work for the systems of interest.

2.2.4 Plane Wave Basis Sets and Pseudopotentials

The use of plane waves and pseudopotentials is reviewed by Segall, Lindan *et al* in their discussion of first-principles simulations and the CASTEP code^[104]. Bloch's theorem states that, at each k-point, the electronic wave function can be expanded in terms of a discrete plane-wave basis set. However, these plane wave basis sets would need to be infinite at each k-point to expand the electronic wave functions. This can be overcome by using a cut-off energy so that only the plane waves with energies less than a particular value are considered; this thereby creates a finite basis set. Similarly to k-point sampling, the cut-off energy value is increased until the minimum required for energy convergence is achieved. Expanding electronic wave functions using plane waves is problematic due to the very large numbers of plane waves required; these are to account for rapid fluctuation of valence electron wave functions and the expansion of core orbitals that are very firmly bound. Pseudopotentials allow the use of far fewer plane wave basis states. Pseudopotentials use approximations which utilise the fact that physical properties of solids are much more dependent on valence electrons than those bound in the core. The core electrons and ionic potential are removed from the calculation and replaced with weaker pseudopotentials; these behave according to pseudo wave functions, not true valence wave functions. This is demonstrated in Figure 9.

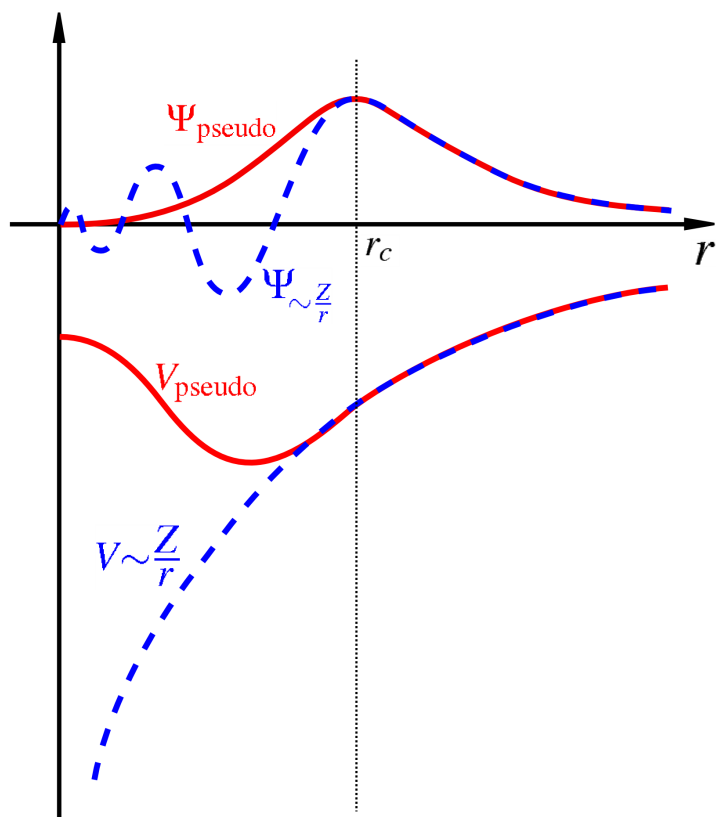


Figure 9: Comparison of a wavefunction in the Coulomb potential of the nucleus (blue) to the one in the pseudopotential (red). The real and the pseudo wavefunction and potentials match above a certain cut-off radius, r_c .

2.3 The Potential Model - Theory and Derivation

For a simulation to produce reliable results there must be a good description of all interactions between all species in the system. This means that methods such as DFT, which use a high level of theory, may seem the ideal type of approach to use in this project. In fact DFT has been used in this project using the computer simulation package CASTEP, but the computational overhead of DFT means that it can be a very expensive approach; thus the system size and number of simulations studied using this technique

are limited. There is a need for MD when water is the solvent as it is likely to be mobile. QM/MD methods could be used but these would be so slow that nanosecond timescales could not be studied. Also the dispersive interactions are likely to be significant; these interactions are present in MM simulations but not in QM simulations. Where simulations need to be on a large scale and involve phenomena such as temperature dynamical methods, these limitations mean an alternative approach must be used.

The potential model is molecular mechanical and provides just such an alternative; to describe the interactions in a system between two or more species it uses parameterised potential functions. These are simulations at the atomistic level where the atoms are only considered as charged particles, removing any explicit effect of the electrons, and they allow modelling of larger systems than DFT. To make sure that variations in geometry still provide accurate interactions in the model the parameterisation requires care.

The potential model must describe the total energy of the system by summing all the intramolecular and intermolecular interaction energies, as shown in equation 14.

$$U_{system} = U_{inter} + U_{intra} \quad (14)$$

The intramolecular interactions are themselves the sum of the energies required in bond stretching, bending and torsion between adjacent atoms:

$$U_{intra} = U_{bonds} + U_{angles} + U_{torsions} \quad (15)$$

Each of these intramolecular forces is defined by a set of parameterised equations.

The intermolecular interactions are comprised of long-range Coulombic and short-range van der Waals interactions:

$$U_{inter} = U_{Coulombic} + U_{vdw} \quad (16)$$

This model is of the type utilised in the Born Model of Ionic Solids^[72].

2.4 The Born Model of Ionic Solids

Where atomistic simulation techniques are used in this project, they are based on the Born model of ionic solids. The Born model represents the atoms of a system as point-charge particles; they interact via short-range interactions and long-range electrostatic forces as described in the potential model. The interaction energy between two ions is defined as:

$$U_{ij} = \frac{1}{4\pi\epsilon_0} \frac{q_i q_j}{r_{ij}} + \Phi(r_{ij}) \quad (17)$$

The first term represents the long-range Coulombic interactions; ϵ_0 is the permittivity of a vacuum, q_i and q_j are the ionic charges and r_{ij} is the interatomic distance between the ions. The second term, $\Phi(r_{ij})$, represents the short-range interactions between the ions; these include repulsive forces between the charged electron clouds and attractive forces caused by van der Waals interactions.

For a system, all the pairwise interactions between all ions i and j must be summed. Many-body terms are utilised where appropriate, for example to account for deviation from equilibrium bond angles. The atomic positions can be used to express the overall interaction energy of the system:

$$U_{SYSTEM} = \frac{1}{2} \sum_i^N \sum_{\substack{j \\ j \neq i}}^N \frac{1}{4\pi\epsilon_0} \frac{q_i q_j}{r_{ij}} + \frac{1}{2} \sum_i^N \sum_{\substack{j \\ j \neq i}}^N \Phi_{ij}(r_{ij}) + \frac{1}{6} \sum_i^N \sum_{\substack{j \\ j \neq i}}^N \sum_{\substack{k \\ k \neq i \\ k \neq j}}^N \Phi_{ijk}(r_{ijk}) \quad (18)$$

Summing all the pairwise electrostatic interactions cannot be used to determine the first term in equation 18 (the Coulombic energy of the system); the contribution to the electrostatic potential of the point charges decays as $\frac{1}{r}$ which results in the Coulombic term being poorly convergent at best (it can

be shown to be conditionally convergent). Summation methods such as the Ewald sum are therefore utilised to calculate the electrostatic interactions. The second and third terms of equation 18 are short-range interactions; these converge much quicker than the electrostatic interactions and can normally be calculated using simple summation.

The ionic charges q_i and q_j are usually assigned as partial charges rather than the full charge values associated with the ion (such as the formal charge of -1 for a chloride ion, for example). For fully ionic systems, formal charges have been used successfully for binary systems^[105,106] but generally require the use of strong, repulsive Born-Mayer potentials and are often paired with a Shell model. For more complex materials, especially those containing an element of covalency, the large charges associated with formal charges can prove unrealistic and partial charge models are more commonly used. Key to their success is determining what charges should be used. Quantum mechanics shows that electron density is smeared out and the associated charges are shared among nearby atoms, so there is no exact way to assign electrons to atoms; this means that the partial charge method is a useful approximation rather than an accurate representation. Because partial atomic charge is not a quantum mechanical observable there is no single way to measure partial atomic charge or to assign electron density to each atom of a molecule or solid; thus various charge models give significantly different partial atomic charges^[107,108,109]. Wang *et al* investigate such variation in their study of a number of different charge models^[110]. There are methods of assigning partial charges such as the restrained electrostatic potential approach (RESP) and RESP2^[111], which use a quantum mechanical method to approximate

charges, albeit with a tuneable parameter in RESP2. However it remains the case that there is no unified system to achieve consistent values for partial charges across different force field models. This means that transferability between models can be problematic, though where there are identical atoms with different charges between models there is the possibility of scaling partial charges from one or both models and testing the results; these scaled charges can then be refined and retested. Partial charge scaling has been tested and validated as a method in studies such as that of Chaudhari *et al*^[112]. This work utilises existing partial charge models where available, such as those in the CLAYFF potential model^[51], and also uses charge scaling to adjust partial charges from different models.

2.5 Coulombic Summation

As stated in section 2.4, Coulombic summation converges poorly due to the $\frac{1}{r}$ term and a quicker, but still reliable, summation method is required; the Ewald sum is the method employed in this project.

2.5.1 Ewald Summation

Ewald summation was developed by Paul Peter Ewald to calculate long-range interactions in periodic systems, in the field of theoretical physics^[113]. The method was first employed in molecular dynamics during the 1950's^[114,115]; since the 1970's its use has become widespread in computer simulations of systems where the particles interact via inverse square force laws such as gravity or, in the case of this project, electrostatics^[116,117]. The long-range

interaction energies are divided into two parts; the near-interactions can be calculated quickly in real space as their sum quickly converges. At larger distances the interactions are calculated by summing their Fourier transforms in reciprocal space; this allows rapid convergence of the energies, which does not happen when using direct summation. The method tacitly assumes the system is infinitely periodic, to allow the use of the Fourier sum.

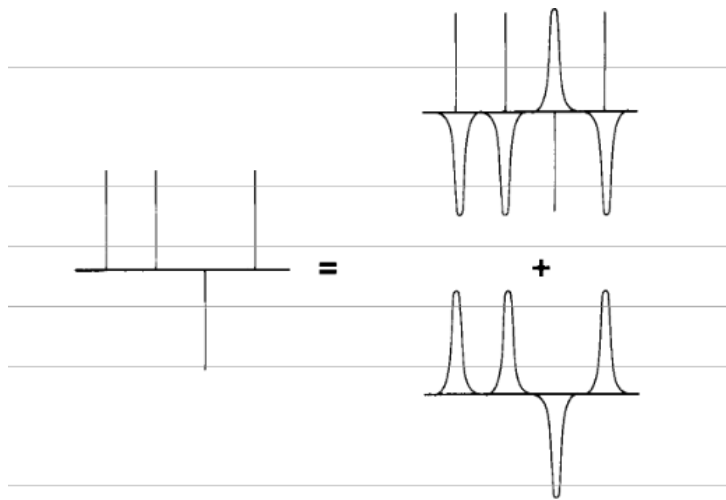


Figure 10: Fourier transformation summation^[118]

Figure 10 demonstrates how a set of point charges may be considered as a set of screened charges, minus the smoothly varying screening background.

The poor convergence of equation 17 is because the contribution of the electrostatic potential due to the point charge decays as $\frac{1}{r}$. The Ewald method assumes that every particle i , with a charge of q_i , is surrounded by a diffuse cloud of charge of the opposite sign, which exactly cancels the charge q_i . This means that the electrostatic charge due to particle i is completely due to the unscreened fraction of q_i . This fraction quickly tends to 0 at long distances; the rate at which this occurs is due to the functional form

of the screening charge distribution. Gaussian distributions of the form in equation 19 are used to represent the cloud of screening charge.

$$\rho_i(r) = -q_i \left(\frac{\alpha}{\pi}\right)^{3/2} \exp(-\alpha r^2) \quad (19)$$

α , the arbitrary parameter, determines the width of the distribution and r is the position relative to the centre of the distribution.

The total contribution of the screened Coulombic interactions to the interaction energy, U_{REAL} , can be written as:

$$U_{REAL} = \frac{1}{2} \left(\frac{1}{4\pi\epsilon_0}\right) \sum_n \sum_{i=1}^N \sum_{j=1}^N \frac{q_i q_j}{|r_{ij} + nL|} \operatorname{erfc}(\sqrt{\alpha}|r_{ij} + nL|) \quad (20)$$

where $\operatorname{erfc}(x)$ is the complementary error function, shown as:

$$\operatorname{erfc}(x) = 1 - \frac{2}{\sqrt{\pi}} \int_0^x \exp(-t^2) dt \quad (21)$$

As x increases, this tends to zero. Thus $n = 0$ is the only term which contributes to the sum in real space, if α is large enough.

The electrostatic potential due to a screened charge is a rapidly decaying function of r , meaning that the electrostatic potential due to a set of screened charges at point r_i can be computed by direct summation. But the potential due to point charges is the quantity of interest, not the potential due to screened charges. Thus the added screening charge must be removed from every particle in the system, as represented visually in Figure 10. The compensating charge distribution varies smoothly in space; it has the same sign as the original charge q_i and the same shape as the distribution $\rho_i(r)$. The Fourier transforms of these charge distributions can be summed in reciprocal space and their contribution to the electrostatic potential calculated.

The electrostatic potential at a point r_i , due to a charge distribution $\rho_i(r)$, consisting of a periodic sum of Gaussians can be represented by Poisson's equation:

$$-\nabla^2\phi_1(r) = \frac{1}{\varepsilon_0}\rho_1(r) \quad (22)$$

where

$$\rho_1(r) = \sum_n \sum_{j=1}^N q_j \left(\frac{\alpha}{\pi}\right)^{3/2} \exp[-\alpha|\mathbf{r} - (\mathbf{r}_j + n\mathbf{L})|^2] \quad (23)$$

Poisson's equation in Fourier form becomes:

$$k^2\phi_1(k) = \frac{1}{\varepsilon_0}\rho_1(k) \quad (24)$$

A Fourier transformation of ρ_1 , the charge density, gives:

$$\rho_1(k) = \frac{1}{V} \int_V \rho_1(r) \exp(-ik \cdot r) dr \quad (25)$$

If $\rho_1(r)$ in equation 25 is replaced by its form in equation 23, equation 25 becomes:^[118]

$$\rho_1(k) = \frac{1}{V} \sum_{j=1}^N q_j \exp(-ik \cdot r_j) \exp(-k^2/4\alpha) \quad (26)$$

Combining equations 24 and 26 gives:

$$\phi_1(k) = \frac{1}{k^2\varepsilon_0} \frac{1}{V} \sum_{j=1}^N q_j \exp(-ik \cdot r_j) \exp(-k^2/4\alpha) \quad (27)$$

The electrostatic potential in real space is given by:

$$\begin{aligned}
\phi_1(r) &= \sum_{k \neq 0} \phi_1(k) \exp(ik \cdot r) \\
&= \frac{1}{V} \sum_{k \neq 0} \sum_{j=1}^N \frac{q_j}{k^2 \epsilon_0} \exp[ik \cdot (r - r_j)] \exp(-k^2/4\alpha)
\end{aligned} \tag{28}$$

Therefore the contribution of ϕ_1 to the interaction energy is:

$$\begin{aligned}
U_{RECIP} &= \frac{1}{2} \sum_i q_i \phi_1(r_i) \\
&= \frac{1}{2} \sum_{k \neq 0} \sum_{i=1}^N \sum_{j=1}^N \frac{q_i q_j}{V k^2 \epsilon_0} \exp[ik \cdot (r_i - r_j)] \exp(-k^2/4\alpha) \\
&= \frac{V}{2} \sum_{k \neq 0} \frac{1}{k^2 \epsilon_0} |\rho(k)|^2 \exp(-k^2/4\alpha)
\end{aligned} \tag{29}$$

where

$$\rho(k) = \frac{1}{V} \sum_{i=1}^N q_i \exp(ik \cdot r_i) \tag{30}$$

But equation 29 includes the interaction of q_i with its own Gaussian charge cloud; this self-interaction requires correction. The contribution to the overall interaction energy of this charge distribution is given by:

$$U_{SELF} = \frac{1}{4\pi\epsilon_0} \sqrt{\frac{\alpha}{\pi}} \sum_{i=1}^N q_i^2 \quad (31)$$

The U_{SELF} term remains constant throughout the simulation as it is independent of the particle's position in space. The total contribution to the potential energy is therefore:

$$U_{COUL} = U_{REAL} + U_{RECIP} - U_{SELF} \quad (32)$$

which can be written:

$$U_{COUL} = \frac{1}{2} \left(\frac{1}{4\pi\epsilon_0} \right) \sum_n' \sum_{i=1}^N \sum_{j=1}^N \frac{q_i q_j}{|r_{ij} + nL|} \operatorname{erfc}(\sqrt{\alpha}|r_{ij} + nL|) + \frac{V}{2} \sum_{k \neq 0} \frac{1}{k^2 \epsilon_0} |\rho(k)|^2 \exp(-k^2/4\alpha) - \frac{1}{4\pi\epsilon_0} \sqrt{\frac{\alpha}{\pi}} \sum_{i=1}^N q_i^2 \quad (33)$$

α can be chosen to optimise the simulation speed as it is present in the sums of both real space and reciprocal space.

Thus, the Ewald method allows high accuracy and reasonable time-scale when computing long-range interactions. The molecular system must be charge neutral for this method (although GULP and DL_POLY do allow charged cells, the method is less accurate).

2.5.2 Smooth Particle Mesh Ewald Summation

A modification of the Ewald summation technique is the Smooth particle mesh Ewald method; the resultant technique is commonly quicker than the Ewald method. The Gaussian charge distribution is approximated using a gridded distribution and a 3D fast Fourier transform (FFT) is applied to the grid. Where the Ewald sum scales as $N^{\frac{3}{2}}$, the SPME method usually scales as $N\log(N)$.

2.6 Parry Summation

Parry summation^[119,120] is a variation of the Ewald sum but is measured in two dimensions rather than three. This makes it useful for simulations of crystal surfaces which are periodic in two dimensions. The method takes crystal surfaces to be a series of charged planes of infinite size, rather than as an infinite lattice. When the electrostatic interactions are summed the vectors are separated into those which are in the plane and those which are perpendicular to it; this means that the sum of plane charges cannot be

presumed to be zero and the reciprocal space term requires evaluation. A detailed derivation of the reciprocal space term is given by Heyes *et al*^[121].

2.7 Short-range Potentials

A number of different interactions contribute to the short-range potentials. At short interatomic distances, the electron clouds of each atom will strongly interact and repel each other. At these same distances, the fluctuating dipoles on each ion will cause dipole-dipole interactions and so result in Van der Waals attractive forces. This project utilises parameterised potential functions to describe the short-range repulsive and attractive interactions. The parameters for these potentials can be derived in one of two ways; they can be fitted to more accurate simulations such as DFT or they can be derived empirically from experimental data such as crystallographic positions. The Lennard-Jones potential, also known as the L-J potential or 12-6 (or 9-6, 12-10 *etc.*) potential, is a mathematical model approximating the interaction between a pair of neutral molecules or atoms.^[122]

Figure 11 is a graph of energy vs. distance for the 12-6 Lennard-Jones potential; r_m is the distance at which the potential reaches its minimum.

There are several ways of expressing the Lennard Jones potential, one of which is shown in equation 34

$$V(r) = \frac{A}{r^n} - \frac{B}{r^m} \quad (34)$$

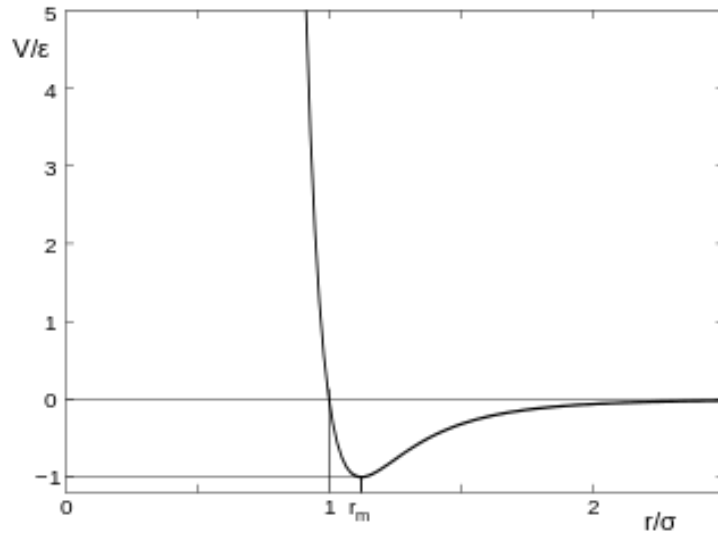


Figure 11: The Lennard-Jones potential^[122]

$$A = 4\epsilon\sigma^n$$

$$B = 4\epsilon\sigma^m$$

ϵ is the depth of the potential well

σ is the finite distance at which the inter-particle potential is zero

r is the distance between the particles

r^{-n} is the repulsive term

r^{-m} is the attractive term

An alternate expression of the Lennard Jones potential is shown in equation 35

$$V(r) = 4\epsilon \left[\left(\frac{\sigma}{r} \right)^n - \left(\frac{\sigma}{r} \right)^m \right] \quad (35)$$

ϵ is the depth of the potential well

σ is the finite distance at which the inter-particle potential is zero

r is the distance between the particles

r^{-n} is the repulsive term

r^{-m} is the attractive term

A third expression of the Lennard Jones potential is shown in equation
36

$$V(r) = \epsilon \left[\left(\frac{r_0}{r} \right)^n - 2 \left(\frac{r_0}{r} \right)^m \right] \quad (36)$$

r_0 (sometimes written as R_{min}) = $\sqrt[n]{2\sigma}$

ϵ is the depth of the potential well

σ is the finite distance at which the inter-particle potential is zero

r is the distance between the particles

r^{-n} is the repulsive term

r^{-m} is the attractive term

More accurate potentials exist but L-J potentials are widely used in modelling as they offer computational simplicity. When the value of r is small the inter-particle force caused by the electron clouds is repulsive, so at short distances the repulsive term r^{-n} , dominates. However, the r^{-n} term has no theoretical validation; it approximates the Pauli repulsion and is computationally efficient as the square of r^m . At larger distances the r^{-m} term dominates; this models the van der Waals forces and is the attractive part of the potential. Common values of n and m are 12 and 6, though values other than 12 and 6 can be used depending what works best for the system being modelled, such as 9-3 or 9-6.

Buckingham potentials (exp-6 rather than 12-6) replace the repulsive term with an exponential function.^[123] This allows more effective convergence of the value for the repulsive term.

$$V_B = A \exp\left(\frac{-r}{\rho}\right) - \frac{C}{r^6} \quad (37)$$

A , C and ρ are constants

r is the distance between the particles

$\frac{-r}{\rho}$ is the repulsive term

r^{-6} is the attractive term

This thesis has generally used the Lennard-Jones potential to facilitate easier mixing of potentials, on occasion recasting established Buckingham potentials as Lennard-Jones potentials to do this. Atomistic and molecular modelling studies are only useful if the potentials used are good, therefore the testing of existing potentials and the validation of new ones is a significant focus of this work.

2.8 Intramolecular Interactions

Besides intermolecular forces there may be covalent forces within a molecule; this means that intramolecular terms must be included in the simulation to describe these forces. This is demonstrated by example in Chapter 5. The intramolecular potentials describing bond bending, bond vibrations and bond twisting (torsion) must be included. These can be written as:

$$U_{intra} = U_{angles} + U_{bonds} + U_{torsions} \quad (38)$$

2.8.1 Bonding Interactions

The simplest way to describe bond oscillations is to assume the vibrations are purely harmonic. The vibrations can then be described as a simple harmonic oscillator as shown in equation 39

$$U_{r_{ij}} = \frac{1}{2}k(r_{ij} - r_0)^2 \quad (39)$$

Plotting the energy versus the interatomic distance results in a parabolic curve as shown in Figure 12.

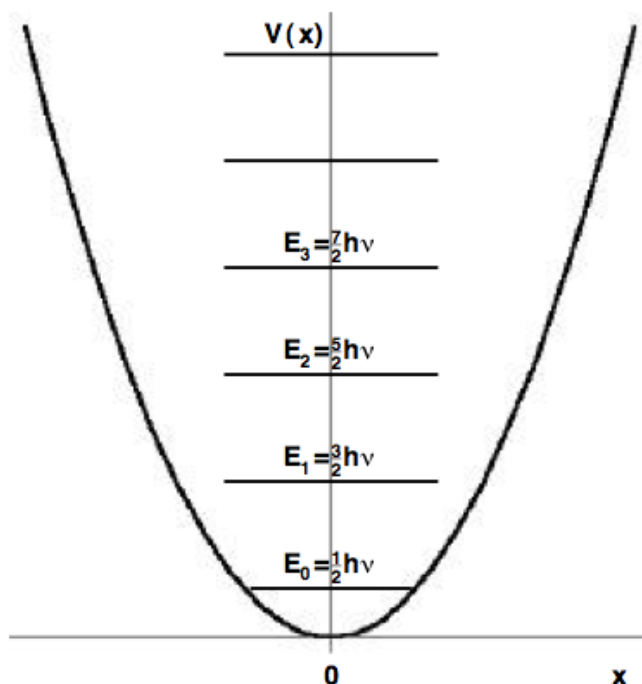


Figure 12: Harmonic oscillator curve of energy versus interatomic distance; in a true vibration system the lowest energy the bond can have is $E_0 = \frac{1}{2}h\nu$

The minimum of the curve represents $r = r_0$, where r_0 is the equilibrium distance, *i.e.* the bond length. Any higher energy levels, such as E_2 , are a result of extension or compression of the bond, which is similar to the behaviour of a spring. When the attractive and repulsive forces are balanced the two atoms will remain at the mean distance apart from each other; this is the point where the energy of the system is at a minimum. The attractive

forces resist the atoms being pulled apart and the repulsive forces resist them being moved closer together, thus energy is required if the bond is to be distorted in either way. Considering the oscillator curve shown in Figure 12, it could be taken that one atom is static at point r_0 ; the other atom would then oscillate laterally along the horizontal line at each energy level, extending and reducing the bond length. It can be seen that as energy levels increase, say from E_1 to E_2 , there is greater scope for the oscillation to extend to the left or right and the variations in bond length become greater. However experimental observation shows that molecules do not completely obey the laws of harmonic motion, and bonds can break when they are extended far enough. Small bond distortions can be said to obey harmonic motion, but once the variations in bond length exceed around 10% a more complex behaviour, requiring a more complex potential, is observed. The Morse potential,^[124,125] developed by Philip Morse, is often used in such cases. The energy is exponentially related to the interatomic spacing (r_{ij}) and the equilibrium distance r_0 . The Morse potential takes the form:

$$U(r_{ij}) = A_{ij}(1 - \exp[-B_{ij}(r_{ij} - r_0)])^2 - A_{ij} \quad (40)$$

where A_{ij} is the bond dissociation energy, r_0 is the equilibrium bond distance and B_{ij} is a function of the slope of the potential energy well and can be determined from spectroscopic data.^[118]

A comparison of the energy versus interatomic distance curves, for the harmonic oscillator and the Morse potential, is shown in Figure 13.

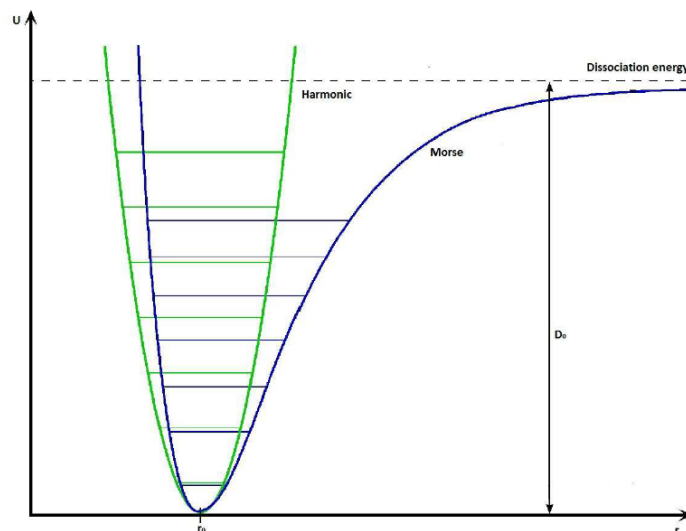


Figure 13: Comparison of energy versus interatomic distance curves for the harmonic oscillator and the Morse potential

An advantage of the harmonic oscillator model is that atoms which are a long way from their equilibrium positions will quickly equilibrate without risk of the bond breaking.

2.8.2 Three-Body Potentials

Where a covalent molecule consists of more than two atoms the bonds will have directionality *i.e.* there will be a bond angle and this must be accounted for. Deviations from the equilibrium value of the bond angle result in an energy penalty and the three-body potential is added to account for this; the potential describes the angle between a central ion, i , and two adjoining ions, j and k . The potential is described in equation 41.

$$U(\theta_{ijk}) = \frac{1}{2}k_{ijk}(\theta_{ijk} - \theta_0)^2 \quad (41)$$

where k_{ijk} is the three-body force constant and θ_0 is the equilibrium angle.

2.8.3 Four-Body Potentials

Four-body potentials are used to account for the effect of torsional angles deviating from their equilibrium value. They take the form:

$$U(\phi_{ijkl}) = k_{ijkl}(1 - \cos(n\phi_{ijkl})) \quad (42)$$

where k_{ijkl} is the four-body force constant, n is equal to 2 and ϕ_{ijkl} is the torsion angle.

2.9 Polarisability

At short interatomic distances there is the possibility of polarisation of the atoms in the system. When an ion comes into close proximity with an electric field a dipole can be induced in the electron charge cloud of the ion. This ionic polarisability can affect the short-range interactions between ions. Rigid ion models consider each ion as a formal point charge and ignore this polarisation.

One method of incorporating the ionic polarisability into the model is to use the shell model, which was developed in 1958 by Dick and Overhauser.^[74]

2.9.1 The Shell Model

The shell model is a simple mechanical model which considers an ion to be represented by two components; these are a positively charged core which contains all the mass of the ion and a negatively charged massless shell. These components are connected by a harmonic spring as represented in Figure 14.

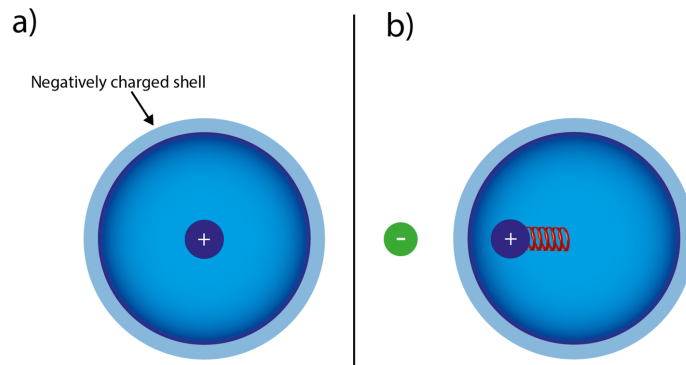


Figure 14: Representation of the shell model. (a) shows an unpolarised ion where the centre of the core and the shell are at the same point. (b) shows a polarised ion where an asymmetric field causes the core and shell to be centred on different points.

The total charge of the ion is the sum of the core and shell charges. The harmonic core-shell potential models the interaction of the positively charged nucleus and negatively charged electron cloud of an ion, as shown in equation 43:

$$U(r_{c-s}) = \frac{1}{2}kr_{c-s}^2 \quad (43)$$

where r is the distance between the core and the shell and k is the spring constant.

The polarisability of the ion is represented as:

$$\alpha = \frac{Y^2}{k} \quad (44)$$

where α is ion polarisability, Y is the shell charge and k is the spring constant.

Comparisons of the rigid ion model and shell model have been made in a number of studies.^[126,127,128] Despite the simplicity of the rigid ion model it has been shown to produce successful results in a wide range of simulations,^[129,130,131] although the shell model often shows better results in comparison. However, the shell model significantly increases the number of particles in the simulation with the result that computational costs can be greatly increased; thus molecular dynamics simulations still very often use the rigid ion model. The rigid ion model is used in this work. The potential parameters used in this work are detailed in each of the results chapters.

Chapter 3 builds on the techniques discussed in this chapter by describing how they can be incorporated into MM energy minimisation techniques and used to calculate relevant information for the system being examined.

3 Energy Minimisation

The computer simulation packages METADISE^[84] and GULP^[132] are used both to perform initial MM energy minimisation on the bulk structures and on surfaces of compounds under consideration. They also enable the generation of inputs that can be used by MD packages such as DL_POLY^[133] and plane-wave DFT codes such as CASTEP^[86]. METADISE also allows manipulation of post-process output from these other simulation packages to produce files for graphical visualisation.

The potential model described in Chapter 2 can be combined with these simulation techniques and used to calculate information of interest regarding the system under investigation. Energy minimisation is a technique to minimise the interaction energy of a system and thus determine that system's equilibrium configuration. It is a quick method and has been used to study mineral structures for many years. The method does not take account of temperature; calculations are effectively carried out at zero Kelvin without the zero-point (ground state) energy.

MD simulations include kinetic energy; the system is allowed to evolve over time and can be studied dynamically. This is a very useful technique for modelling liquids and liquids in contact with mineral surfaces, both of which are critical in this particular project. Solid systems are periodic *i.e.* their structure is regular and repeating; this means the size of the problem being computationally modelled can be reduced by using the periodic boundary condition.

3.1 Energy Minimisation

This project calculates surface and bulk structures and energies using energy minimisation methods. The interaction energy calculated for a system should be the minimum such energy of the system; the system should be at mechanical equilibrium with no residual stress. When setting up a simulation cell this is not usually the case, so energy minimisation routines must be used on the cell. This can be done at constant volume, where the cell dimensions are fixed but the ionic positions can be altered, or it can be done at constant pressure, where ionic positions can be altered and the cell dimensions can change. This can be indicated as the ions being at the positions with minimised energy when all the forces are zero:

$$\frac{\partial U}{\partial \mathbf{r}} = 0 \quad (45)$$

where ∂U is the change in energy and ∂r is the change in the ionic position.

Two methods of achieving the energy minimum in equation 45 are discussed here.

3.1.1 Conjugate Gradients

Conjugate gradient minimisation is an augmentation of the method of steepest descent^[134]. Each minimisation step is directed using information on the

forces from the previous step. Each new position in the steepest descent method is calculated using the formula in equation 46:

$$r_{n+1} = r_n - \alpha_n S_n \quad (46)$$

where r_n is the coordinate at time n , α_n is a constant at each iteration (chosen to optimise efficiency of minimisation) and S_n is the displacement vector. S_n is given by:

$$S_n = -g_n \quad (47)$$

where:

$$g_n = \frac{\partial U}{\partial r_n} \quad (48)$$

The search direction (or displacement vector) in this method is determined from information regarding the previous gradient values:

$$S_n = -g_n + \gamma_n S_{n-1} \quad (49)$$

where:

$$\gamma_n = \frac{g_n^T \cdot g_n}{g_{n-1}^T \cdot g_{n-1}} \quad (50)$$

where T is the transpose of the vector and:

$$S_1 = g_1 \quad (51)$$

When S_n reaches zero, or a value within parameters determined as close enough to zero for accuracy, the minimisation is achieved. This method only uses the first derivative of the energy with respect to the ionic positions and so each iteration is very swift. However, a large number of iterations are required as the algorithm is less effective than matrix techniques such as the Newton-Raphson method.^[135] Even though more steps are required, the conjugate gradient method is usually quicker than matrix methods. DFT codes use the conjugate gradient method, or newer methods derived from it.

3.1.2 Newton-Raphson Method

The Newton-Raphson method is an iterative procedure and struggles for computational cost-effectiveness with large systems. It utilises the second derivative of the energy, U_r , using a Taylor expansion to expand to second order:

$$U(r_{n+1}) = U(r_n) + g_n \cdot \delta r^T + \frac{1}{2} \delta r^T \cdot \mathbf{W}_n \cdot \delta r \quad (52)$$

where δr is the displacement of a given ion:

$$\delta r = r_{n+1} - r_n \quad (53)$$

and \mathbf{W}_n is the second derivative matrix:

$$\mathbf{W}_n = -\frac{\partial^2 U}{\partial r_n^2} \quad (54)$$

Therefore, assuming the energy change with strain to be zero, when the system is at equilibrium:

$$\frac{\partial U}{\partial r} = 0 = g_n + \mathbf{W}_n \cdot \delta r \quad (55)$$

which gives:

$$\delta r = -\mathbf{W}_n^{-1} \cdot g_n \quad (56)$$

and hence:

$$r_{n+1} = r_n - g_n \mathbf{H}_n \quad (57)$$

where \mathbf{H}_n is the Hessian matrix and is equivalent to \mathbf{W}_n^{-1} .

The minimum system energy could be obtained in a single step if the system were absolutely harmonic in r , but if it is anharmonic the displacement will give rise to a lower energy configuration and an iterative process must be used to determine the lowest energy configuration. Because the Newton-Raphson method necessitates the calculation of both derivatives of displacement energy, and the inversion of the matrix of the second derivative of the

energy, it is computationally demanding. Some methods, such as Davidon-Fletcher-Powell (DFP)^[136] or the Broyden-Fletcher-Goldfarb-Shanno algorithm (BFGS),^[137] only work out this matrix at intervals, but they are still computationally taxing; for potential based codes computer speeds have negated the cost to a large extent, but the full Newton-Raphson method would still be prohibitively expensive for DFT methods. The updated approximation of the Hessian matrix is given as:

$$\mathbf{H}_{n+1} = \mathbf{H}_n + \frac{\delta r \cdot \delta r^T}{\delta r^T \cdot \delta g} - \frac{\mathbf{H}_n \cdot \delta g \cdot \delta g^T \cdot \mathbf{H}_n}{\delta g^T \cdot \mathbf{H}_n \cdot \delta g} \quad (58)$$

Because energy minimisation techniques do not take account of temperature effects it is necessary to employ other modelling techniques to allow for these, such as molecular dynamics.

3.2 Molecular Dynamics

As mentioned previously, molecular dynamics simulations involve kinetic energy and are allowed to evolve over time. The simulation requires the solving of Newton's laws of motion for all the particles in the system, over the time allowed. The method was first used in the late 1950's by Alder and Wainwright to study the interactions of hard spheres.^[114,115], whilst the first studies of a realistic system were done in 1974 by Rahman and Stillinger^[138] who simulated liquid water.

At the start of the simulation, the particles are assigned random velocities so that the initial temperature of the system is that required, and so that the cell has no translational momentum. These initial conditions are defined by:

$$\sum_{i=1}^N m_i \cdot v_i^2 = 3Nk_B T \quad (59)$$

and

$$\sum_{i=1}^N m_i \cdot v_i = 0 \quad (60)$$

where N is the number of particles, m_i is the mass of particle i , v_i is the velocity of particle i , k_B is the Boltzmann constant and T is temperature.

Next the forces acting on each particle are calculated by solving Newton's equations of motion; the forces allow calculation of accelerations and velocities and thus the position of each particle can be updated for an infinitely small time-step. The time-step must be small enough to capture molecular vibrations and not allow significant movement of atoms between steps. Newtons' equations of motion are solved by:

$$a_i(t) = \frac{F_i(t)}{m_i} \quad (61)$$

$$v_i(t + \delta t) = v_i(t) + a_i(t)\delta t \quad (62)$$

$$r_i(t + \delta t) = r_i(t) + v_i(t)\delta t \quad (63)$$

where F_i are the forces on particle i and a_i is the acceleration of particle i .

After each step, the run time properties are calculated *e.g.* temperature or potential energy. The whole process is then repeated iteratively over the simulation time, involving thousands or millions of iterations. The early part of the simulation involves equilibration of the system, scaling the particle's velocities to obtain equilibrium at a given temperature and pressure, so as to hold the temperature at the desired level for the simulation; typically this takes a few tens of thousands steps. Once equilibration is achieved the particle velocities are no longer scaled and the simulation is run for as long as possible, to achieve converged values for the properties of interest. MD

simulations facilitate the calculation of a number of system properties, both static and dynamic, as well as free energy. The computer code DL_POLY^[133] was used to perform the MD simulations in this project.

In practice, the errors due to the size of the time step, δt , need to be combated. A large time step would miss molecular vibrations but a short time step can mean too many iterations are needed, thus the simulation time becomes too long and too expensive. Integration algorithms are an effective compromise to offset the time step length against the total simulation time.

3.2.1 Integration Algorithms

The potential energy of a system is a function of the $3N$ coordinates of all the atoms in the system; because of the complex nature of this function there is no analytical solution for Newton's equations of motion and they must be solved numerically. Computer modelling codes use integration algorithms to solve Newton's equations of motion over a finite time-step; an integration algorithm should be able to achieve the desired level of accuracy whilst computing forces at finite time steps as large as possible. The algorithms discussed here use a Taylor expansion to describe the atomic positions, velocities and accelerations:

$$\begin{aligned}
 r(t + \delta t) &= r(t) + v(t)\delta t + \frac{1}{2}a(t)\delta t^2 + \frac{1}{6}b(t)\delta t^3 + \dots \\
 v(t + \delta t) &= v(t) + a(t)\delta t + \frac{1}{2}b(t)\delta t^2 + \dots \\
 a(t + \delta t) &= a(t) + b(t)\delta t + \dots \\
 b(t + \delta t) &= b(t) + \dots
 \end{aligned}
 \tag{64}$$

where r is the position of the particle, v is the velocity of the particle, a is the acceleration of the particle and b is the third time derivative of r . Equation 64 can be used to calculate the particle position about a position $r(t)$ before and after a time step δt :

$$r(t + \delta t) = r(t) + v(t)\delta t + \frac{1}{2}a(t)\delta t^2 + \frac{1}{6}b(t)\delta t^3 + \vartheta(\delta t^4) \quad (65)$$

$$r(t - \delta t) = r(t) - v(t)\delta t + \frac{1}{2}a(t)\delta t^2 - \frac{1}{6}b(t)\delta t^3 + \vartheta(\delta t^4) \quad (66)$$

where $\vartheta(x)$ is the order of accuracy. Adding together equations 65 and 66 gives:

$$r(t + \delta t) + r(t - \delta t) = 2r(t) + a(t)\delta t^2 + \vartheta(\delta t^4) \quad (67)$$

which leads to:

$$r(t + \delta t) = 2r(t) - r(t - \delta t) + \frac{\delta t^2}{m} f(t) + \vartheta(\delta t^4) \quad (68)$$

which is the underlying basis of the Verlet algorithm.^[139] The Verlet algorithm uses the previous and current positions of a particle, along with the current forces acting on the particle, to determine the new position of the particle; this is shown in Figure 15. Velocities are used to estimate the kinetic energy. The velocities can be calculated by subtracting equation 66 from equation 65, to give:

$$r(t + \delta t) - r(t - \delta t) = 2v(t)\delta t + \vartheta(\delta t^3) \quad (69)$$

which gives:

$$v(t) = \frac{r(t + \delta t) - r(t - \delta t)}{2\delta t} + \vartheta(\delta t^2) \quad (70)$$

This means that $r(t + \delta t)$ must be known before velocities can be calculated and that the velocities are subject to error in the order δt^2 . The method can be imprecise due to the addition of the small term $\vartheta(\delta t^2)$ to the difference of larger terms $\vartheta(\delta t)$ in equation 68.

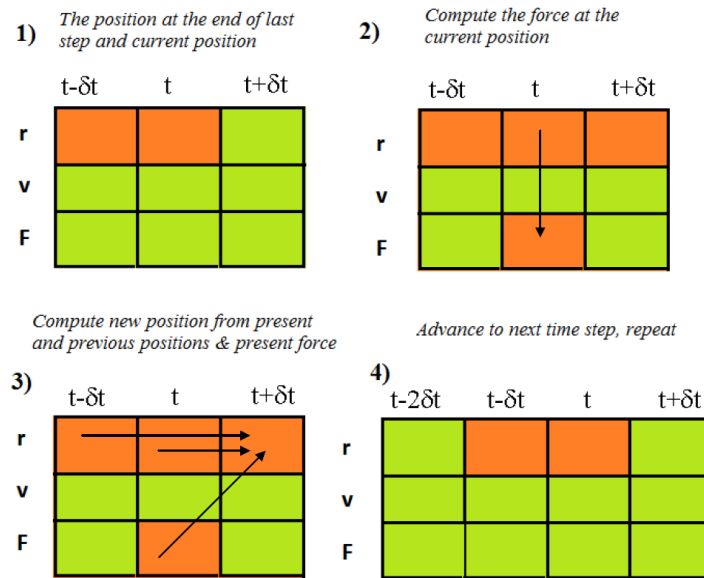


Figure 15: Implementation of the Verlet scheme, showing the successive steps in the method

A modification of the Verlet technique is the Verlet leapfrog algorithm,^[140,141] which considers velocity at half a time step behind. This is shown in equations 71 and 72:

$$v(t + \frac{1}{2}\delta t) = \frac{r(t + \delta t) - r(t)}{\delta t} \tag{71}$$

$$v(t - \frac{1}{2}\delta t) = \frac{r(t) - r(t - \delta t)}{\delta t} \quad (72)$$

which means that equation 68 can be defined as:

$$\frac{r(t + \delta t) - r(t)}{\delta t} = \frac{r(t) - r(t - \delta t)}{\delta t} + \frac{\delta t}{m}f(t) + \vartheta(\delta t^3) \quad (73)$$

then from equations 71 and 72:

$$v(t + \frac{1}{2}\delta t) = v(t - \frac{1}{2}\delta t) + \frac{\delta t}{m}f(t) + \vartheta(\delta t^3) \quad (74)$$

and:

$$r(t + \delta t) = r(t) + v(t + \frac{1}{2}\delta t)\delta t + \vartheta(\delta t^4) \quad (75)$$

The leapfrog algorithm requires positions and forces for the particles at time t and the velocities of the particles at half a time step behind. Equation 74 is used to calculate the new velocities, at which point the velocities "leapfrog" over the coordinates to produce the values for the next half time step velocities, $v(t + \frac{1}{2}\delta t)$. This is illustrated visually in Figure 16.

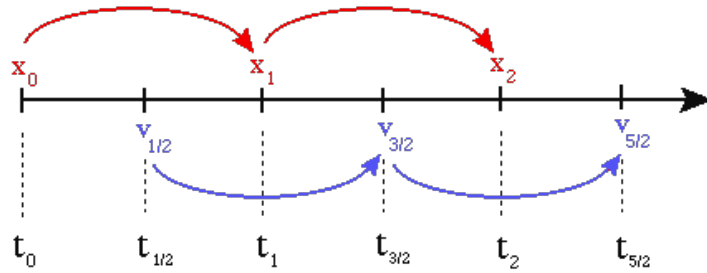


Figure 16: Verlet leapfrog velocity sampling^[142]

The current velocities can be calculated using equation 76:

$$v(t) = \frac{1}{2} \left[v\left(t + \frac{1}{2}\delta t\right) + v\left(t - \frac{1}{2}\delta t\right) \right] \quad (76)$$

Once the velocities have advanced, the positions of the particles can be advanced using equation 75. Because the Verlet leapfrog method does not take the difference of two large quantities to obtain a small one, it has improved numerical precision over the Verlet algorithm.

3.2.2 Ensembles

Ehrenfest's theorem of 1927 has been interpreted in terms of ensembles^[143], as has the work of Boltzmann in 1866^[144]. Allen *et al*^[145] developed a method

to incorporate certain conditions when addressing variables such as temperature, pressure and volume. The conditions of the simulation are known as the ensemble. There are several common variants:

The NVE ensemble – the number of particles, the volume and the energy of the system are kept constant. This is also known as the microcanonical system.

The NVT ensemble – the number of particles, the volume and the temperature of the system remain constant. Also known as the canonical ensemble.

The NPT ensemble – this is also termed the isobaric-isothermal ensemble. The number of particles, the pressure and the temperature of the system are kept constant.

The μ VT ensemble – also known as the grand canonical ensemble, this is where the chemical potential, the volume and the temperature of the system remain constant. This ensemble is mainly used in Monte Carlo simulations.

The microcanonical (NVE) ensemble has a constant number of particles, volume and total system energy and the Hamiltonian of the system is given by:

$$\mathcal{H}_{NVE} = U + K.E. \tag{77}$$

where U is the potential energy and $K.E.$ is the kinetic energy.

The canonical (NVT) ensemble, with constant number of particles, volume and temperature, maintains the temperature using a Nosé-Hoover thermostat,^[146] which acts as a heat bath. The Nosé-Hoover algorithm modifies Newton's equations of motion to include a friction coefficient \mathcal{X} :

$$\frac{d\mathbf{v}(t)}{dt} = \frac{\mathbf{f}(t)}{m} - \mathcal{X}(t)\mathbf{v}(t) \quad (78)$$

The friction coefficient is controlled by the first order differential equation:

$$\frac{d\mathcal{X}(t)}{dt} = \frac{1}{\mathcal{T}_T^2} \left[\frac{T}{T_{ext}} - 1 \right] \quad (79)$$

where \mathcal{T}_T is an arbitrary time constant for variations in temperature, T_{ext} is the temperature of the heat bath and T is the instantaneous temperature. The Verlet leapfrog algorithm can therefore be modified as:

$$\mathcal{X}(t + \frac{1}{2}\delta t) = \mathcal{X}(t - \frac{1}{2}\delta t) + \frac{\delta t}{\mathcal{T}_T^2} \left[\frac{T}{T_{ext}} - 1 \right] \quad (80)$$

$$\mathcal{X}(t) = \frac{1}{2} \left[\mathcal{X}(t - \frac{1}{2}\delta t) + \mathcal{X}(t + \frac{1}{2}\delta t) \right] \quad (81)$$

$$v(t + \frac{1}{2}\delta t) = v(t - \frac{1}{2}\delta t) + \left[\frac{f(t)}{m} - \mathcal{X}(t)v(t) \right] \delta t \quad (82)$$

$$v(t) = \frac{1}{2} \left[v(t - \frac{1}{2}\delta t) + v(t + \frac{1}{2}\delta t) \right] \quad (83)$$

$$r(t + \delta t) = r(t) + v(t + \frac{1}{2}\delta t)\delta t \quad (84)$$

Because $v(t)$ is required to calculate T , which in turn is required to calculate $v(t)$ itself, several iterations are necessary to achieve self-consistency.

The iteration number is set as three within DL_POLY and the initial predictions of $v(t)$ and T are made using the standard Verlet leapfrog algorithm. The conserved quantity in NVT, derived from the Hamiltonian for the system is given by:

$$\mathcal{H}_{NVT} = \mathcal{H}_{NVE} + f k_B T_{ext} \left(\frac{\mathcal{T}_T^2 \mathcal{X}^2(t)}{2} + \int_0^t \mathcal{X}(s) d(s) \right) \quad (85)$$

The isobaric-isothermal (NPT) ensemble, with constant particle number, pressure and temperature, can be isotropic or anisotropic. Isotropic allows the cell dimensions to change but not the cell shape, anisotropic allows both the cell dimensions and cell shape to change. A barostat to control the pressure is introduced into DL_POLY by adjusting the Hoover algorithm with the Melchionna modification;^[147] which calculates the velocities as:

$$\frac{dv(t)}{dt} = \frac{f(t)}{m} - [\mathcal{X}(t) + \eta(t)] v(t) \quad (86)$$

where η is the friction coefficient of the barostat:

$$\frac{d\eta(t)}{dt} = \frac{1}{N k_B T_{ext} \mathcal{T}_p^2} V(t) [P - P_{ext}] \quad (87)$$

where \mathcal{T}_p is an arbitrary time constant for variations in pressure, P is the instantaneous pressure, P_{ext} is the pressure of the barostat and $V(t)$ is the volume of the system at time t , where:

$$\frac{dV(t)}{dt} = [3\eta(t)V(t)] \quad (88)$$

The Verlet leapfrog algorithm can therefore be modified as:

$$\eta(t + \frac{1}{2}\delta t) = \eta(t - \frac{1}{2}\delta t) + \frac{V(t)\delta t}{Nk_B T_{ext}\mathcal{T}_p^2} [P - P_{ext}] \quad (89)$$

$$\eta(t) = \frac{1}{2} \left[\eta(t - \frac{1}{2}\delta t) + \eta(t + \frac{1}{2}\delta t) \right] \quad (90)$$

$$\mathbf{v}(t + \frac{1}{2}\delta t) = \mathbf{v}(t - \frac{1}{2}\delta t) + \left[\frac{\mathbf{f}(t)}{m} - [\mathcal{X}(t) + \eta(t)]\mathbf{v}(t) \right] \delta t \quad (91)$$

$$v(t) = \frac{1}{2} \left[v\left(t - \frac{1}{2}\delta t\right) + v\left(t + \frac{1}{2}\delta t\right) \right] \quad (92)$$

because:

$$\frac{dr(t)}{dt} = v(t) + \eta(t)[r(t) - R_0] \quad (93)$$

where R_0 is the centre of mass of the system. So:

$$r(t + \delta t) = r(t) + \left(v\left(t + \frac{1}{2}\delta t\right) + \eta\left(t + \frac{1}{2}\delta t\right) \left[r\left(t + \frac{1}{2}\delta t\right) - R_0 \right] \right) \delta t \quad (94)$$

where:

$$r\left(t + \frac{1}{2}\delta t\right) = \frac{1}{2} \left[r(t) + r(t + \delta t) \right] \quad (95)$$

As with the NVT ensemble, several iterations are required to achieve self-consistency. This iteration number is set to four in DL_POLY and initial estimates for P , T , $v(t)$ and $r(t + \frac{1}{2}\delta t)$ are made using the standard Verlet leapfrog algorithm. The new cell volume can be obtained from:

$$V(t + \delta t) = V(t)\exp\left[3\delta t\eta\left(t + \frac{1}{2}\delta t\right)\right] \quad (96)$$

The new cell vectors can be obtained from:

$$H(t + \delta t) = H(t)\exp\left[\eta\left(t + \frac{1}{2}\delta t\right)\delta t\right] \quad (97)$$

where H is the cell matrix with columns that are the three vectors of the cell. In the isotropic situation the conserved quantity for the NPT ensemble is:

$$\mathcal{H}_{NPT} = \mathcal{H}_{NVT} + P_{ext}V(t) + \frac{3Nk_B T_{ext}}{2}\eta(t)^2\mathcal{T}_p^2 \quad (98)$$

If anisotropic conditions are used the cell shape is allowed to change by defining η as tensor $\underline{\underline{\eta}}$, which enables the isotropic algorithm to be adjusted.

3.3 Surfaces

Interactions at the surface of green rust and other minerals are a key part of this project and so surface generation must be used. The computer code METADISE was used for the generation of two-dimensional surfaces in this work; it has been used to calculate surface energies using energy minimisation to determine the lowest energy states of each surface.

3.3.1 Mineral Surface Types

Crystal surfaces can be considered as a stack of planes which are periodic in two dimensions. This work uses Miller indices to describe the direction of cut at mineral surfaces.^[148] However, when describing surfaces it is not only the direction of cut which is important, the location of the surface is also crucial. Work by Bertaut showed that when there is a dipole moment in the unit cell which is perpendicular to the surface, the surface energy diverges with increasing depth.^[149] Tasker showed that this divergence to infinity only occurs on certain charged surfaces and described the different surface types that can be generated from different cut locations.^[150] These surfaces are represented in Figure 17.

Surface type 1 consists of neutral planes which contain both anions and cations, there is no dipole perpendicular to the surface. Surface type 2 has charged planes in a symmetrical arrangement with no dipole perpendicular to

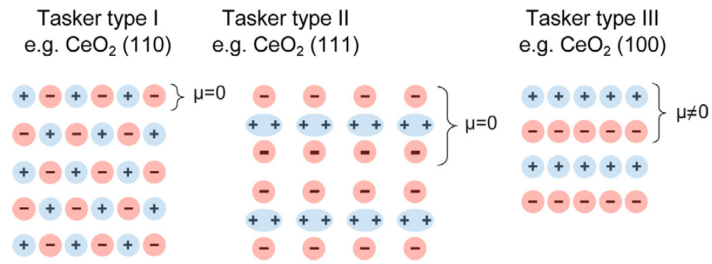


Figure 17: The three types of stacking surface described by Tasker^[151]

the surface. The type 3 surface has a neutral repeat unit but there is a dipole perpendicular to the surface; the surface energy diverges and is infinite which means this type of surface is naturally unstable. Therefore if type 3 surfaces are to be simulated the dipole must be removed. When a polar surface is cut it reconstructs to form a non-polar surface. This could be facilitated by adsorption of other atoms or a redox process, or it could involve faceting of the polar surface. The faceting produces small stable surfaces as shown in Figure 18, where a polar (1 1 1) surface of MgO has reconstructed to form a non-polar surface. This faceting is represented schematically in figure 19.

Similar faceting can be achieved in modelling by removing half of the ions from the top layer of the surface and transferring them to the bottom of the unit cell, a method developed by Oliver *et al*^[153] and shown in Figure 20.

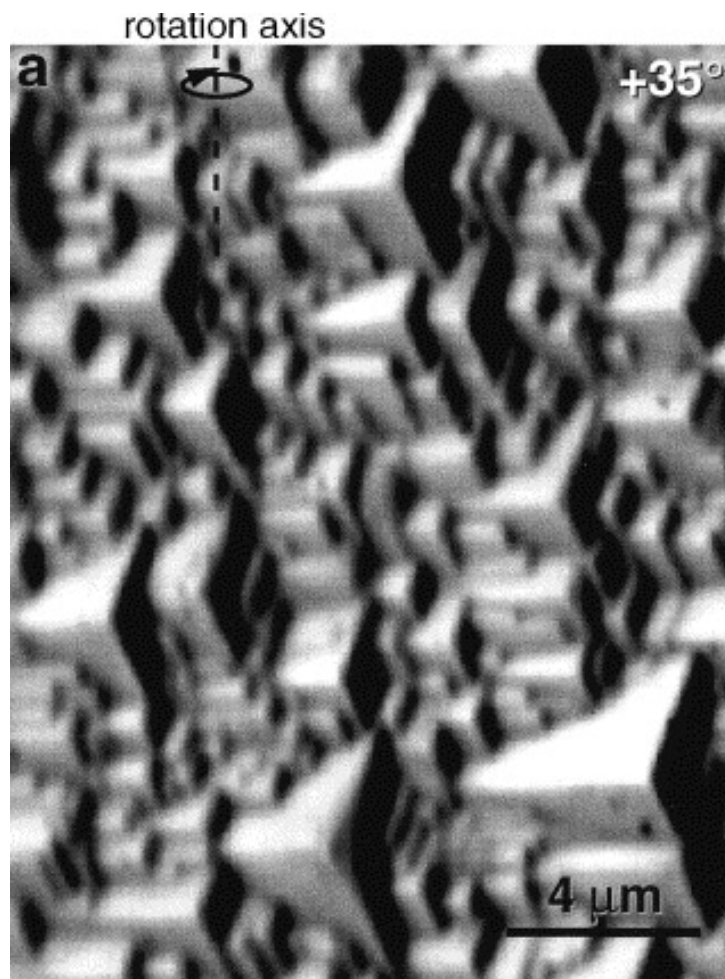


Figure 18: Scanning electron microscope image showing faceting of the polar (1 1 1) MgO surface to produce neutral (1 0 0) surfaces^[152]

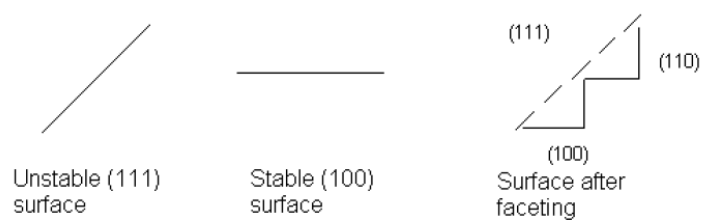


Figure 19: Schematic showing how faceting produces a non-polar surface

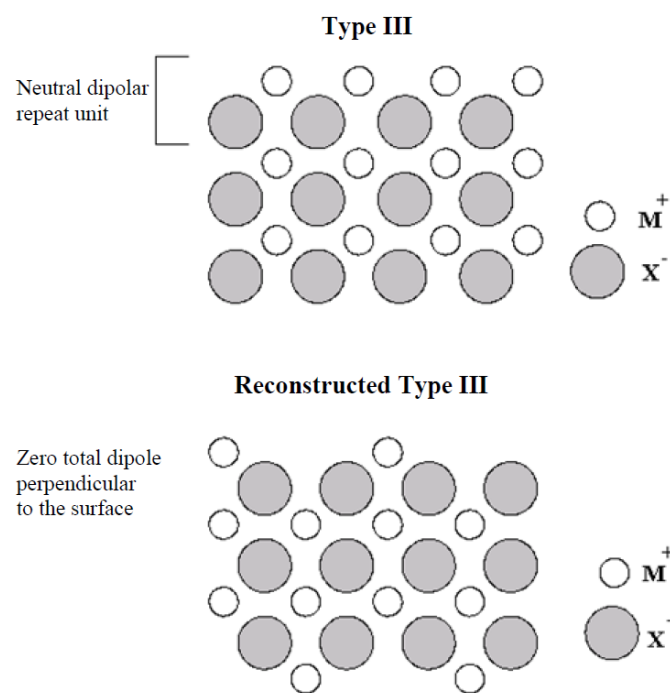


Figure 20: Type 3 surface reconstructed to remove the dipole^[154]

3.3.2 Surface Energy Calculations - Two-dimensional Approach

As previously stated, surface simulations consider a crystal to consist of a series of charged planes which are parallel to the surface and periodic in two dimensions. Building up many of these planes forms the crystal. However it is computationally expensive to simulate each of these planes so METADISE uses the two-region approach developed by Tasker.^[150] The crystal is made up of two blocks, each of which is constituted of two regions; these blocks are periodic in two dimensions.

Region 1 contains the atoms near the surface of the crystal and these can be mechanically relaxed. Region 2 represents the bulk of the crystal and the atomic positions are not relaxed here, they remain at the positions of bulk equilibrium. Two blocks together represent a bulk crystal, but removal of one of the blocks can be used to represent a crystal surface. This is illustrated in Figure 21.

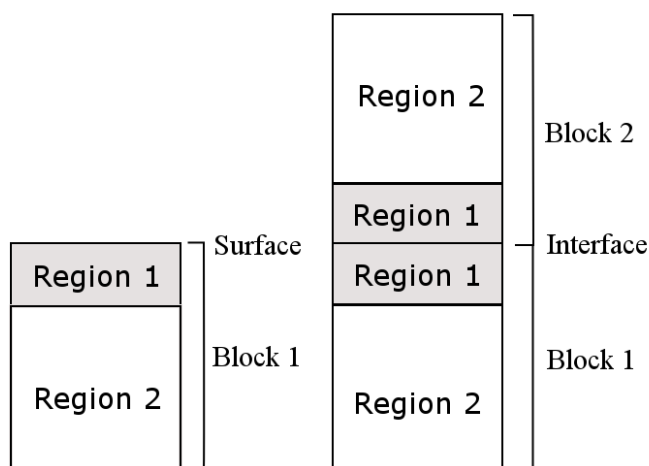


Figure 21: Schematic representation of the two-region approach used by METADISE for surfaces and interfaces^[84]

The total energy of a block consists of the sum of the energy in region 1 and that in region 2. The energy in region 1 can be subdivided into two parts; the interaction energy between all the ions in region 1 and the interaction energy between the ions in region 1 and the ions in region 2. The same is true in region 2, but because the ions in region 2 are held in fixed positions, the interactions between them in this region are taken to be zero. The energy of a block is calculated by summing all the interaction energies of the atoms within that block:

$$U_S = (E_{I-I}^S + E_{I-II}^S) + (E_{II-I}^S + E_{II-II}^S) \quad (99)$$

where the first term represents the atoms in region 1 and the second term represents the atoms in region 2. For example, E_{I-II}^S is the energy of the atoms in the surface of region 1 interacting with the atoms in the surface of region 2. A similar method can be applied to calculate the energy of the bulk:

$$U_B = (E_{I-I}^B + E_{I-II}^B) + (E_{II-I}^B + E_{II-II}^B) \quad (100)$$

The slab method can also be used; the method for calculating the surface energy is to evaluate the total energy of a slab of the material of interest

(generally with a thickness between 5 to 15 layers) and to subtract from that the bulk energy obtained from a separate calculation. This procedure singles out the total energy contribution due to the presence of the surface^[155]. The Coulomb sum is only provisionally convergent for a 2-D slab, so an analogous approach to the Ewald sum is frequently taken, originally devised by Parry^[120,119]; the METADISE code contains the Parry sum.

The surface energy is the excess energy of the surface compared to the energy of the bulk for the same number of atoms, per unit area. It is given by:

$$\gamma = \frac{U_S - U_B}{A} \quad (101)$$

U_S is the energy of the surface block, U_B is the energy of the bulk crystal containing the same amount of atoms as the surface block, A is the surface area. METADISE allows relaxation of the surface, cut along Miller indices, to produce the surface with the most energetically favourable arrangement.

3.3.3 Surface Energy Calculations - Three-dimensional Approach

The three-dimensional Ewald method is very quick and efficient in comparison with the two-dimensional Parry method, so when undertaking surface molecular dynamics calculations using DL_POLY a particular application of the three-dimensional periodic boundary condition is used. The system is first allowed to relax to the bulk structure, then is it orientated so that two

of the lattice vectors are parallel to the surface. This means the third lattice vector is perpendicular to the surface; this vector is increased in size, which introduces a vacuum gap into the crystal structure and results in repeating crystal slabs. The system, including the vacuum gap, is treated as a 3-D periodic system. The chosen surfaces are therefore on opposite sides of the slabs and so the thickness of the slab and the vacuum gap must be sufficient that the periodic images do not interact with each other. Once convergence testing has been used to determine suitable dimensions for the vacuum gap and slab, energy minimisation can be used to relax the surfaces in the system. This method takes advantage of the efficiency of summing Coulombic energy for a three-dimensional system. When simulating a crystal slab in vacuum DL_POLY can utilise either the NVT or NVE ensemble as the volume must be kept fixed; if it were not, the slabs would reform the more energetically favourable bulk structure.

4 Iron (II) Hydroxide and Goethite

Green rust is a complex mineral to model so this project begins by first modelling the simpler minerals iron (II) hydroxide ($\text{Fe}(\text{OH})_2$) and goethite ($\text{FeO}(\text{OH})$). Iron (II) hydroxide is a layered double hydroxide (LDH), though simpler in structure than the LDH green rust. LDH's have a generic sequence of layers $[\text{AcBZAcB}]_n$ where c is the metal cation layer, Z is a layer of anions and neutral molecules (such as water) and A and B are hydroxide layers either side of the metal cation layer. Goethite is a naturally occurring mineral and can be formed by the oxidation of green rust. The aim of this chapter is to investigate the bulk and low index surfaces of these minerals using plane wave DFT and a variety of potential models to develop potential parameters which will form the basis of further study in chapter 6. The bulk structure and five different surfaces of $\text{Fe}(\text{OH})_2$ were investigated, with varying vacuum gap size above the surface, and the results presented. Next, the results from investigating the bulk and seven different surfaces of goethite were considered.

4.1 Iron (II) Hydroxide Crystal Structure

Iron (II) hydroxide is a LDH (see Figure 22) with the brucite ($\text{Mg}(\text{OH})_2$) or portlandite ($\text{Ca}(\text{OH})_2$) configuration whose pure form is not found in nature; its closest natural analogue is the rare mineral amakinite $(\text{Fe}, \text{Mg})(\text{OH})_2$. Under anaerobic conditions it can be oxidised by water protons to form magnetite (Fe_3O_4), and under aerobic conditions it can oxidise to form green rust, before further oxidising to form goethite ($\text{FeO}(\text{OH})$). However, it has been

produced under experimental conditions,^[33,156,157,158,159] which has allowed the reporting of a hexagonal structure,^[160,161,162] as represented in Figure 23, with space group $P\bar{3}m1$.

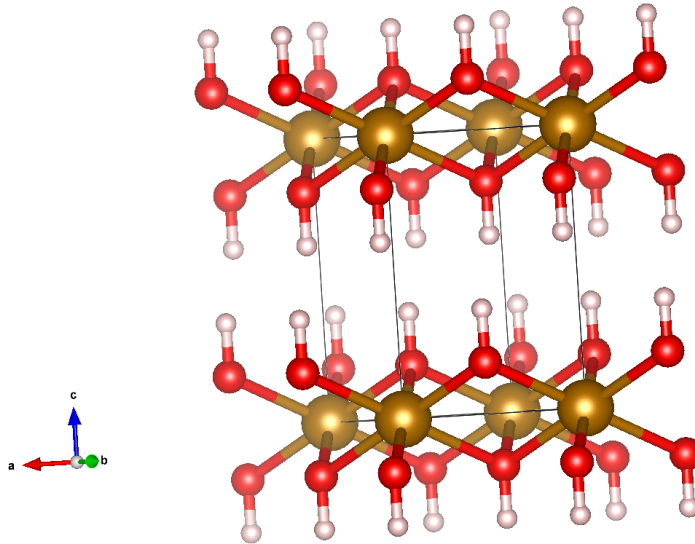


Figure 22: Layered double hydroxide typical structure. In the a and b directions are planes of $\text{Fe}(\text{OH})_2$, in the c direction the structure is dominated by weaker hydrogen bonds from the OH groups in the gaps between the layers.

The oxides and hydroxides of iron were studied by Bernal *et al*^[162] using X-ray diffraction and their results for $\text{Fe}(\text{OH})_2$ are shown in Table 1.

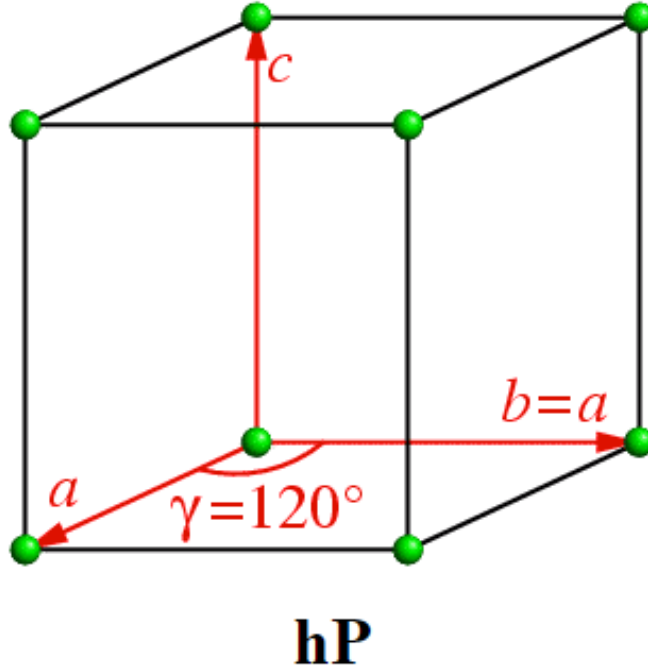


Figure 23: Schematic of a hexagonal Bravais lattice, where $a = b \neq c$ and $\alpha = \beta = 90^\circ$ and $\gamma = 120^\circ$

Table 1: $\text{Fe}(\text{OH})_2$ experimentally determined cell parameters^[162]

Fe(OH) ₂ cell parameters	
a (Å)	3.26
b (Å)	3.26
c (Å)	4.60
α (°)	90
β (°)	90
γ (°)	120

To verify and compare existing potential models and DFT calculations the

experimentally determined cell configuration was taken and the METADISE code used to generate DFT input files for use in CASTEP. PBEsol pseudopotentials^[95] were used for convergence testing of the DFT final free energy results; PBEsol is a revised Perdew-Burke-Ernzerhof GGA^[92] that improves equilibrium properties of densely-packed solids and their surfaces. It was determined that a 4 4 4 k-point grid with a 650eV cut-off value was acceptable, giving convergence to within 0.02eV as shown in Table 2.

Table 2: Fe(OH)₂ convergence testing of DFT calculations

k-point grid	Final free energy (eV)					
	plane-wave cut-off energy (eV)					
	300	400	500	600	650	750
3 3 3	-1753.19	-1762.80	-1767.04	-1766.23	-1766.30	-1766.31
4 4 4	-1751.20	-1762.84	-1765.64	-1766.25	-1766.30	-1766.32
5 5 5	-1751.18	-1762.83	-1765.76	-1766.25	-1766.30	-1766.31
6 6 6	-1753.16	-1763.35	-1765.76	-1766.25	-1766.30	-1766.32

A graphical representation of the convergence is shown in Figure 24.

The converged values were used to run a full DFT geometry optimisation; different potential sets were used to determine the best set to use going forward. PBEsol, on-the-fly (OTF), PBE_recpot and PBE_pseudo_D potential parameters were tested and showed that the PBE_pseudo_D potential set was able to most closely reproduce the experimental cell sizes; the cell angles were reproduced to within 0.02% and the a, b and c parameters to within 0.87%, 4.56% and 2.17% respectively. The next closest results were produced

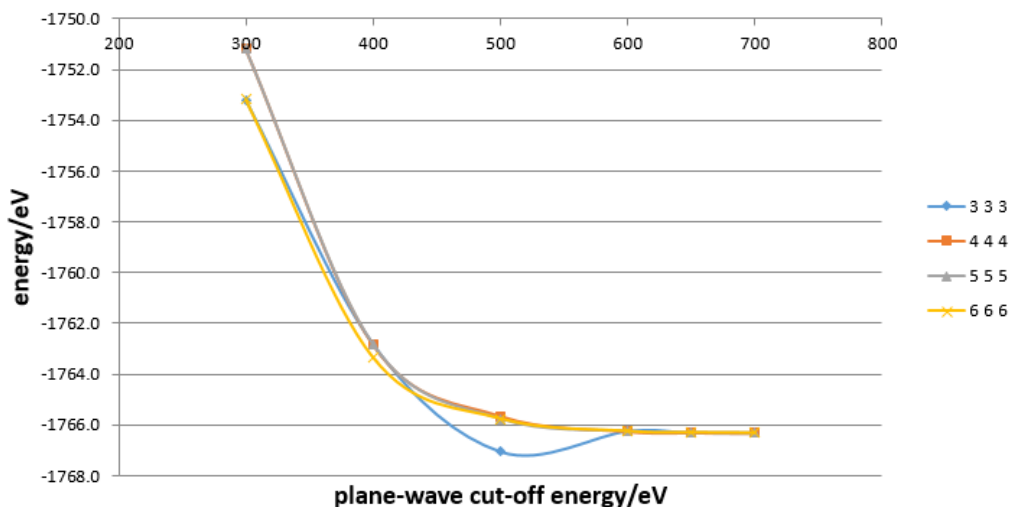


Figure 24: Graphical representation of convergence testing for the bulk structure of $\text{Fe}(\text{OH})_2$

from the PBE_recipot potentials with a, b and c parameters reproduced to within 3.68%, 3.68% and 2.61% respectively, though the cell angles were all around 2.3% different to experimental results. Whilst the PBEsol potentials were able to exactly reproduce the cell angles, the a, b and c parameters were 6.44%, 6.44% and 9.35% away from experimental values respectively. The results from testing these different parameters are shown in Table 3. The Hubbard value in the DFT cell file, which affects the movement of the d and f electrons, was found to give a marginally better result if set to 4.4 for the d electrons of iron, so this value was retained alongside the PBE_pseudo_D potential; this value could be considered practically arbitrary as it only affected the c parameter of the cell, improving the value compared to experimental by $1.9 \times 10^{-5} \text{\AA}$.

Table 3: Fe(OH)₂ experimentally determined cell parameters compared to DFT modelling results (experimental: $a = b \neq c$ and $\alpha = \beta \neq \gamma$)

Results from	Cell dimensions (Å)			% difference to experiment			Cell angles (°)			% difference to experiment		
	a	b	c	a	b	c	α	β	γ	α	β	γ
Experiment	3.26	3.26	4.60	-	-	-	90.00	90.00	120.00	-	-	-
PBEsol	3.05	3.05	4.17	-6.44	-6.44	-9.35	90.00	90.00	120.00	0.00	0.00	0.00
PBE_recipot	3.14	3.14	9.32	-3.68	-3.68	102.61	92.04	87.96	122.67	2.27	-2.27	2.23
PBE_pseudo_D	3.11	3.11	4.56	-0.87	4.56	-2.17	90.02	89.98	120.01	0.02	-0.02	0.01
OTF	3.08	2.67	4.26	-7.39	-18.10	-2.61	90.03	89.97	120.02	-0.03	-0.03	0.01

The experimentally determined structure was optimised in METADISE using the rigid ion CLAYFF potentials,^[51] a rigid ion model based on the work of Baram and Parker^[163] which was modified and refitted^[71,70,164] and a shell model based from the work of Lewis and Catlow^[106], which also comes from the Baram and Parker work^[163]. The ionic charges and potential parameters were varied slightly from the original values on the CLAYFF, rigid and shell models. The CLAYFF potential parameters used are detailed in Tables 4 to 6.

Table 4: Partial charges (q_u) on ions used in the testing and development of interatomic potentials for Fe(OH)₂, CLAYFF potentials

Species	
Ion	Charge (e)
Iron (Fe)	1.330
Hydroxide Oxygen (Oh)	-1.090
Hydrogen (H)	0.425

Table 5: Lennard-Jones potentials for Fe(OH)₂, CLAYFF potentials

Lennard-Jones potentials $A_{ij}r_{ij}^{-12} - B_{ij}r_{ij}^{-6}$			
Ion pair (ij)	A_{ij} (eV Å ¹²)	B_{ij} (eV Å ⁶)	Reference
Fe-Fe	225.1652853	0.018779573	[51]
Oh-Oh	27290.95482	27.12256792	[51]
Fe-Oh	3195.83262	0.810345514	[51]

Table 6: Harmonic potentials for Fe(OH)₂, CLAYFF potentials

Harmonic potentials $k_{ij}/2(r_{ij} - r_0)^2$			
Species (ij)	k_{ij} (eV Å ⁻²)	r_0 (Å)	Reference
Oh-H	48.059	1.00	[51]

Tables 7 to 10 show the shell model potentials based on the work of Lewis and Catlow.

Table 7: Partial charges (q_u) on ions used in the testing and development of interatomic potentials for Fe(OH)₂, based on the shell model of Lewis and Catlow

Species	
Ion	Charge (e)
Iron (Fe)	2.00
Hydroxide Oxygen (Oh) core	0.90
Hydroxide Oxygen (Oh) shell	-2.30
Hydrogen (H)	0.40

Table 8: Buckingham potentials for Fe(OH)₂, based on the shell model of Lewis and Catlow

Buckingham Potentials $A_{ij} \exp(-r_{ij}/\rho_{ij}) - (C_{ij}/r_{ij}^6)$				
Ion pair (ij)	A_{ij} (eV)	ρ_{ij} (Å)	C_{ij} (eV Å ⁶)	Reference
Fe (core)-Oh (shell)	530.00	0.3399	0.00	[70]
H (core)-Oh (shell)	311.97	0.2500	0.00	[70]
Oh (shell)-Oh (shell)	22764.30	0.1490	6.97	[70]

Table 9: Morse potentials for Fe(OH)₂, based on the shell model of Lewis and Catlow

Morse potentials $D_{ij}[\{1 - \exp(-\alpha_{ij}(r_{ij} - r_0))\}^2 - 1]$					
Ion pair (ij)	D_{ij} (eV)	α_{ij} (Å ⁻¹)	r_0 (Å)	Coul.Sub (%)	Reference
H (core)-Oh (shell)	7.0525	3.1749	0.9258	0.00	[70]

Table 10: Harmonic potentials for Fe(OH)₂, based on the shell model of Lewis and Catlow

Harmonic potentials $k_{ij}/2(r_{ij} - r_0)^2$			
Species (ij)	k_{ij} (eV Å ⁻²)	r_0 (Å)	Reference
Oh (core)-Oh (shell)	74.92038	0.00	[106]

Tables 11 to 13 show the rigid ion potentials based on the work of Baram and Parker.

Table 11: Partial charges (q_u) on ions used in the testing and development of interatomic potentials for $\text{Fe}(\text{OH})_2$, based on the rigid ion model of Baram and Parker

Species	
Ion	Charge (e)
Iron (Fe)	2.00
Hydroxide Oxygen (Oh)	-1.40
Hydrogen (H)	0.40

Table 12: Lennard-Jones potentials for $\text{Fe}(\text{OH})_2$, based on the rigid ion model of Baram and Parker

Lennard-Jones potentials $A_{ij}r_{ij}^{-12} - B_{ij}r_{ij}^{-6}$			
Ion pair (ij)	A_{ij} (eV \AA^{12})	B_{ij} (eV \AA^6)	Reference
Fe-Oh	517.50	0.3399	[163]
Oh-Oh	22764.00	0.1490	[163]
H-Oh	311.97	0.2500	[163]

Table 13: Morse potentials for $\text{Fe}(\text{OH})_2$, based on the rigid ion model of Baram and Parker

Morse potentials $D_{ij}[\{1 - \exp(-\alpha_{ij}(r_{ij} - r_0))\}^2 - 1]$					
Ion pair (ij)	D_{ij} (eV)	α_{ij} (\AA^{-1})	r_0 (\AA)	Coul.Sub (%)	Reference
H-Oh	7.0525	3.1749	0.9258	0.00	[163]

Table 14 compares the results of the optimisations and also includes the

closest DFT result for comparison.

Table 14: Fe(OH)₂ experimentally determined cell parameters compared to interatomic potential modelling results (experimental: $a = b \neq c$ and $\alpha = \beta \neq \gamma$)

Results from	Cell dimensions (Å)			% difference to experiment			Cell angles (°)			% difference to experiment		
	a	b	c	a	b	c	α	β	γ	α	β	γ
Experiment	3.26	3.26	4.60	-	-	-	90.00	90.00	120.00	-	-	-
CLAYFF rigid ion	3.25	3.25	4.63	-0.31	-0.31	0.65	90.00	90.00	120.00	0.00	0.00	0.00
Rigid ion	3.25	3.25	4.50	-0.31	-0.31	-2.17	90.00	90.00	120.00	0.00	0.00	0.00
Shell model	3.26	3.26	4.48	0.00	0.00	-2.61	90.00	90.00	120.00	0.00	0.00	0.00
PBE_pseudo_D	3.11	3.11	4.56	-0.87	4.56	-2.17	90.02	89.98	120.01	0.02	-0.02	0.01

Although there is limited experimental data for pure Fe(OH)₂ the potential parameters used were all able to reproduce reported structures with a and b parameters between 0% and 0.31% difference to experiment and the c parameter from the CLAYFF potentials was within 0.65% difference (other potentials produced c parameters of between 2.17% and 2.61% difference to experiment). The DFT results using the PBE_pseudo_D potential set were unable to obtain as close a match to experiment as the interatomic potential method, with a, b and c parameters varying from experimental by 0.87%, 4.56% and 2.17% respectively. Having determined the suitability of CLAYFF potentials for modelling the bulk structure of Fe(OH)₂ they were then used for modelling Fe(OH)₂ surfaces.

4.2 Iron (II) Hydroxide Surfaces

The low index planes investigated were of Miller indices (0 0 1), (0 1 0), (0 1 1), (1 1 0) and (1 1 1). These surfaces were generated from the DFT relaxed cell using METADISE. Once the surfaces were generated METADISE was

again utilised to prepare DFT input, so that slabs terminating in each of the surface types could be modelled and investigated. The first investigation for each slab was to optimise the vacuum gap above the surface using convergence testing. A slab of 4 unit cells thickness was taken for each surface and the vacuum gap varied from 20Å to 35Å in 5Å increments; the results for total energy (corrected for finite basis set) were then compared for convergence and are shown in Table 15.

Table 15: Vacuum gap convergence testing for the low index Miller surfaces of Fe(OH)₂

	Vacuum gap (Å)			
	20	25	30	35
Surface	Total energy (-eV)			
(0 0 1)	5962.54	5962.51	5962.51	5962.51
(0 1 0)	5962.53	5962.51	5962.51	5962.51
(0 1 1)	10429.24	10429.22	10429.23	10429.23
(1 1 0)	14902.11	14902.10	14902.10	14902.10
(1 1 1)	16392.81	16392.79	16392.78	16392.78

Convergence to less than one hundredth of an electron volt was observed for the (0 0 1), (0 1 0), (1 1 0) and (1 1 1) surfaces at a 25Å vacuum gap; similar convergence was seen for the (0 1 1) surface with a 30Å vacuum gap.

To compare surface energy trends for the different Miller indices the thickness of region 1 in the two region system, as discussed in Chapter 3, must be optimised for a relaxed system; testing was carried out to find the converged

value of γ_{min} as the size of region 1 was varied for each different surface under investigation. This was done by running a geometry optimisation of each slab using METADISE, with the value for region 1 initially set to a thickness of 3 unit cells. This produced a surface energy value in $\text{eV}/\text{\AA}^2$ which was then manually converted to J/m^2 . As also discussed in Chapter 3, the surface energy is the excess energy of the surface compared to the energy of the bulk for the same number of atoms, per unit area. It is given by equation 101.

Because the surface energy was for a region 1 thickness of 3 unit cells the bulk energy which was calculated earlier must also be multiplied by 3, so that it is for the same number of atoms as the surface energy. The bulk energy value is subtracted from the surface energy value and the resultant value divided by the surface area of the particular cut through the unit cell. This process was then repeated using METADISE, with the value for region 1 increased by an integer of 1, for values of 4, 5 and 6; the overall slab thickness was increased by the same amount each time to maintain a constant value for region 2. Each time the slab was increased in thickness the vacuum gap above the surface was increased by 5\AA to allow for the extra unit cell that was added to the slab thickness since vacuum gap convergence testing. The resultant figures could then be compared for each surface to investigate surface energy trends; the actual energy values are not important as they vary depending upon potential sets and software used, but the trends of the values are useful indicators of relative surface stability. The DFT convergence testing results for the thickness of region 1 are shown in Tables 16 to 20.

Table 16: Region 1 thickness convergence testing for the (0 0 1) Miller surface of $\text{Fe}(\text{OH})_2$

(0 0 1) Miller surface	
Thickness of Region 1 (unit cells)	Energy difference between surface and bulk (J/m^2)
3	0.14
4	0.14
5	0.14
6	0.14
Converged value for Region 1 thickness (unit cells)	3

Table 17: Region 1 DFT thickness convergence testing for the (0 1 0) Miller surface of $\text{Fe}(\text{OH})_2$

(0 1 0) Miller surface	
Thickness of Region 1 (unit cells)	Energy difference between surface and bulk (J/m^2)
3	0.08
4	0.08
5	0.08
6	0.08
Converged value for Region 1 thickness (unit cells)	3

Table 18: Region 1 DFT thickness convergence testing for the (0 1 1) Miller surface of Fe(OH)₂

(0 1 1) Miller surface	
Thickness of Region 1 (unit cells)	Energy difference between surface and bulk (J/m ²)
3	1.44
4	3.70
5	1.44
6	1.44
Converged value for Region 1 thickness (unit cells)	3

Table 19: Region 1 DFT thickness convergence testing for the (1 1 0) Miller surface of Fe(OH)₂

(1 1 0) Miller surface	
Thickness of Region 1 (unit cells)	Energy difference between surface and bulk (J/m ²)
3	2.53
4	2.43
5	2.10
6	2.05
Converged value for Region 1 thickness (unit cells)	6

Table 20: Region 1 DFT thickness convergence testing for the (1 1 1) Miller surface of Fe(OH)₂

(1 1 1) Miller surface	
Thickness of Region 1 (unit cells)	Energy difference between surface and bulk (J/m ²)
3	2.40
4	1.99
5	2.00
6	1.98
Converged value for Region 1 thickness (unit cells)	4

The energy value for the (0 1 1) Miller surface in Table 18, where Region 1 is 4 unit cells thick, appears anomalous when compared to the other results in the table; this was checked and repeat testing produced the same energy value. The reason for this anomaly was not determined.

Using the region 1 thickness values from the DFT convergence testing, the same Miller surfaces were relaxed to their minimum energy states using METADISE; the previously tested rigid ion and shell model potentials were utilised and the energy trends for the different surfaces compared. These trends are displayed in Table 21.

Table 21: Surface energy trend comparison for the low index Miller surfaces of $\text{Fe}(\text{OH})_2$. Figures in square brackets represent the lowest to highest energy trends within each set of results.

Energy difference between surface and bulk (J/m^2)				
Parameter set				
Miller surface	Shell model	Rigid ion	CLAYFF rigid ion	DFT PBE_pseudo_D
(0 0 1)	0.08 [1]	0.07 [1]	0.29 [1]	0.14 [2]
(0 1 0)	0.43 [3]	0.40 [2]	0.55 [3]	0.08 [1]
(0 1 1)	0.41 [2]	0.40 [2]	0.49 [2]	1.44 [3]
(1 1 0)	0.71 [5]	0.73 [5]	0.80 [5]	2.05 [5]
(1 1 1)	0.68 [4]	0.70 [4]	0.56 [4]	1.98 [4]

As mentioned earlier in this chapter, the numerical values are less critical than the trend of the values; the latter is the more useful information when comparing the likely stability of different surfaces. The lower the value in Table 21, the more stable the Miller surface is, relative to the other surfaces using the same potentials.

It can be seen that the (0 0 1) surface of $\text{Fe}(\text{OH})_2$ is the most stable for each of the interatomic potential sets. The (0 0 1) surface using the CLAYFF potentials is shown in figure 25.

The next most stable are the (0 1 0) and (0 1 1) surfaces, with the results for these two surfaces being very close to each other for the interatomic potential sets. The (0 1 1) surface using the CLAYFF potentials is shown as an example in figure 26.

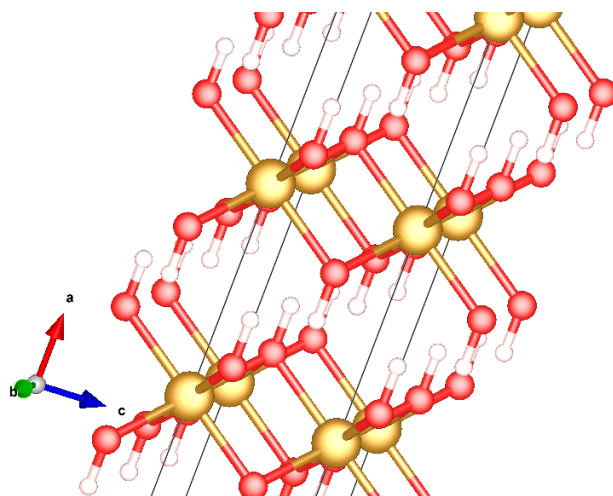


Figure 25: $\text{Fe}(\text{OH})_2$ (0 0 1) surface, perpendicular to lattice vector a , generated from CLAYFF potentials. The spacing between the layers of Fe is 4.63 Å

The DFT results vary slightly for these first three surfaces, showing the (0 1 0) surface to be the most stable, marginally more so than the (0 0 1); the (0 1 1) result from DFT suggests this to be the third most stable of the surfaces investigated. Images of the (0 0 1) and (0 1 1) surfaces generated from DFT are shown in figures 27 and 28 respectively.

The reason for the difference in the stability ordering of the DFT results is unclear and would require further investigation beyond the scope of this chapter, but one possible reason could be that DFT has no direct mechanism to account for dispersive van der Waals forces and must rely on best-fit potentials to try and recreate the effects without the mechanism. The relaxation of the structures when cutting surfaces appear similar when using potentials or DFT, with DFT generally having a slightly smaller spacing between the layers of $\text{Fe}(\text{OH})_2$. Physical studies of brucite (isostructural with $\text{Fe}(\text{OH})_2$) show that the preferred surface is the (0 0 1)^[165,166]; this, along

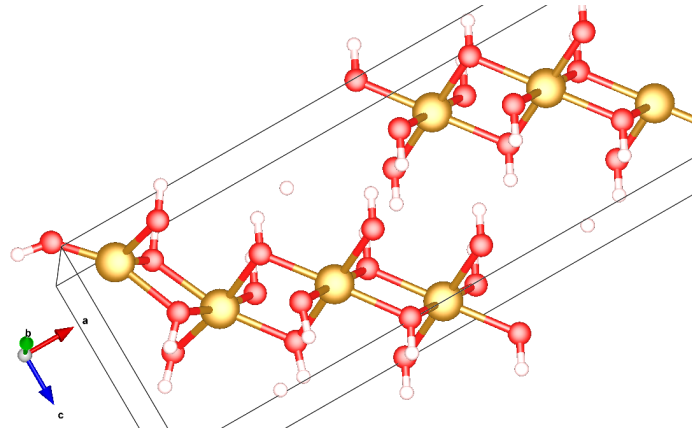


Figure 26: $\text{Fe}(\text{OH})_2$ (0 1 1) surface, perpendicular to lattice vector a , generated from CLAYFF potentials. The spacing between the layers of Fe is 4.97 Å

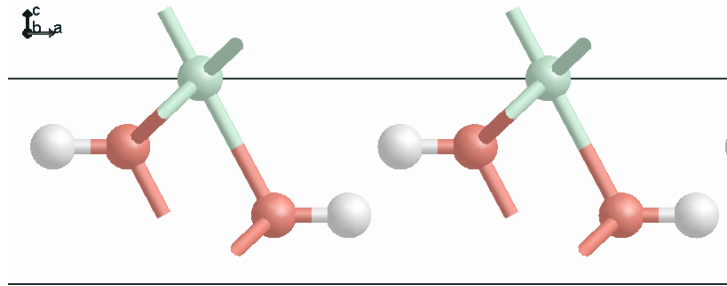


Figure 27: $\text{Fe}(\text{OH})_2$ (0 0 1) surface, perpendicular to lattice vector a , generated from DFT. The spacing between the layers of Fe is 4.57 Å

with the known difficulties that DFT has in modelling layered structures, validates the results of the interatomic potential model in determining the (0 0 1) surface as the most stable.

The results for the (1 1 0) surface show this to be the least stable for all the interatomic potential sets and the DFT calculations, with the (1 1 1) surface more stable than the (1 1 0) by between 0.03 and 0.14 J/m² in each case.

It has been shown that interatomic potentials can successfully be used

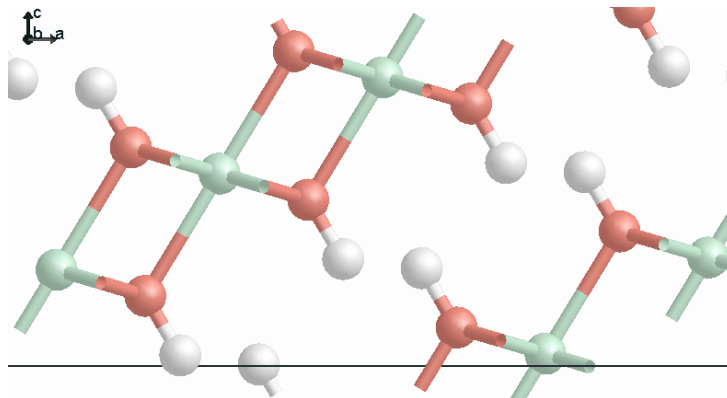


Figure 28: $\text{Fe}(\text{OH})_2$ (0 1 1) surface, perpendicular to lattice vector a , generated from DFT. The spacing between the layers of Fe is 4.90 Å

to model the bulk and low index Miller surfaces of $\text{Fe}(\text{OH})_2$, with greater accuracy than DFT calculation allows for bulk modelling, when compared with experimental data. For ease of mixing potentials in further investigation of green rust it would be ideal to utilise existing potential sets where possible; the modelling of the bulk and low index Miller surfaces of $\text{Fe}(\text{OH})_2$ has demonstrated that the CLAYFF interatomic potentials are suitable for use in these investigations.

4.3 Goethite Crystal Structure

Following modelling of $\text{Fe}(\text{OH})_2$ the interatomic potential sets were tested further by the modelling of goethite (see Figure 29). This was pertinent because green rust has Fe^{2+} and Fe^{3+} in its structure and the modelling of $\text{Fe}(\text{OH})_2$ involved only Fe^{2+} ; thus modelling to test Fe^{3+} potentials was required. Goethite is a relevant mineral to test the potentials because in an oxidising environment green rust usually turns into the Fe^{3+} oxyhydroxides goethite ($\alpha\text{-FeOOH}$) and lepidocrocite ($\gamma\text{-FeOOH}$).^[167]

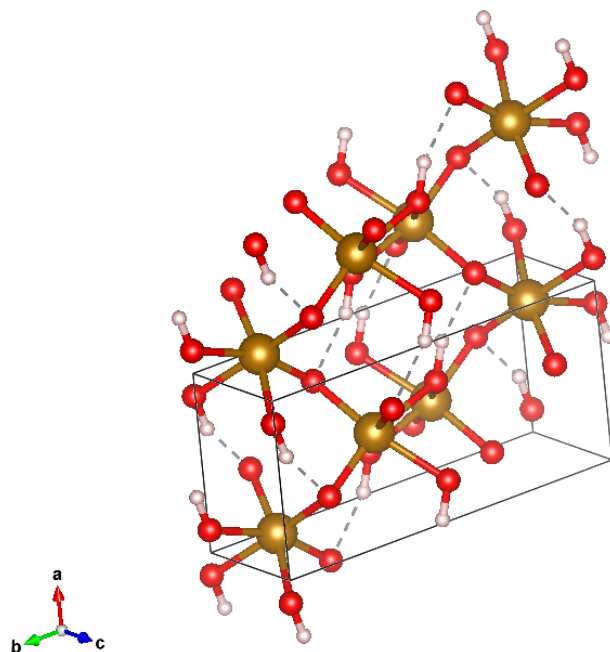


Figure 29: Goethite structure. The planes of Fe are linked by bonds to oxygen atoms. Weaker hydrogen bonds from the OH groups are present in the structure.

Goethite has an orthorhombic structure, represented in Figure 30, with space group $Pbnm$.

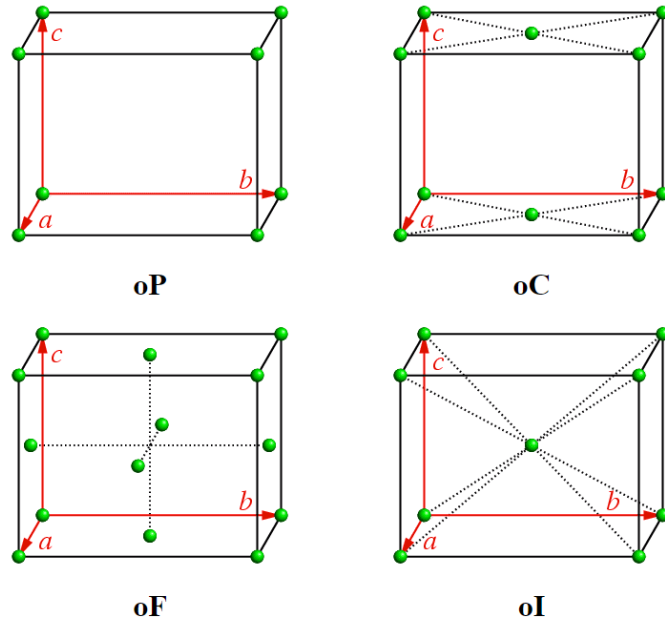


Figure 30: Schematic of an orthorhombic Bravais lattice, where $a \neq b \neq c$ and $\alpha = \beta = \gamma = 90^\circ$. An orthorhombic lattice may be either primitive or centred in one of three different ways: C-face centred, body-centred, or all-face centred

The cell parameters of goethite have been reported in several experimental studies.^[168,169,170,171] The reported experimental cell parameters from the Handbook of Mineralogy^[166] were used for comparison to simulation results and are shown in Table 22.

Table 22: Goethite (α -FeOOH) experimentally determined cell parameters^[166]

α -FeOOH cell parameters	
a (Å)	4.608
b (Å)	9.956
c (Å)	3.0215
α (°)	90
β (°)	90
γ (°)	90

Similar procedures were followed to those when using $\text{Fe}(\text{OH})_2$, to test the potentials by comparing their results to experimental data and the results of DFT calculations. The experimentally determined cell configuration was taken and the METADISE code used to generate DFT input files for use in CASTEP. After determining the PBE_pseudo_D potentials to be the most suitable when testing with $\text{Fe}(\text{OH})_2$ these were the chosen set for use with goethite. These potentials were used with and without a Hubbard d value of 4.4 for comparison; a full DFT geometry optimisation was run using each of these parameter sets, with a 4 4 4 k-point grid and 650eV cut-off energy, and no difference in the results was noted, so the Hubbard value was left unamended moving forward. These results are shown in Table 23.

Table 23: Goethite experimentally determined cell parameters compared to DFT modelling results, for amended and unamended Hubbard d values, using PBE_pseudo_D potentials (experimental: $a \neq b \neq c$ and $\alpha = \beta = \gamma$)

Results from	Cell dimensions (Å)			% difference to experiment			Cell angles (°)			% difference to experiment		
	a	b	c	a	b	c	α	β	γ	α	β	γ
Experiment	4.61	9.96	3.02	-	-	-	90.00	90.00	90.00	-	-	-
Unamended Hubbard d value	4.40	9.53	2.94	-4.23	-4.09	-2.47	90.00	90.00	89.99	0.00	0.00	-0.01
Hubbard d value 4.4	4.40	9.53	2.94	-4.23	-4.09	-2.47	90.00	90.00	89.99	0.00	0.00	-0.01

Convergence testing of the PBE_pseudo_D potentials showed that a 4 4 4 k-point grid with a 650eV cut-off energy value was acceptable, as shown in Table 24.

Table 24: Goethite convergence testing of DFT calculations

Final free energy (eV)			
k-point grid	plane-wave cut-off energy (eV)		
	600	650	700
3 3 3	-5898.94	-5898.96	-5898.96
4 4 4	-5899.01	-5899.03	-5899.03
5 5 5	-5899.04	-5899.06	-5899.06

A graphical representation of the convergence is shown in Figure 31.

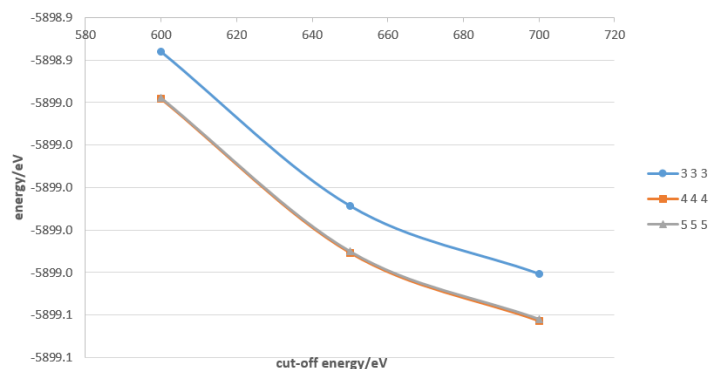


Figure 31: Graphical representation of convergence testing for the bulk structure of goethite

As with $\text{Fe}(\text{OH})_2$, the experimentally determined bulk structure was optimised in METADISE using the rigid ion CLAYFF potentials^[51] and the modified refitted potentials^[71,70,164] based on the work of Baram and Parker.^[163] The shell model tested for $\text{Fe}(\text{OH})_2$ was not used, having already determined the rigid ion potentials to be suitable for this modelling, and easier for future mixing of potentials. The goethite structure determined by Zepeda-Alarcon *et al*^[171] was used as the starting point for these optimisations for expediency, as the cell input file was available on the International Crystal Structural Database. The potential parameters and ionic charges used for the CLAYFF modelling are those detailed earlier in this chapter in Tables 4 to 6. The rigid ion potentials and charges based on the rigid ion model of Baram and Parker are those detailed in Tables 11 to 13.

The results of these geometry optimisations are shown in Table 25 and include the DFT result for comparison.

Table 25: Goethite experimentally determined cell parameters compared to interatomic potential modelling results (experimental: $a \neq b \neq c$ and $\alpha = \beta = \gamma$)

Results from	Cell dimensions (Å)			% difference to experiment			Cell angles (°)			% difference to experiment		
	a	b	c	a	b	c	α	β	γ	α	β	γ
Experiment	4.60	9.94	3.01	-	-	-	90.00	90.00	90.00	-	-	-
CLAYFF rigid ion	4.56	9.84	3.02	-0.73	-1.04	0.22	90.00	90.00	90.00	0.00	0.00	0.00
Rigid ion	4.71	9.87	3.18	2.53	-0.75	5.63	90.00	90.00	90.00	0.00	0.00	0.00
PBE_pseudo_D	4.40	9.53	2.94	-4.30	-4.14	-2.43	90.00	90.00	89.99	0.00	0.00	-0.01

The CLAYFF potential parameters tested were able to adequately reproduce reported structures. The a and b parameters were not quite as accurately reproduced as the c parameter but they were within acceptable limits for this work. The rigid ion model based on that of Baram and Parker was slightly worse, with the c parameter, for example, being over 5% different from experimental observations. The DFT modelling using the PBE_pseudo_D potential set was unable to produce a result as accurate as those from the interatomic potential sets; again this could be because of the difficulty DFT faces in having no direct mechanism to account for dispersive van der Waals forces, though that is not the focus of this project. Having established that the CLAYFF potentials were suitable in modelling the bulk structure of goethite they were then used for modelling surfaces of goethite.

4.4 Goethite Surfaces

The Miller index surfaces investigated were the (0 0 1), (0 1 0), (0 1 1), (1 1 0), (1 1 1), (1 0 0) and (1 0 1). These were the same surfaces investigated for Fe(OH)₂, with the addition of the (1 0 0) and (1 0 1) surfaces; these two addi-

tional surfaces were modelled because the goethite cell structure is $a \neq b \neq c$ whereas $\text{Fe}(\text{OH})_2$ is $a = b \neq c$. This meant that in both cases all the unique low index surfaces based on 1 and 0 were investigated. The aforementioned experimentally determined cell of Zepeda-Alarcon *et al*, relaxed using DFT, was taken as the starting structure. The surfaces were generated from the DFT relaxed cell using METADISE. Once generated, METADISE was used to prepare DFT inputs so that slabs terminating in each surface type could be modelled and investigated. DFT single point calculations were run and the vacuum gap above each surface varied for convergence testing. A slab of 20 unit cells thickness was taken for each surface and the vacuum gap varied, starting from 20Å and increased in 5Å increments until convergence was achieved. The results for total energy (corrected for finite basis set) were compared to test for convergence and are shown in Table 26.

Table 26: Vacuum gap convergence testing for the low index Miller surfaces of goethite

Surface	Vacuum gap (Å)		
	20	25	30
(0 0 1)	35384.22	35384.84	35384.84
(0 1 0)	11794.83	11794.75	11794.75
(0 1 1)	35376.74	35376.59	35376.60
(1 1 0)	23590.66	23590.59	23590.60
(1 1 1)	41276.88	41276.65	41276.66
(1 0 0)	29488.55	29488.32	29488.32
(1 0 1)	47182.71	47182.63	47182.63

Convergence for each surface, within one hundredth of an electron volt, was observed for each of the surfaces at a vacuum gap of 25Å. The thickness of region 1, of the two region system, was optimised using the same method described for Fe(OH)₂. The region values were different than those for Fe(OH)₂ due to the orthorhombic structure of goethite, where $a \neq b \neq c$, meaning that the unit cell thickness for goethite differs greatly depending upon the orientation of the cell. Once the region 1 values were converged to a minimum value the surface energy trends could be compared. As previously, the trend is more important than the absolute values as this can be used to predict relative stability of the different surfaces. The results from this DFT convergence testing for the thickness of region 1, for each surface,

are shown in Tables 27 to 33.

Table 27: Region 1 DFT thickness convergence testing for the (0 0 1) Miller surface of goethite

(0 0 1) Miller surface	
Thickness of Region 1 (unit cells)	Energy difference between surface and bulk (J/m ²)
5	2.69
6	2.69
7	2.69
8	2.69
Converged value for Region 1 thickness (unit cells)	5

Table 28: Region 1 DFT thickness convergence testing for the (0 1 0) Miller surface of goethite

(0 1 0) Miller surface	
Thickness of Region 1 (unit cells)	Energy difference between surface and bulk (J/m ²)
2	2.82
3	2.81
4	2.82
Converged value for Region 1 thickness (unit cells)	2

Table 29: Region 1 DFT thickness convergence testing for the (0 1 1) Miller surface of goethite

(0 1 1) Miller surface	
Thickness of Region 1 (unit cells)	Energy difference between surface and bulk (J/m ²)
5	4.47
6	6.00
7	4.47
8	4.47
Converged value for Region 1 thickness (unit cells)	5

Table 30: Region 1 DFT thickness convergence testing for the (1 1 0) Miller surface of goethite

(1 1 0) Miller surface	
Thickness of Region 1 (unit cells)	Energy difference between surface and bulk (J/m ²)
3	2.06
4	2.06
5	2.06
6	2.06
Converged value for Region 1 thickness (unit cells)	3

Table 31: Region 1 DFT thickness convergence testing for the (1 1 1) Miller surface of goethite

(1 1 1) Miller surface	
Thickness of Region 1 (unit cells)	Energy difference between surface and bulk (J/m ²)
6	3.53
7	4.78
8	3.53
9	3.53
Converged value for Region 1 thickness (unit cells)	6

Table 32: Region 1 DFT thickness convergence testing for the (1 0 0) Miller surface of goethite

(1 0 0) Miller surface	
Thickness of Region 1 (unit cells)	Energy difference between surface and bulk (J/m ²)
4	3.69
5	3.68
6	3.69
Converged value for Region 1 thickness (unit cells)	4

Table 33: Region 1 DFT thickness convergence testing for the (1 0 1) Miller surface of goethite

(1 0 1) Miller surface	
Thickness of Region 1 (unit cells)	Energy difference between surface and bulk (J/m ²)
7	2.86
8	2.86
9	2.86
Converged value for Region 1 thickness (unit cells)	7

Using the region 1 values from the DFT convergence testing, METADISE was used to relax each of the Miller surfaces to their minimum energy state. Having previously established the suitability of the CLAYFF rigid ion potential set these were the only set used; the energy trends for the different surfaces were then compared. These energy trends are shown in Table 34.

Table 34: Surface energy trend comparison for the low index Miller surfaces of goethite. Figures in square brackets represent the lowest to highest energy trends within each set of results

Energy difference between surface and bulk (J/m ²)		
Parameter set		
Miller surface	CLAYFF rigid ion	DFT PBE_pseudo_D
(0 0 1)	1.09 [3]	2.69 [2]
(0 1 0)	0.67 [1]	2.82 [3]
(0 1 1)	1.52 [6]	4.47 [7]
(1 1 0)	1.18 [4]	2.06 [1]
(1 1 1)	1.39 [5]	3.53 [5]
(1 0 0)	1.79 [7]	3.69 [6]
(1 0 1)	0.85 [2]	2.86 [4]

Similarly to the Fe(OH)₂ results, the numerical values are less important than in noting their trends, with a lower value indicating a likely more stable surface in relative terms. Whilst there is a difference in energy values between DFT and CLAYFF potential results, (the DFT energy values are around twice the CLAYFF values), this is not key in this investigation of energy trends; in fact a difference in magnitude would be expected when taking into account the difficulty DFT has with layered structures and in view of the better agreement with experimental data achieved by interatomic potential modelling when considering relative surface stability. The energy value results in Table 34 were, for each parameter set, divided by the lowest value;

this provides energy ratios rather than values for comparison and is shown in Table 35. Once converted to ratios it can be seen that the energy trends between CLAYFF and DFT results vary in their order but not greatly in their magnitude.

Table 35: Surface energy ratio comparison for the low index Miller surfaces of goethite. Figures in square brackets represent the lowest to highest energy trends within each set of results

Surface energy ratios		
Parameter set		
Miller surface	CLAYFF rigid ion	DFT PBE_pseudo-D
(0 0 1)	1.63 [3]	1.31 [2]
(0 1 0)	1.00 [1]	1.37 [3]
(0 1 1)	2.27 [6]	2.17 [7]
(1 1 0)	1.76 [4]	1.00 [1]
(1 1 1)	2.07 [5]	1.71 [5]
(1 0 0)	2.67 [7]	1.79 [6]
(1 0 1)	1.27 [2]	1.39 [4]

The CLAYFF potential sets showed the (0 1 0) to be the most stable surface, followed by the (1 0 1). The (0 0 1) and (1 1 0) surfaces appeared next most stable, quite close to each other in relative terms. Next in order were the (1 1 1) and (0 1 1) with the (1 0 0) surface appearing the least stable of those investigated. The results from DFT suggested the (1 1 0) surface to be the most stable, then the (0 0 1), (0 1 0) and (1 0 1) all relatively

close to each other. Following this the (1 1 1) and (1 0 0) surfaces were quite close to each other and finally the (0 1 1) appeared the least stable. The (0 0 1) surfaces of goethite produced from the CLAYFF potentials and from DFT are shown as examples in figures 32 and 33 respectively; the respective spacing between the Fe atoms of 3.46 Å and 3.11 Å replicate the trend from the Fe(OH)₂ surfaces, where the DFT results produced a relaxed structure with the Fe atoms slightly closer together than the CLAYFF potential results.

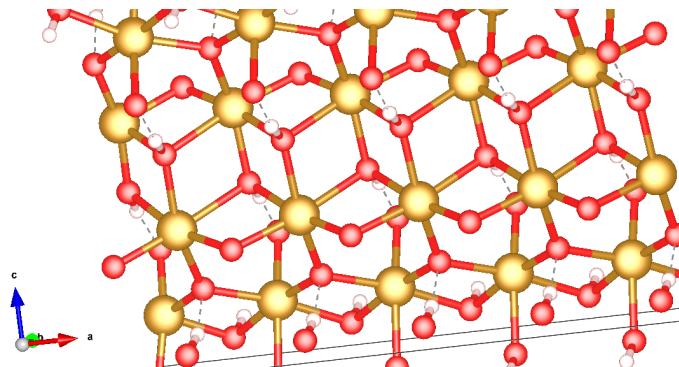


Figure 32: Goethite (0 0 1) surface, perpendicular to lattice vector a , generated from CLAYFF potentials. The spacing between the Fe atoms in adjacent layers is 3.46 Å

As with results for Fe(OH)₂ surfaces, experimental observations support the results of the CLAYFF modelling in determining the most stable surface of goethite, which is shown to be the (0 1 0) surface^[172,173]. There are alternative DFT studies of goethite surfaces, though none addressing the full range of surfaces undertaken in this work and none showing comparative energies to determine the order of likely surface stabilities; Martin *et al* studied surfaces of hematite, magnetite and the (0 1 0) surface of goethite^[174] and Kubicki *et al* note that the (0 1 0) surface is one of the most stable surfaces of goethite^[175]. Zhou *et al* investigated the energy of water molecules on the

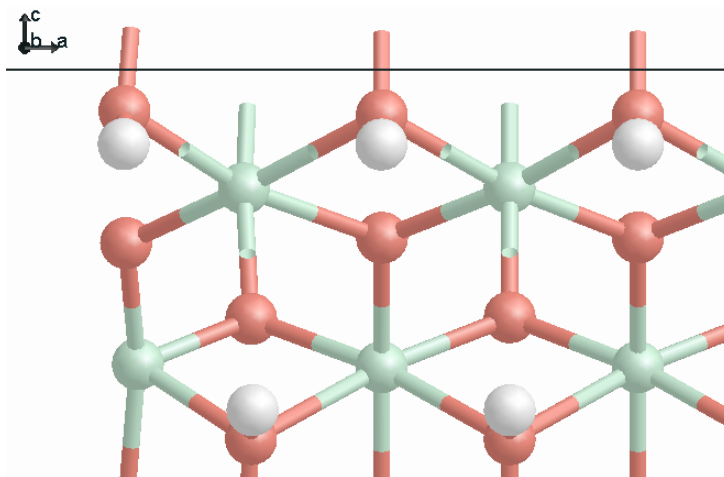


Figure 33: Goethite (0 0 1), perpendicular to lattice vector a , surface generated from DFT. The spacing between the Fe atoms in adjacent layers is 3.11 Å

(0 1 0) surface of goethite using DFT calculations, though they quote water molecule energy and do not give energy values for the goethite surface^[176].

Whilst there are differences in the two sets of results in terms of absolute relative stabilities it can be concluded that surfaces most likely to occur naturally could be (0 1 0), (1 0 1), (0 0 1) and (1 1 0), which are the four most stable surfaces investigated using interatomic potentials or DFT calculations. Surfaces which appear less likely to occur naturally would include (1 0 0), (0 1 1) and (1 1 1); in both the case of DFT and interatomic potential investigations these were the three least stable low index surfaces.

4.5 Conclusions

There is a need for transferable reliable potentials when modelling large systems where DFT cannot be used because of the system size. Similarly to $\text{Fe}(\text{OH})_2$, the results for the modelling of goethite demonstrate that inter-

atomic potentials can be used successfully to model the bulk and the low index Miller surfaces of goethite. These potentials are from existing potential sets which removes the need for expensive fitting procedures. Comparison of results has been made to DFT calculations and empirically obtained data; the potential sets have shown good agreement with these results and demonstrated their interchangeability for use in modelling larger systems without the need for fitting procedures. As was the case for $\text{Fe}(\text{OH})_2$, the interatomic potentials achieve a closer match to experimental data than DFT modelling can produce, for the bulk structure of goethite. Taken in combination with the results from modelling of $\text{Fe}(\text{OH})_2$, the modelling of the bulk and of the low index Miller surfaces of goethite adequately demonstrates that the CLAYFF interatomic potentials are suitable for mixing and use in the modelling and investigation of green rust.

Having established suitable potentials for later use in the bulk modelling of the layered elements of green rust, the next stage was to develop suitable potentials for modelling uranyl compounds which may be formed within the interlayers of green rust. This work is detailed in the following chapter.

5 Uranyl Minerals

The section of the project discussed in the first section of this chapter involves the development of an effective set of interatomic potentials for a range of previously observed uranyl minerals, formed from the uranyl ion UO_2^{2+} and various counterions, namely Cl_2^{2-} , CO_3^{2-} , FeO_2^{2-} , $(\text{OH})_2^{2-}$ and SO_4^{2-} , which are the main components of green rust. The second part of this chapter investigates the uranyl ion UO_2^{2+} in an aqueous environment and the coordination of water molecules.

Fitting any parameterised model to experimental data is by its nature subjective and there is no single method which can be applied to all situations. When considering ionic systems, the method developed by Gale and implemented in the GULP code is widely used^[177]. However, Read *et al* note that that the method does not guarantee a global minimum and the results can be sensitive to the initial configuration provided; they instead favour an approach based on scanning a range of possible parameters and observing the discrepancy between predicted and observed structural properties^[178]. Molecular systems also require the development of intramolecular terms and are therefore by their nature more complex. Traditionally, libraries of potentials have been developed in tandem with simulation software or as a dedicated project and not by individual users, for example in the Amber^[179,180] and CHARMM^[181] molecular dynamics codes.

The need to mix molecular and ionic potential parameters creates another level of subjectivity. One approach is to use an average potential based on mixing rules^[182]. However, such an approach is known to fail when the

potential forms of the two models differ significantly. An alternative method which also incorporates an element of fitting has been proposed by Schröder *et al*^[183] and further refined by Freeman *et al*^[184]. The complex nature of the green rust system, combined with the desire to use existing potential models where possible, has meant that in this work a combination of the methods described above have been used; the exact approach is detailed at the appropriate stages of the discussion in this chapter.

5.1 Methodology

Details of uranyl compounds were taken from the Inorganic Crystal Structural Database (ICSD)^[185] for each of those being investigated. It should be noted that not all of these compounds exist as minerals in the field; some have been synthesised as crystals in the laboratory purely for characterisation and so no great description can be given.

UO₂Cl₂ (uranyl chloride) is bright yellow in colour. It is unstable and decomposes under exposure to light^[186]. It forms highly soluble (in alcohols, ethers and water) crystals which have the appearance of grains of sand. It has three sources of structural information on the crystal database.

UO₂CO₃ (uranyl carbonate) has two structural sources in the crystal database^[187]. It forms yellow crystals and is a constituent of a number of uranyl mineral species, which include andersonite (Na₂Ca(UO₂)(CO₃) · 6 H₂O) and rutherfordine (UO₂CO₃); the latter is the only known mineral to contain purely uranyl and carbonate.

UO_2FeO_2 has one entry on the crystal database from 1967 and is not widely reported upon^[188]; the work in this paper addresses $\text{U}^{6+}\text{Fe}^{2+}\text{O}_4$ rather than the uranyl ion.

$\text{UO}_2(\text{OH})_2$ (uranyl hydroxide) has had the location of hydrogen atoms in the alpha and beta forms investigated previously by Taylor *et al*^[189]. It can precipitate as a yellowcake at near neutral pH when hydrated. There are eight sources of structural information in the crystal database.

UO_2SO_4 (uranyl sulfate) has one source of structural data in the crystal database. The crystalline form is pale yellow and appears like sand.

Whilst the crystal database contains valuable information there are some structures which have not been validated by replication and some studies are, for example, over fifty years old. Thus to provide additional validation of structural information this project uses DFT, using the computer simulation package CASTEP^[86]; the Perdew-Burke-Ernzerhof (PBE) pseudopotentials^[92] used for the exchange-correlation functions are calculated on the fly in the CASTEP code. The results from the crystal database and the DFT calculations are used to empirically fit, test and validate the potentials used for the MM calculations.

5.1.1 Development of Potentials

It may be possible to specifically refit potentials and try and achieve a better fit to experimental or ab initio results^[190], such as by using the GULP^[132] computer code; GULP can use the Broyden-Fletcher-Goldfarb-Shanno (BFGS) algorithm, which is a hill-climbing optimisation technique. It produces an arbitrary solution to the problem then iteratively attempts

to find better solutions by making incremental changes; the Hessian matrix is approximated then gradually improved using approximate gradient evaluations of a function. Alternatively, GULP may fit multiple structures concurrently or use gas-phase cluster information; it can combine free-energy minimisation with empirical fitting based on displacements rather than gradients. More recently, genetic algorithms have been utilised for optimisation problems. These use an iterative process where a population of randomly generated solutions (a generation) is evaluated; the better suited individuals from the populations are selected and may be combined or mutated to form the next generation of solutions. This process continues until the best solution is found.

However the purpose of this work is to use a method which can produce reliable potentials in general cases, whilst at the same time being transparent and less of a “black box” type of potential generation.

The use of existing potentials for the uranyl compounds is desirable where possible. Where reliable potentials are not available they should be derived by a method which is standardised, as far as possible. The algorithm used is similar to that used by Freeman, Harding, Cooke *et al* for deriving CaCO₃-organic interactions from existing potential sets^[184]; the method used is summarised below:

- (1) Existing Lennard-Jones potentials were taken from the literature and used to run a MM structural optimisation in the GULP computer simulation package. The results were compared to the structure from the ICSD and the results from the DFT calculations.

- (2) If potentials in the literature were only available as Buckingham po-

tentials these were recast as Lennard-Jones potentials in the first instance and a structural optimisation and results comparison run as above. This is to try and standardise the potential type for easier mixing of potentials.

(3) Where potentials were not available these were created from existing Lennard-Jones potentials using the standard Lorentz-Berthelot mixing rules. This method was also used to mix potentials that were recast as Lennard-Jones from Buckingham potentials.

(4) If the results from existing or recast Lennard-Jones potentials were outside of acceptable values, the ϵ and R_0 parameters were varied systematically about the literature value (or value produced from mixing) to try and attain a better fit.

(5) If none of the above, using solely Lennard-Jones potentials, produced acceptable results then Buckingham potentials (where available) were incorporated into the input data.

(6) Mixing of Buckingham potentials, which is a more complex procedure than mixing of Lennard-Jones potentials, was undertaken where necessary to try and refine results further and achieve values within acceptable limits.

To demonstrate the methodology an example of potential development will be used, namely uranyl chloride (UO_2Cl_2).

5.1.2 Example: Uranyl Chloride

The unit cell of uranyl chloride, as defined by Taylor and Wilson^[191] is shown in Figure 34

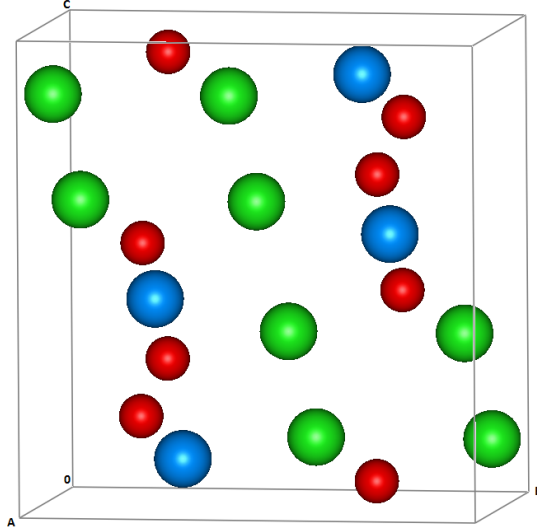


Figure 34: Uranyl chloride, UO_2Cl_2 , $a = 5.725\text{\AA}$, $b = 8.409\text{\AA}$, $c = 8.720\text{\AA}$
 $\alpha = \beta = \gamma = 90^\circ$

Key: uranium, blue; oxygen, red; chlorine, green.

The potential used for the UO_2^{2+} was one already tested and validated by Guilbaud and Wipff^[192]. The initial Cl^- potential used was an aqueous chloride potential used by Cygan et al^[51] when developing the CLAYFF general force field. These parameters are shown in Table 36

Table 36: Nonbond Parameters for the CLAYFF Force Field

species	charge (e)	ϵ (eV)	R_0 (\AA)
aqueous chloride ion	-1.0	0.00434	4.9388

A 12-6 LJ potential was used for the GULP calculations using the input form shown in Equation 102:

$$E_{LJ} = \frac{A}{r^{12}} - \frac{B}{r^6} \quad (102)$$

The values for the A and B parameters are shown in Table 37:

Table 37: Lennard-Jones 12-6 parameters, with CLAYFF chloride potential

	A (eV Å ¹²)	B (eV Å ⁶)
U-U	5999.46965	11.17488
U-O	13420.70013	18.99050
O-O	29307.47496	31.88601
Cl-Cl	914001.69930	125.96455

These potentials were mixed using the Lorentz-Berthelot standard mixing rules to provide interatomic potentials, i.e.

$$\epsilon = \sqrt{\epsilon(1)\epsilon(2)} \quad (103)$$

and

$$R_0 = \frac{R_0(1) + R_0(2)}{2} \quad (104)$$

The MM structural optimisation using these parameters resulted in a cell with dimensional errors in the region of 40% in the c direction, thus an alternative potential was tested. The Buckingham potential used by Spagnoli *et al*^[71], shown in Table 38, was recast as a Lennard-Jones potential to allow mixing using the Lorentz-Berthelot rules.

Table 38: Buckingham Potentials - Spagnoli *et al*

ion pair	A_{ij} (eV)	ρ_{ij} (Å)	C_{ij} (eV Å ⁶)
Cl-Cl	1227.200	0.3214	29.06000

The recasting was done by plotting the Buckingham potential to determine the minimum value of ϵ and the associated R_0 value, then using these values to plot the Lennard-Jones potential. This allowed checking of the fit of curve for both potentials and determination of the A and B parameters for the Lennard Jones potential. Figure 35 shows that a good fit was achieved for the recast Cl-Cl potential and so the Lennard-Jones parameters were determined for this potential.

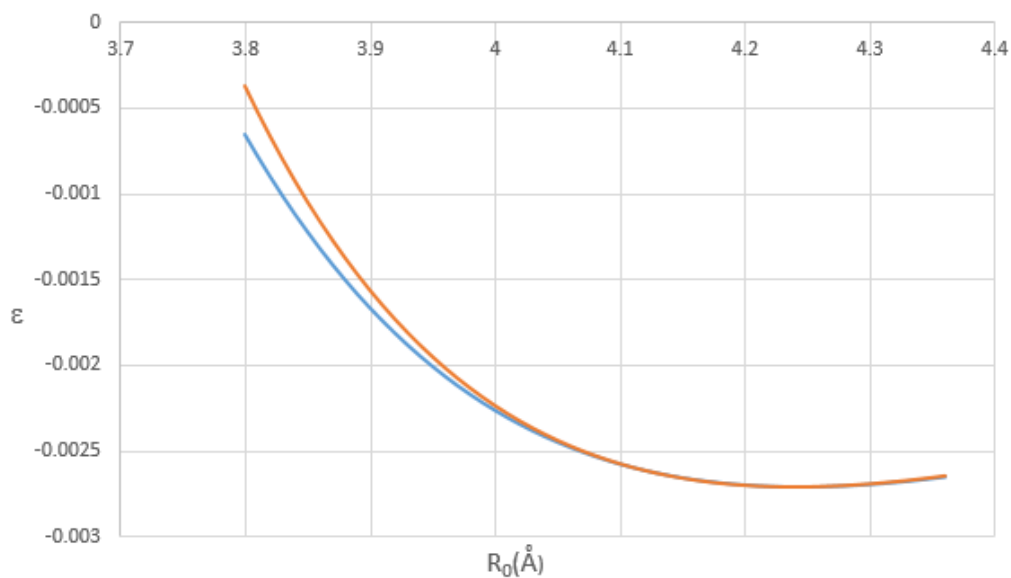


Figure 35: Graph of recast Buckingham potential for Cl-Cl as a Lennard-Jones 12-6 potential

Key: Buckingham potential, blue; Lennard-Jones 12-6 potential, orange.

The revised Lennard-Jones parameters are shown in Table 39:

Table 39: Lennard-Jones 12-6 parameters, revised with chloride potentials from Spagnoli *et al*

	A (eV Å ¹²)	B (eV Å ⁶)
U-U	5999.46965	11.17488
U-O	13420.70013	18.99050
O-O	29307.47496	31.88601
Cl-Cl	91583.35321	31.52473

These potentials were again mixed using the Lorentz-Berthelot standard mixing rules to provide interatomic potentials. The results were improved

though the a dimension of the cell still had an error in the region of 18%. A systematic variation of the ϵ and R_0 values around the minimum energy value did not achieve an improved result so Buckingham potentials were tried instead of Lennard-Jones potentials. This necessitated recasting the U-U Lennard-Jones potential as a Buckingham potential, then mixing the UO_2^{2+} and Cl^- Buckingham potentials to produce the interatomic terms.

When recasting the potential it was decided to keep the attractive term value the same in the Buckingham potential (term C) as it was in the Lennard-Jones potential (term B), i.e. $11.17488 \text{ eV } \text{\AA}^6$. This then left two variables, A and ρ to solve. Two points were taken from the Lennard-Jones potential; the first point was $E = 0, r = \sigma$ from the 4ϵ form of the potential, the second point was $E = \epsilon, r = R$ from the nm form of the potential. Using A and B values taken from the Lennard-Jones potential in Table 37, values were calculated for:

$$E = 0 \tag{105}$$

$$R = \left(\frac{A}{B} \right)^{\frac{1}{6}} \tag{106}$$

and for:

$$E = \left(\frac{A}{R^{12}} \right) \quad (107)$$

$$R = \left(\frac{2A}{B} \right)^{\frac{1}{6}} \quad (108)$$

This allowed a pair of simultaneous equations to be solved and determine that $\rho = 0.2507 \text{ \AA}$. This ρ value could then be substituted into either of the equations to determine that $A = 1806.057 \text{ eV}$.

The O-O potentials were retained as their existing Lennard-Jones 12-6 potentials. This meant that the derivation of a U-Cl Buckingham potential was required.

Using the Spagnoli Cl-Cl and Cl-O potentials and the recast U-U potential gave a set of Buckingham potential parameters as shown in Table 40:

Table 40: Buckingham potential parameters

	A (eV)	ρ (\AA)	C (eV \AA^6)
U-U	1806.057	0.2507	11.17488
Cl-Cl	1227.200	0.3214	29.06000
O-Cl	1272.249	0.2352	34.99827

The method of derivation for mixed Buckingham potentials is founded on the soft sphere model presented by Gilbert^[193].

If the final term of Equation 17 is considered, in the Buckingham potential this term is represented as:

$$\Phi(r_{ij}) = A_{ij} \exp\left(\frac{-r_{ij}}{\rho_{ij}}\right) - \frac{C_{ij}}{r_{ij}^6} \quad (109)$$

$\Phi(r_{ij})$ is the short range interaction between the ions, r_{ij} is the ionic separation. A_{ij} , ρ_{ij} and C_{ij} are empirical parameters which are derived to fit each ion pair.

Gilbert demonstrated that the repulsive term of the Buckingham potential, A_{ij} , could be replaced by a distance, R_{ij} , which is the distance between two ions which are acting against repulsive forces only, and are being pushed together by an arbitrary force, f :

$$R_{ij} = \rho_{ij} \ln\left(\frac{A_{ij}}{f\rho_{ij}}\right) \quad (110)$$

Gilbert also used spectroscopic data to show that the hardness parameter, ρ_{ij} , and the soft sphere radii, R_{ij} , obeyed the additivity rules, i.e. $\rho_{ij} = \rho_i + \rho_j$ and $R_{ij} = R_i + R_j$, where $\rho_i = \frac{\rho_{ii}}{2}$ and $R_i = \frac{R_{ii}}{2}$.

Therefore the Born-Mayer repulsive potential, U_{ij} , can be written as:

$$U_{ij}(R) = f(\rho_i + \rho_j) \exp\left(\frac{R_i + R_j}{\rho_i + \rho_j}\right) \exp\left(\frac{-R_{ij}}{\rho_{ij}}\right) \quad (111)$$

Thus determining the ρ value was straightforward:

$$\rho_{U-Cl} = \frac{\rho_{Cl-Cl}}{2} + \frac{\rho_{U-U}}{2} = 0.2861 \text{ \AA}$$

To determine the A value, consideration of the Cl-Cl repulsive interaction in Equation 111 means it can be written as:

$$U_{Cl-Cl}(R) = f(\rho_{Cl} + \rho_{Cl}) \exp\left(\frac{R_{Cl} + R_{Cl}}{\rho_{Cl} + \rho_{Cl}}\right) \exp\left(\frac{-R_{Cl-Cl}}{\rho_{Cl-Cl}}\right) \quad (112)$$

Equation 110 can be rearranged and written as:

$$A_{Cl-Cl} = f\rho_{Cl-Cl} \exp\left(\frac{R_{Cl-Cl}}{\rho_{Cl-Cl}}\right) \quad (113)$$

So:

$$A_{Cl-Cl} = f(0.3214) \exp\left(\frac{R_{Cl}}{0.1607}\right)$$

Taking ln of both sides gives:

$$\ln 1227.200 = \ln f + \ln 0.3214 + \frac{R_{Cl}}{0.1607}$$

Which gives:

$$R_{Cl} = 0.1695408197 - 0.1607 \ln f$$

Following the same procedure for R_U gives:

$$R_U = 0.1402037827 - 0.12535 \ln f$$

Using these values in Equation 110, for the repulsive part of the equation only (*i.e.* not including the final exponential term), produces:

$$A_{U-Cl} = f(0.2861) \exp\left(\frac{0.3097446024 - 0.2861 \ln f}{0.2861}\right) \quad (114)$$

Finally, taking ln of both sides allows evaluation of:

$$A_{U-Cl} = 1440.069148 \text{ eV}$$

Thus the final set of Buckingham potential parameters are shown in Table 41. This method was previously used to derive potentials for FeCl_2 , which are the potentials used in work by Spagnoli *et al*^[71].

Table 41: Buckingham potential parameters

	A (eV)	ρ (Å)	C (eV Å ⁶)
U-U	1806.057	0.2507	11.17488
Cl-Cl	1227.200	0.3214	29.06000
O-Cl	1272.249	0.2352	34.99827
U-Cl	1440.069	0.2861	11.17488

The C parameter for the U-Cl potential was determined simply by fixing the value at that of the U-U Lennard-Jones 12-6 potential, so can be varied when testing the potential. It is in fact often taken to be 0 in value as the attractive forces are dominated by the Coulombic term of the Born-Mayer potential.

The methodology described above was used, in full or in part as appropriate, to produce or refine potential sets for each of the minerals under investigation. The testing of these potential sets is discussed in the following results section.

5.2 Results

5.2.1 Uranyl Chloride

The experimentally determined structure of Taylor and Wilson^[191] (shown in Figure 34) was used as the starting point for this work. Reference was also made to DFT calculations using the CASTEP code^[86] using the generalised gradient approximation (GGA) basis sets; a 600 eV cut-off was used with a k-point grid of 4 4 4.

The methodology and sequence of potential trials for uranyl chloride is detailed in section 5.1.2. The partial charge, q_u , on the chloride ion was -1.0 eV which is shown in Table 42 along with the other partial charges used.

Table 42: Partial charges (q_u) on ions used in the testing and development of interatomic potentials

Species	
Ion	Charge (e)
Uranium (U)	3.2500
Uranyl Oxygen (Ou)	-0.6250
Chlorine (Cl)	-1.0000

The ClayFF potential for the chloride ion is for the aqueous form; as the results using the ClayFF potentials^[51] were around 40% larger than the experimental unit cell size in the c dimension the potentials used by Spagnoli et al^[71] were tested. These provided a better match to experimental cell parameters, improving the c dimension by around 33%. The results using these potentials and the results of the DFT calculations are shown in Table

43.

Table 43: UO_2Cl_2 simulation results comparing experimental data with results generated from CASTEP (DFT) and GULP (using interatomic potentials)

UO_2Cl_2	Experimental data	DFT output	% difference	MM output (Spagnoli et al pots)	% difference
a (Å)	5.725	5.759	0.590	4.692	18.047
b (Å)	8.409	8.350	0.705	8.009	4.756
c (Å)	8.720	8.709	0.125	9.327	6.965
alpha (°)	90	90	0.000	90	0.000
beta (°)	90	90	0.000	90.125	0.139
gamma (°)	90	90	0.000	90	0.000

The recasting of uranyl Lennard-Jones potentials as Buckingham potentials and mixing of these with the chloride Buckingham potentials, as detailed in 5.1.2, did not have a beneficial effect on cell sizes from those obtained with the Spagnoli et al potentials; thus the results in Table 43 are currently the best obtained. Further refinement to obtain values closer to the experimental cell sizes are desirable, particularly the a dimension of the cell. The work of Spagnoli et al from which the chloride potentials were taken does not in fact use a rigid ion model, such as this work attempts to produce, instead it uses a polarisable shell model; they derive potentials by fitting to reproduce the structure and energetics of chloride-water clusters from ab initio calculations. They do not directly model uranyl chloride but model sodium chloride in aqueous solution and its interaction with various solid surfaces. In the absence of rigid ion models of uranyl chloride in the literature it is better to compare results with empirical data and DFT calculations.

5.2.2 Uranyl Carbonate

The experimentally determined unit cell of uranyl carbonate is shown in Figure 36.

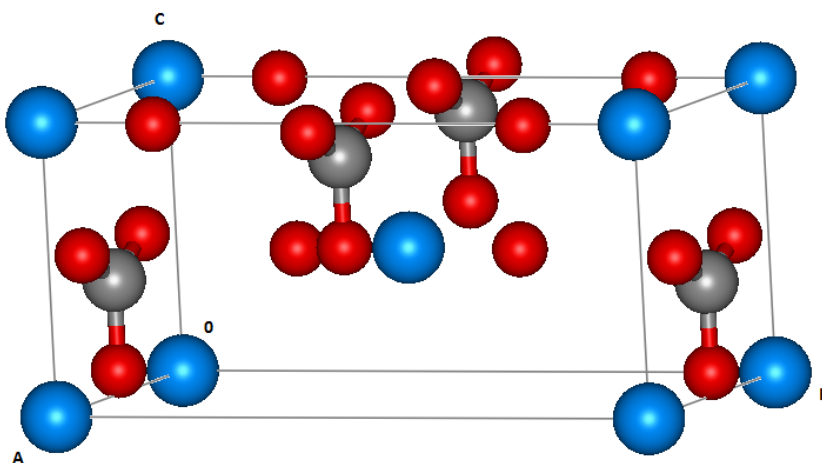


Figure 36: Uranyl carbonate, UO_2CO_3 , $a = 4.840\text{\AA}$, $b = 9.273\text{\AA}$, $c = 4.298\text{\AA}$
 $\alpha = \beta = \gamma = 90^\circ$

Key: uranium, blue; oxygen, red; carbon, grey.

Similarly to the chloride, an experimental structure was used as a starting point and reference for the uranyl carbonate structure, namely that of Finch

et al.^[187] The DFT calculations run in the CASTEP code used a 600 eV cut-off with a 3 3 3 k-point grid.

The potential parameters and ionic charges used were those detailed by Kerisit and Liu^[194], using Lennard-Jones potentials for all but the O_c-O_c interactions, which are Buckingham potentials. These are shown in Tables 44 to 46.

Table 44: Partial charges (q_u) on ions used in the testing and development of interatomic potentials

Species	
Ion	Charge (e)
Uranium (U)	3.2500
Uranyl Oxygen (Ou)	-0.6250
Carbon (C)	1.1350
Carbonate Oxygen (Oc)	-1.0450

Table 45: Lennard-Jones potentials for UO_2CO_3

Lennard-Jones potentials $A_{ij}r_{ij}^{-12} - B_{ij}r_{ij}^{-6}$			
Ion pair (ij)	A_{ij} (eV \AA^{12})	B_{ij} (eV \AA^6)	Reference
U-U	5999.46965	11.17488	[194]
U-Ou	13420.70013	18.99050	[194]
U-Oc	35000.00000	22.00000	[194]
Ou-Ou	29307.47496	31.88601	[194]
Ou-Oc	27290.95482	27.12257	[194]

Table 46: Buckingham potentials for UO_2CO_3

Buckingham Potentials $A_{ij} \exp(-r_{ij}/\rho_{ij}) - (C_{ij}/r_{ij}^6)$				
Ion pair (ij)	A_{ij} (eV)	ρ_{ij} (Å)	C_{ij} (eV Å ⁶)	Reference
Oc-Oc	16372.0	0.2130	3.47	[194]

The Morse, harmonic, three-body and four-body potentials are shown in Tables 47 to 50; these are also taken from the same work of Kerisit and Liu.

Table 47: Morse potentials for UO_2CO_3

Morse potentials $D_{ij}[\{1 - \exp(-\alpha_{ij}(r_{ij} - r_0))\}^2 - 1]$					
Ion pair (ij)	D_{ij} (eV)	α_{ij} (Å ⁻¹)	r_0 (Å)	Coul.Sub (%)	Reference
C-Oc	4.71	3.80	1.18	0.00	[194]

Table 48: Harmonic potentials for UO_2CO_3

Harmonic potentials $k_{ij}/2(r_{ij} - r_0)^2$			
Species (ij)	k_{ij} (eV Å ⁻²)	r_0 (Å)	Reference
U-Ou	43.36	1.80	[194]

Table 49: Three-body potentials for UO_2CO_3

Three-body potentials $k_{ijk}/2(\theta_{ijk} - \theta_0)^2$			
Species (ijk)	k_{ijk} (eV rad ⁻²)	θ_0 (deg)	Reference
Ou-U-Ou	13.01	180.00	[194]
Oc-C-Oc	1.69	120.00	[194]

Table 50: Four-body potentials for UO_2CO_3

Four-body potentials $k_{ijkl}[1 + \cos(2\theta_{ijkl} - \theta_0)]$			
Species (ijkl)	k_{ijkl} (eV rad ⁻²)	θ_0 (deg)	Reference
C-Oc-Oc-Oc	0.1129	180.00	[194]

Initial results from the MM calculations were promising with all unit cell angles at 90° and both the a and c dimensions reproduced to within 1% of experimental results. However the b value was overestimated by around 12%.

The U– O_c potential value in the Kerisit and Liu paper does not appear to be derived from any standard mixing rules and its derivation is not given. Systematic variation of the ϵ and R_0 values did not yield improvement in the b value. Thus the O_c – O_c potential was recast as a Lennard-Jones potential and similar variation of the ϵ and R_0 values carried out. Improvement in any one cell dimension was always to the detriment of another and so no improvement could be made. To test a U– O_c Buckingham potential, the U–U Lennard-Jones potential was recast as a Buckingham potential then mixed with the O_c potential using the worked example methodology. Using

the GULP MM code with these potentials produced a , b and c values which were overestimated by between 10% and 12%. Thus the initial potentials of Kerisit and Liu produce the closest fit to experimental results obtained; the difficulty with these potentials is the use of non-standard mixing rules or potentials with no given derivation, meaning their incorporation into larger mixed systems at a later time could be difficult.

Table 51 summarises the experimental, DFT and GULP MD results.

Table 51: UO_2CO_3 simulation results comparing experimental data with results generated from CASTEP (DFT) and GULP (using interatomic potentials)

UO_2CO_3	Experimental data	DFT output	% difference	MM output (Kerisit-Liu pots)	% difference
a (Å)	4.840	4.857	0.351	4.788	1.081
b (Å)	9.273	9.026	2.663	10.459	12.785
c (Å)	4.298	4.288	0.236	4.340	0.976
alpha (°)	90	90	0.000	90	0.000
beta (°)	90	90	0.000	90	0.000
gamma (°)	90	90	0.000	90	0.000

Kerisit and Liu do use a rigid ion model for uranyl carbonate, though in this and their earlier supporting works they use uranyl and carbonate potentials from different sources and do not test the structure of uranyl carbonate before incorporating these potentials into a wider aqueous system; thus there are no computational structures to compare to other than those generated in this study using DFT techniques.

5.2.3 Uranyl Iron Oxide

The experimental structure, shown in Figure 37, determined in 1967 by Bacmann and Bertaut^[188] was used as a starting point and reference for simulations. The DFT reference calculations were run in the CASTEP code with a cut-off of 650 eV and a k-point grid of 3 3 3.

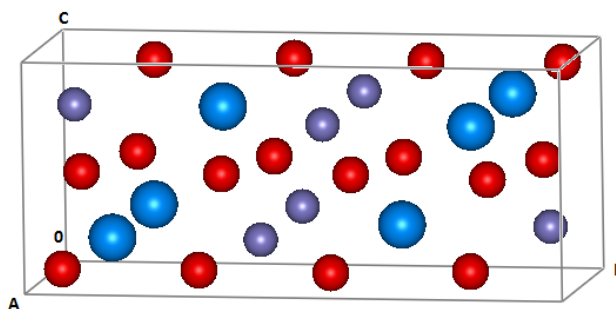


Figure 37: Uranyl iron oxide, UO_2FeO_2 , $a = 4.888\text{\AA}$, $b = 11.937\text{\AA}$, $c = 5.110\text{\AA}$ $\alpha = \beta = \gamma = 90^\circ$

Key: uranium, blue; oxygen, red; iron, purple.

Whilst this project aims to use Lennard-Jones potentials where possible, for simple mixing of potentials using the Lorentz-Berthelot rules, the uranyl iron oxide at this point has only been simulated using Buckingham potentials. These are potentials from the work of Kerisit et al^[195] and are shown in Table 53. The partial charges are shown in Table 52; these charges are different to those for the uranyl uranium and oxygen ions in the other simulations so do not suit combination into a wider system with these other simulation values.

Table 52: Partial charges (q_u) on ions used in the testing and development of interatomic potentials

Species	
Ion	Charge (e)
Uranium (U) core	-1.3500
Uranium (U) shell	7.3500
Uranyl Oxygen (Ou) core	0.2100
Uranyl Oxygen (Ou) shell	-2.2100
Iron (II) (Fe) core	2.0000

Table 53: Buckingham potentials for UO_2FeO_2

Buckingham Potentials $A_{ij} \exp(-r_{ij}/\rho_{ij}) - (C_{ij}/r_{ij}^6)$				
Ion pair (ij)	A_{ij} (eV)	ρ_{ij} (Å)	C_{ij} (eV Å ⁶)	Reference
O shell - O shell	22764.300	0.14900	27.88	[188]
U shell - O shell	3428.870	0.33415	43.89	[188]
Fe core - O shell	816.105	0.32990	0.00	[188]

The results from the MM calculations show a better fit with experimental values than the DFT calculations, with both a and b dimensions being within 0.1% and the c dimension being only 2.2% underestimated. No further refinement of potentials was attempted due to the very close fit of values and because the potentials and ionic partial charges do not particularly suit development into the broader system with the other compounds simulated. Table 54 summarises the simulation results.

Table 54: UO_2FeO_2 simulation results comparing experimental data with results generated from CASTEP (DFT) and GULP (using interatomic potentials)

UO_2FeO_2	Experimental data	DFT output	% difference	MM output (Kerisit-Felmy-Ilton pots)	% difference
a (Å)	4.888	4.881	0.149	4.883	0.094
b (Å)	11.937	11.264	5.636	11.928	0.076
c (Å)	5.110	5.064	0.902	4.996	2.240
alpha (°)	90	90	0.000	90	0.000
beta (°)	90	90	0.000	89.990	0.011
gamma (°)	90	90	0.000	90	0.000

Kerisit et al compare their results only to the empirical results of Bacmann and Bertaut as there are no available computational studies to compare to; they do not test and compare to any DFT calculation results. Their only stated comparison for uranyl iron oxide with U(VI) / Fe(II) is that their result compared poorly with experiment, with the supporting information showing that the a , b and c parameters varied by +3.5%, -10.2% and -5.3% respectively.

5.2.4 Uranyl Hydroxide

Figure 38 shows the unit cell of uranyl hydroxide as determined by Taylor and Hurst^[189].

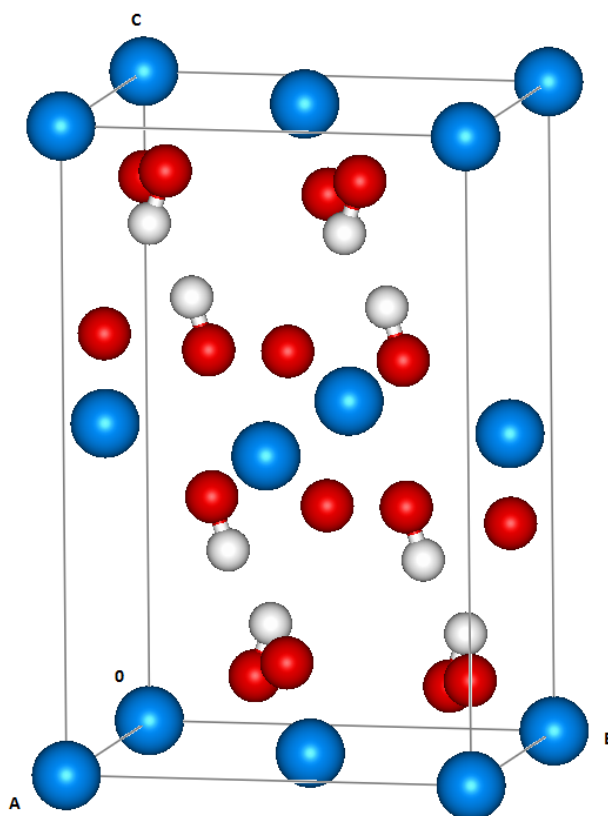


Figure 38: Uranyl hydroxide, $\text{UO}_2(\text{OH})_2$, $a = 5.644\text{\AA}$, $b = 6.287\text{\AA}$, $c = 9.937\text{\AA}$ $\alpha = \beta = \gamma = 90^\circ$

Key: uranium, blue; oxygen, red; hydrogen, white.

The experimental structure of Taylor and Hurst^[189] was used as a starting point. The DFT calculations were run in the CASTEP computer code with

a cut-off of 600 eV and a k-point grid of 3 3 3. Table 55 details the partial charges on the ions in the MM simulation. The partial charges for O and H given by Cygan et al gave an overall charge of -0.525e for the hydroxide ion (OH⁻) so these charges were divided by 0.525 to produce an overall charge of -1.0 e.

Table 55: Partial charges (q_u) on ions used in the testing and development of interatomic potentials

Species	
Ion	Charge (e)
Uranium (U)	3.2500
Uranyl Oxygen (Ou)	-0.6250
Hydrogen (H)	0.4000
Hydroxide Oxygen (Oh)	-1.4000

Initial MM calculations were performed using the hydroxide potential of Cygan et al^[51]. The results were poor, for example the a parameter of the unit cell was underestimated by around 46%. An alternative OH⁻ potential was sought and it was decided to try that developed by Baram and Parker^[163], used in other work such as that of de Leeuw and Cooper^[73]. The partial charges in the shell used by Baram and Parker were combined to suit the rigid ion model used in this work. The hydroxide potential was recast from the Buckingham form to the Lennard-Jones form to allow use of the Lorentz-Berthelot mixing rules. A slight improvement in results was observed, but the a , b and c parameters of the cell were still -28.37%, -20.47% and +7.97% away

from experimental values respectively, which was considered unacceptable. Potentials for the O_h -H and H-H interactions were added using values for the water potential in the work of Kerisit and Parker^[196]; this had a detrimental effect on the results. The Lennard-Jones potentials used are given in Table 56.

Table 56: Lennard-Jones potentials for $UO_2(OH)_2$

Lennard-Jones potentials $A_{ij}r_{ij}^{-12} - B_{ij}r_{ij}^{-6}$			
Ion pair (ij)	A_{ij} (eV Å ¹²)	B_{ij} (eV Å ⁶)	Reference
U-U	5999.46965	11.17488	[163]
U-Ou	13420.70013	18.99050	[163]
U-H	745.21960	6.45295	[163]
U-Oh	1493.51526	11.12339	[163]
Ou-Ou	29307.47496	31.88601	[163]
Ou-H	1948.12756	11.85460	[163]
Ou-Oh	3938.45768	20.26157	[163]
H-H	31.79701	2.18393	[163]

The Buckingham potentials of Baram and Parker were then utilised instead of their recast Lennard-Jones version for the hydroxide ion. (It was noted that de Leeuw and Cooper were also unable to obtain a good match to experimental unit cell sizes in their work utilising the Baram and Parker hydroxide potentials^[73], though they were able to reproduce some of the cell dimension ratios to good effect. The Baram and Parker potentials tested are detailed in Tables 57 to 60).

The hydroxide Buckingham potentials of Fleming and Rohl were also considered^[197], though as these would not recast as Lennard-Jones potentials they were not investigated further at this stage.

Table 57: Buckingham potentials for $\text{UO}_2(\text{OH})_2$

Buckingham Potentials $A_{ij} \exp(-r_{ij}/\rho_{ij}) - (C_{ij}/r_{ij}^6)$				
Ion pair (ij)	A_{ij} (eV)	ρ_{ij} (Å)	C_{ij} (eV Å ⁶)	Reference
Oh-Oh	22764.0	0.1490	6.97	[163]
H-Oh	311.97	0.2500	0.00	[163]

Table 58: Morse potentials for $\text{UO}_2(\text{OH})_2$

Morse potentials $D_{ij}[\{1 - \exp(-\alpha_{ij}(r_{ij} - r_0))\}^2 - 1]$					
Ion pair (ij)	D_{ij} (eV)	α_{ij} (Å ⁻¹)	r_0 (Å)	Coul.Sub (%)	Reference
H-Oh	7.0525	3.1749	0.9258	0.00	[163]

Table 59: Harmonic potentials for $\text{UO}_2(\text{OH})_2$

Harmonic potentials $k_{ij}/2(r_{ij} - r_0)^2$			
Species (ij)	k_{ij} (eV Å ⁻²)	r_0 (Å)	Reference
U-Ou	43.36	1.80	[163]

Table 60: Three-body potentials for $\text{UO}_2(\text{OH})_2$

Three-body potentials $k_{ijk}/2(\theta_{ijk} - \theta_0)^2$			
Species (ijk)	k_{ijk} (eV rad ⁻²)	θ_0 (deg)	Reference
Ou-U-Ou	13.01	180.00	[163]

The MM calculations failed to optimise with an energy minimum not being reached; this is reflected in Table 61.

Table 61: $\text{UO}_2(\text{OH})_2$ simulation results comparing experimental data with results generated from CASTEP (DFT) and GULP (using interatomic potentials)

$\text{UO}_2(\text{OH})_2$	Experimental data	DFT output	% difference	MM output (Baram & Parker pots)	% difference
a (Å)	5.644	5.621	0.407	unresolved	0.000
b (Å)	6.287	6.161	2.001	unresolved	0.000
c (Å)	9.937	9.796	1.422	unresolved	0.000
alpha (°)	90	90	0.000	unresolved	0.000
beta (°)	90	90	0.000	unresolved	0.000
gamma (°)	90	90	0.000	unresolved	0.000

5.2.5 Uranyl sulfate

The experimentally determined structure of Brandenburg and Loopstra^[198] as shown in Figure 39 was taken as a starting point. DFT calculations were run in the CASTEP computer code with a cut-off of 600 eV and a k-point grid of 3 3 3. The partial charges on the ions are shown in Table 62. The charges and Lennard-Jones potentials are those of Williams et al^[199], the potentials are detailed in Tables 63 to 65.

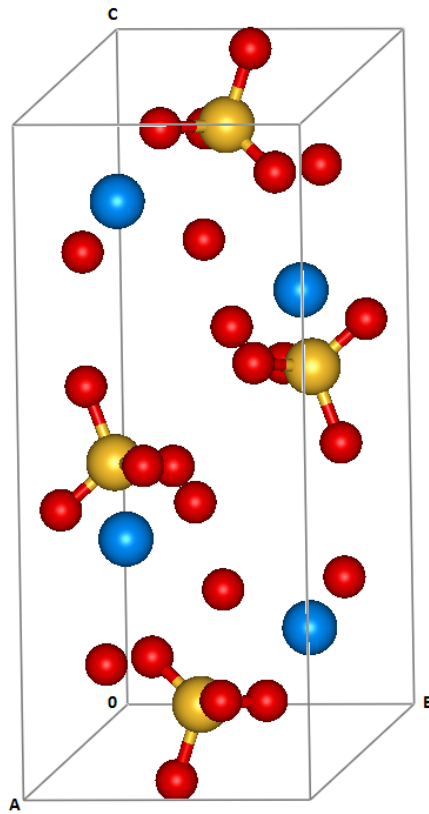


Figure 39: Uranyl sulfate, UO_2SO_4 , $a = 6.760\text{\AA}$, $b = 5.711\text{\AA}$, $c = 12.824\text{\AA}$
 $\alpha = \gamma = 90^\circ$, $\beta = 102.91^\circ$

Key: uranium, blue; oxygen, red; sulfate, yellow.

Table 62: Partial charges (q_u) on ions used in the testing and development of interatomic potentials

Species	
Ion	Charge (e)
Uranium (U)	3.2500
Uranyl Oxygen (Ou)	-0.6250
sulfur (S)	2.3000
sulfate Oxygen (Os)	-1.0750

Table 63: Lennard-Jones potentials for UO_2SO_4

Lennard-Jones potentials $A_{ij}r_{ij}^{-12} - B_{ij}r_{ij}^{-6}$			
Ion pair (ij)	A_{ij} (eV \AA^{12})	B_{ij} (eV \AA^6)	Reference
U-U	5999.46965	11.17488	[199]
U-Ou	13420.70013	18.99050	[199]
U-S	31035.71070	28.88050	[199]
U-Os	15373.18604	19.08056	[199]
Ou-Ou	29307.47496	31.88601	[199]
Ou-S	65459.70305	47.65667	[199]
Ou-Os	33199.97434	31.85959	[199]
S-S	139015.97340	69.45360	[199]
S-Os	72969.31917	47.23536	[199]
Os-Os	37416.43460	31.75140	[199]

Table 64: Harmonic potentials for UO_2SO_4

Harmonic potentials $k_{ij}/2(r_{ij} - r_0)^2$			
Species (ij)	k_{ij} (eV \AA^{-2})	r_0 (\AA)	Reference
U-Ou	43.36	1.80	[199]
S-Os	22.79	1.49	[199]

Table 65: Three-body potentials for UO_2SO_4

Three-body potentials $k_{ijk}/2(\theta_{ijk} - \theta_0)^2$			
Species (ijk)	k_{ijk} (eV rad^{-2})	θ_0 (deg)	Reference
Ou-U-Ou	13.01	180.00	[199]
Os-S-Os	6.07	109.47	[199]

The initial results from the MM simulation gave excellent accord with experimental results, with the a parameter underestimated by 1.2% and the b and c parameters less than 1% different. Unit cell angles were reproduced to less than 0.02% of experimentally determined angles. The results suggest that this sulfate potential will be suitable for incorporation into a larger mixed system without the need for modification. Simulation results are summarised in Table 66.

Table 66: UO_2SO_4 simulation results comparing experimental data with results generated from CASTEP (DFT) and GULP (using interatomic potentials)

UO_2SO_4	Experimental data	DFT output	% difference	MM output (Williams et al pots)	% difference
a (Å)	6.760	6.777	0.245	6.677	1.230
b (Å)	5.711	5.575	2.377	5.743	0.556
c (Å)	12.824	12.909	0.659	12.787	0.290
alpha (°)	90	90	0.000	90	0.000
beta (°)	102.91	103.13	0.214	102.930	0.019
gamma (°)	90	90	0.000	89.999	0.001

The work of Williams *et al* did not model uranyl sulfate but did model the sulfate anion in aqueous solution. Their work used the results of DFT calculations as a reference for testing the potentials, which is the same approach as used in this work. They set bond lengths and angles to match the DFT results and used literature values for the force constants of SO_4^{2-} . The optimised SO_4^{2-} parameters produced by Williams *et al*, and used in this work, are very similar to other classical force fields^[200], thus suggesting the development approach is logical.

5.3 Water and UO_2^{2+}

Molecular dynamics simulations were carried out to investigate the uranyl ion (UO_2^{2+}) and the coordination of water molecules in an aqueous environment. The investigations were undertaken using the DL_POLY Classic MD simulation package^[133]. This was to investigate and refine the potential parameters, particularly the partial charges on the ions in the system. Empirical data has shown there to be five water molecules in the first co-

ordination sphere around the UO_2^{2+} with a U—OW distance of 2.42 Å; this was a study using X-ray diffraction and ^1H NMR to characterise a 1 M aqueous solution of uranyl perchlorate ($\text{UO}_2(\text{ClO}_4)_2 \cdot 7 \text{H}_2\text{O}$)^[201], showing the presence of $[\text{UO}_2(\text{H}_2\text{O})_5]^{2+}$. Rogers *et al* investigated the reactions of $\text{UO}_2(\text{ClO}_4) \cdot n\text{H}_2\text{O}$ with 15-crown-5 and 18-crown-6 ether in acetonitrile; each of the complexes formed were characterised and contained $[\text{UO}_2(\text{H}_2\text{O})_5]^{2+}$, confirming five water molecules in the first hydration shell of the uranyl ion^[202]. In a study of the crystal and molecular structure of uranyl diperchlorate heptahydrate ($\text{UO}_2[\text{ClO}_4]_2 \cdot 7 \text{H}_2\text{O}$), using single-crystal X-ray methods, Alcock *et al* showed the crystal contained $[\text{UO}_2(\text{H}_2\text{O})_5]^{2+}$, $2[\text{ClO}_4]^-$ and $2 \text{H}_2\text{O}$; the U—O(aqua) bond length was 2.45 Å^[203]. All of these studies found the uranyl ion and the five water molecules to be arranged with a pentagonal-bipyramidal geometry *i.e.* with the five water molecules arranged equatorially around the uranyl ion. A molecular dynamical study of the hydrated ion model of $[\text{UO}_2]^{2+}$ in water by Pérez-Conesa *et al* showed five water molecules in the first hydration shell, $[\text{UO}_2(\text{H}_2\text{O})_5]^{2+}$, with an average U—O distance of 2.46 Å; this work also showed the water molecules in an equatorial arrangement around the uranyl ion^[204].

Previously, Guilbaud and Wipff developed a set of potential parameters compatible with the AMBER force field and TIP3P water model, to model $\text{UO}_2^{2+}(\text{aq})$ ^[205,192]. They investigated the effect of varying the charge on the component ions whilst maintaining an overall charge of +2 on the uranyl ion. They found that in order to maintain a coordination number of five water molecules around the central uranium ion, charges smaller than +6 and -2 were required^[205], though they concluded that a charge of +3 on the uranium

ion led to the uranyl oxygen ions being associated with a charge too low (-0.5) when compared to that of the oxygen of the TIP3P water molecules (-0.834)^[66]. In subsequent work, Guilbaud and Wipff produced results working with a charge of +2.5 on the uranium ion, where they accepted the need for the charge on the uranyl oxygen ions to be as low as -0.25, though the parameters quoted in the text of this paper do not match those presented in the tables of the same paper^[192]. These results from Guilbaud and Wipff were able to replicate the five H₂O ligands in the equatorial plane with a U—OW distance of 2.4 Å, in accordance with experimental results. Further investigation using quantum mechanical (QM) calculations has subsequently confirmed this result^[206], although this calculation was performed using a small gas phase complex. It was decided that the uranyl ion parameters from this later work of Guilbaud and Wipff would be taken as a starting point and the partial charges on the ions varied. These parameters, and those for the TIP3P water model, are shown in Tables 67 to 70.

Table 67: Partial charges (q_u) on ions used in molecular dynamics modelling of the uranyl ion in water, using potentials as Guilbaud and Wipff^[192].

Species	
Ion	Charge (e)
Uranyl Uranium (U)	2.5000
Uranyl Oxygen (Ou)	-0.2500
Water Oxygen (Ow)	-0.834
Water Hydrogen (Hw)	0.417

Table 68: Lennard-Jones potentials used in molecular dynamics modelling of the uranyl ion in water, using potentials as Guilbaud and Wipff^[192]

Lennard-Jones potentials $A_{ij}r_{ij}^{-12} - B_{ij}r_{ij}^{-6}$		
Ion pair (ij)	A_{ij} (eV Å ¹²)	B_{ij} (eV Å ⁶)
U-U	1.465064	0.174649
U-Ou	1.972697	0.214274
U-Ow	482.488500	3.362343
Ou-Ou	2.648686	0.262517
Ou-Ow	605.935063	3.984181
Ow-Ow	25246.059000	25.805200

Table 69: Harmonic potentials used in molecular dynamics modelling of the uranyl ion in water, using potentials as Guilbaud and Wipff^[192]

Harmonic potentials $k_{ij}/2(r_{ij} - r_0)^2$		
Species (ij)	k_{ij} (eV Å ⁻²)	r_0 (Å)
U-Uo	21.682127	1.8000
Ow-Hw	23.990700	0.9572

Table 70: Three-body potentials used in molecular dynamics modelling of the uranyl ion in water, using potentials as Guilbaud and Wipff^[192]

Three-body potentials $k_{ijk}/2(\theta_{ijk} - \theta_0)^2$		
Species (ijk)	k_{ijk} (eV rad ⁻²)	θ_0 (deg)
Ou-U-Ou	6.504638	180.00
Hw-Ow-Hw	4.338300	104.52

Firstly the TIP3P water model, using a box of 390 water molecules, was optimised using DL_POLY at temperatures of 300K, 350K, 400K and 450K. The NPT ensemble with a Hoover thermostat was used, with a timestep of 0.001 picoseconds. The 300K result is shown as an example in figure 40.

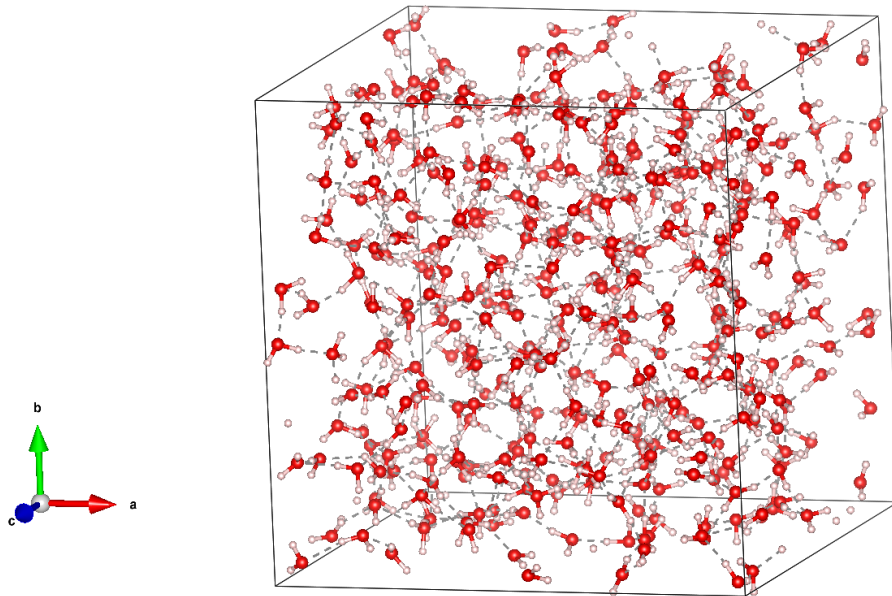


Figure 40: TIP3P water model at 300K.

Secondly a single uranyl ion was optimised in DL_POLY, run as a gas

phase molecule at 300K using the NVT ensemble with a Hoover thermostat and a timestep of 0.001 picoseconds. The uranyl ion is shown in figure 41.

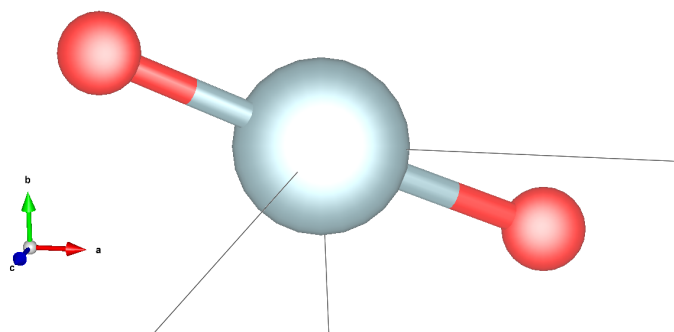


Figure 41: Uranyl ion at 300K. The U—O bond length is 1.81 Å

The uranyl ion was then combined with a box of TIP3P water containing 527 water molecules and optimised at 300K. Similar simulations were run but with the partial charges on the oxygen and uranium of the uranyl ion altered; the values are shown in Table 71.

Table 71: Varied partial charges (q_u) on uranyl ion used in molecular dynamics modelling of the uranyl ion in water, using potentials as Guilbaud and Wipff^[192]

Species			
Ion	Charge (e)	Ion	Charge (e)
Uranyl Uranium (U)	2.000	Uranyl Oxygen (Ou)	0.000
Uranyl Uranium (U)	2.500	Uranyl Oxygen (Ou)	-0.250
Uranyl Uranium (U)	3.000	Uranyl Oxygen (Ou)	-0.500
Uranyl Uranium (U)	4.000	Uranyl Oxygen (Ou)	-1.000
Uranyl Uranium (U)	5.000	Uranyl Oxygen (Ou)	-1.500
Uranyl Uranium (U)	6.000	Uranyl Oxygen (Ou)	-2.000

Only the first two variations in Table 71 (q_u) of 2.000 and 2.5000 on the uranyl uranium) ran successfully. The higher value charges may have failed to optimise because of the greater coulombic attraction between oppositely charged ions, resulting in them being too tightly bound to each other; a greater repulsive force between ions of the same charge may also prevent optimisation. The difference in charge on the oxygen atoms of water and the uranyl ion may also contribute to the failure, mirroring the findings of Guilbaud and Wipff and Jorgensen *et al.*^[205,66].

The U – O_{water} radial distribution function (RDF) for the system where the charge on the uranium atom is +2.5 e is shown in Figure 42. The sharp peak at 1.78 Å, which falls to zero, indicates that water is strongly coordinated to the complex and there is no transfer of water out of this adsorption layer once it forms. Integration of this peak reveals that it contains 4 water

molecules, as opposed to 5 suggested by previous studies^[192,206]. However, there is a smaller peak in the RDF when $r \approx 3 \text{ \AA}$. This peak is, nevertheless, broad and does not drop fully to zero as the separation is increased, suggesting that this fifth water molecule is less strongly bound and the actual molecule present at this U – O separation varies throughout the simulation.

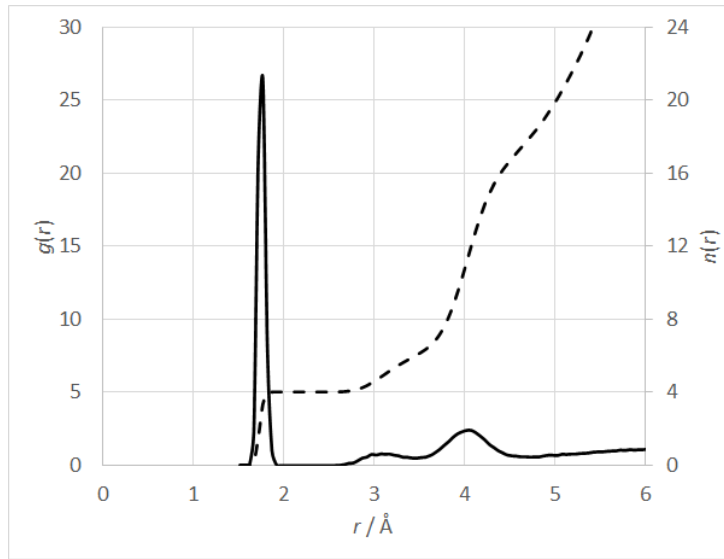


Figure 42: The U—O radial distribution function for a Uranyl ion in water using the potential parameters of Guilbaud and Wipff with a charge of $+2.5 e$ on the central uranium ion. $g(r)$ (solid line) is the RDF, $n(r)$ (dotted line) is the integrated value showing the number of water molecules

To further probe the mobility of the water molecule associated with the peak at 3 \AA we note that according to statistical thermodynamics the free energy of a system is given by:

$$A = -RT \ln Q \quad (115)$$

where R is the gas constant and Q is the total partition function. Since the RDF provides a description of all the atoms in the system, it can be shown to be a good approximation of the partition function and because the RDF converges to 1 at large r , then the free energy will become zero at infinite separation of the ions. Thus, transforming the RDF in this way, gives a measure of the change in free energy as a water molecule is brought from infinity towards the hydration shell^[207,208]. (The rate of observed exchange in water molecules in a long simulation is an indication of the size of energy barriers that are present for adsorption and desorption. It is therefore reasonable that an estimate of the energy barriers can be used estimate the rate of exchange. The approach is at best semi-quantitative but does give a good indication of the energy barriers present in the system). Such a plot is shown in Figure 43 where a large activation barrier is noted at around 15 kJ mol^{-1} ($\approx 6 RT$), calculated for a molecule from the bulk solution moving into the innermost hydration layer, with a barrier of around 22 kJ mol^{-1} ($\approx 9 RT$) corresponding to a molecule desorbing from this layer. Both these values are significantly larger than the kinetic energy possessed by the molecules, clear when the energy is expressed in units of RT , and hence explains why there is no observed exchange of the four most tightly bound molecules in the hydration layer at ambient temperatures.

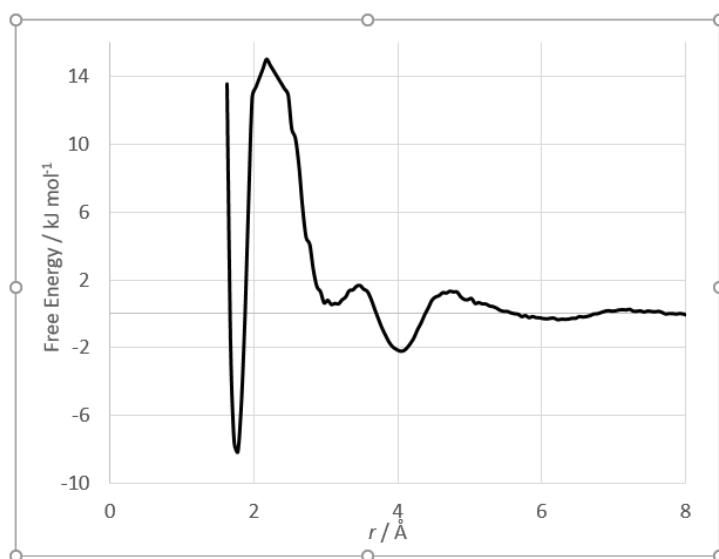


Figure 43: The change in free energy as a water molecule approaches the hydration layer of the uranyl ion

The activation barriers for the fifth molecule moving from the bulk to a U—O separation of 3 \AA is far smaller as is illustrated in Figure 44. Here, the activation barrier for a water molecule moving from the bulk solution into this level is 1.66 kJ mol^{-1} and 1.12 kJ mol^{-1} for it to move back into the bulk solution. As both of these values are smaller than $RT = 2.49 \text{ kJ mol}^{-1}$ @ 300 K it is clear that there will be a fast transfer of water molecules in and out of this layer. Estimates based on the sizes of the activation barriers quoted in this section suggest that the residence time of the fifth water molecule is 100 times smaller than that of the four innermost water molecules.

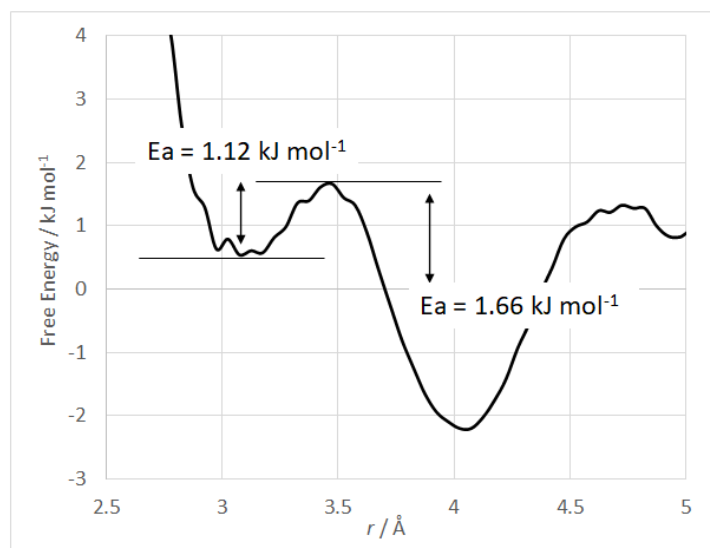


Figure 44: The change in free energy as a water molecule approaches the hydration layer of the uranyl ion

Increasing the simulation run time to almost 20 ns showed the average coordination number of water molecules around the uranyl ion to be 5 (for 99.97% of the time), with a coordination number range of 4 (0.01% of the time) to 6 (0.02% of the time); this gives support to there being 1 less strongly bound water molecule. The converged residence time for a water molecule in the first coordination sphere was shown to be 3006.33 ps.

Figure 45 shows the arrangement of the water molecules which, as in experimental results, are arranged equatorially around the uranyl ion. The U—OW bond distance ranges between 1.76 Å and 1.84 Å.

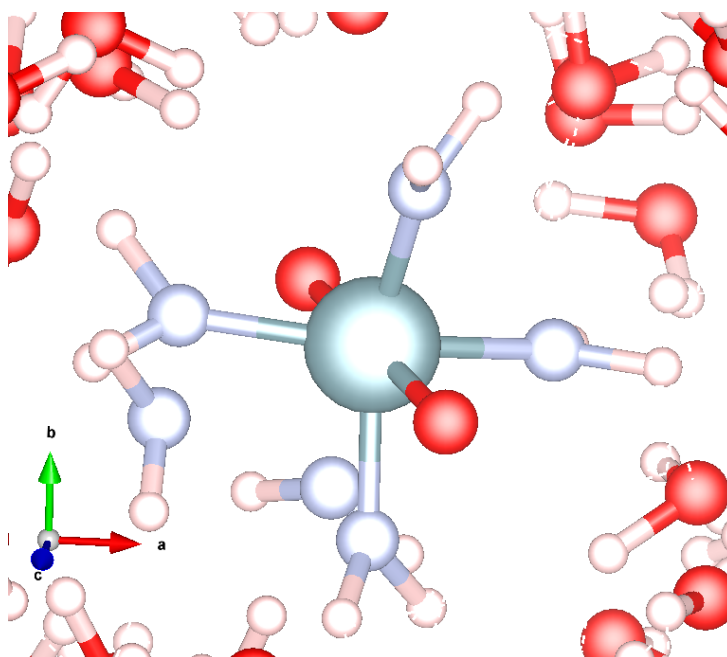


Figure 45: Uranyl ion in water at 300K, showing four coordinated water molecules and an exchange of the fifth coordinated water molecule (adjacent water molecules removed for clarity). Potentials as Guilbaud and Wipff.

Interatomic potential parameters for actinyl ions were also developed by Rai *et al*^[209], so it was decided to test these parameters in the same way as those of Guilbaud and Wipff. These parameters are shown in Tables 72 to 75.

Table 72: Partial charges (q_u) on ions used in molecular dynamics modelling of the uranyl ion in water, using potentials as Rai *et al*^[209]

Species	
Ion	Charge (e)
Uranyl Uranium (U)	2.5000
Uranyl Oxygen (Ou)	-0.2500
Water Oxygen (Ow)	-0.834
Water Hydrogen (Hw)	0.417

Table 73: Lennard-Jones potentials used in molecular dynamics modelling of the uranyl ion in water, using potentials as Rai *et al*^[209]

Lennard-Jones potentials $A_{ij}r_{ij}^{-12} - B_{ij}r_{ij}^{-6}$		
Ion pair (ij)	A_{ij} (eV \AA^{12})	B_{ij} (eV \AA^6)
U-U	1.464714	0.174608
U-Ou	1.972461	0.214249
U-Ow	15544.053630	13.190587
Ou-Ou	2.648686	0.262517
Ou-Ow	23794.632530	32.640100
Ow-Ow	25246.059000	25.805200

Table 74: Harmonic potentials used in molecular dynamics modelling of the uranyl ion in water, using potentials as Rai *et al*^[209]

Harmonic potentials $k_{ij}/2(r_{ij} - r_0)^2$		
Species (ij)	k_{ij} (eV Å ⁻²)	r_0 (Å)
U-Uo	43.364254	1.8000
Ow-Hw	23.990700	0.9572

Table 75: Three-body potentials used in molecular dynamics modelling of the uranyl ion in water, using potentials as Rai *et al*^[209]

Three-body potentials $k_{ijk}/2(\theta_{ijk} - \theta_0)^2$		
Species (ijk)	k_{ijk} (eV rad ⁻²)	θ_0 (deg)
Ou-U-Ou	13.009276	180.00
Hw-Ow-Hw	4.338300	104.52

The uranyl ion was again combined with a box of TIP3P water containing 527 water molecules and optimised at 300K using the NPT ensemble with a Hoover thermostat and a timestep of 0.001 picoseconds. Similar simulations were run but with the partial charges on the oxygen and uranium of the uranyl ion altered; the values are shown in Table 76.

Table 76: Varied partial charges (q_u) on uranyl ion used in molecular dynamics modelling of the uranyl ion in water, using potentials as Rai *et al*^[209]

Species			
Ion	Charge (e)	Ion	Charge (e)
Uranyl Uranium (U)	2.000	Uranyl Oxygen (Ou)	0.000
Uranyl Uranium (U)	2.500	Uranyl Oxygen (Ou)	-0.250
Uranyl Uranium (U)	3.000	Uranyl Oxygen (Ou)	-0.500
Uranyl Uranium (U)	4.000	Uranyl Oxygen (Ou)	-1.000
Uranyl Uranium (U)	5.000	Uranyl Oxygen (Ou)	-1.500
Uranyl Uranium (U)	6.000	Uranyl Oxygen (Ou)	-2.000

As with the Guilbaud and Wipff potentials, only the first two variations in Table 76 (q_u of 2.000 and 2.5000 on the uranyl uranium) were modelled successfully.

The U – O_{water} radial distribution function (RDF) for the system where the charge on the uranium atom is +2.0 e is shown in Figure 46. There is again a sharp peak, in this case at 2.03 Å, indicating an adsorption layer which is strongly coordinated; this peak is a little further away from the central uranium atom than when using the potentials developed by Guilbaud and Wipff, but the sharpness of the peak is similar, though it does not drop fully to zero which indicates that some water transfer from this layer may occur. Integration of the area under this peak indicates there are 4 water molecules, which is in agreement with the number when using the potentials of Guilbaud and Wipff. Once more there is a smaller peak in the RDF when

the $n(r) \approx 3$ Å. This peak is again broad and does not drop fully to zero as the separation is increased, suggesting that this fifth water molecule is less strongly bound and the actual molecule present at this U – O separation varies throughout the simulation, in agreement with the result shown when using the Guilbaud and Wipff potentials.

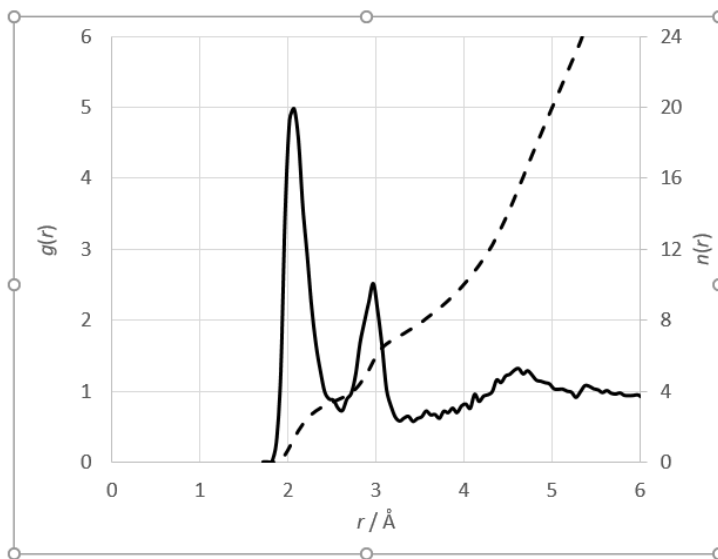


Figure 46: The U—O radial distribution function for a Uranyl ion in water using the potential parameters of Rai *et al* with a charge of $+2.0 e$ on the central uranium ion. $g(r)$ (solid line) is the RDF, $n(r)$ (dotted line) is the integrated value showing the number of water molecules

Transforming the RDF as before, to give an approximate measure of the change in free energy as a water molecule is brought from infinity towards the hydration shell, is shown in Figure 47. The activation barrier calculated for a water molecule moving from the bulk solution to the innermost hydration layer is much lower in this case, around 1 kJ mol^{-1} , with a barrier of around 5 kJ mol^{-1} ($\approx 2 \text{ RT}$) corresponding to a molecule desorbing from this layer. Thus with the potentials of Rai *et al*, in terms of RT , the energy requirement

is such that desorption from the innermost hydration layer remains unlikely; if and when it does occur, another water molecule will be adsorbed rapidly.

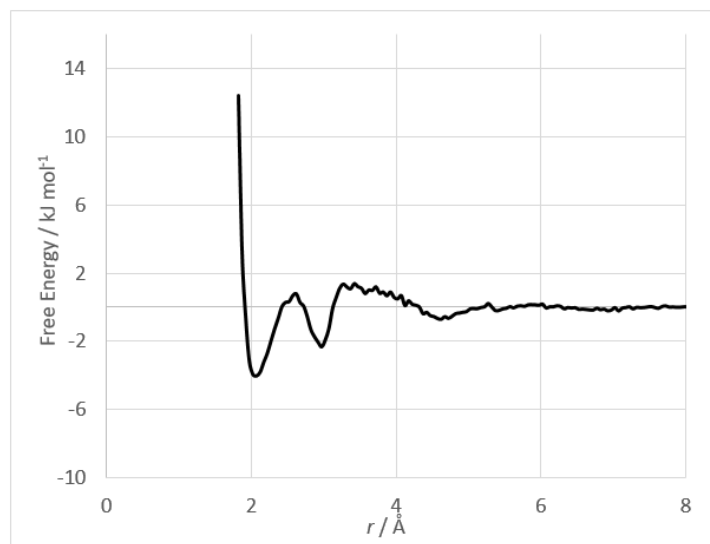


Figure 47: The change in free energy as a water molecule approaches the hydration layer of the uranyl ion

The activation barrier for the fifth molecule moving from the bulk to a U—O separation of 3 \AA is smaller as is illustrated in Figure 48. Here, the activation barrier for a water molecule moving from the bulk solution into this level is 1.38 kJ mol^{-1} and 3.68 kJ mol^{-1} for it to move back into the bulk solution. As the adsorption value is smaller than $RT = 2.49 \text{ kJ mol}^{-1}$ @ 300 K there will be a fast transfer of water molecules into this layer. The desorption value is greater than RT , thus desorption from this layer will be slow.

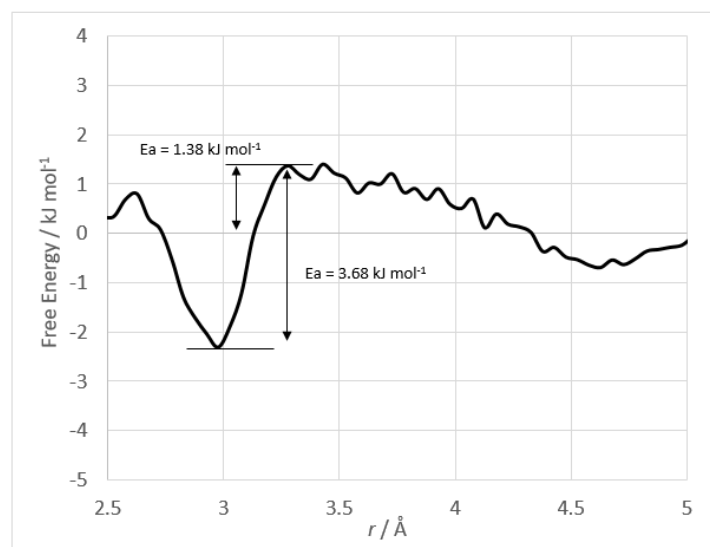


Figure 48: The change in free energy as a water molecule approaches the hydration layer of the uranyl ion

Figure 49 shows the arrangement of the water molecules which are again arranged equatorially around the uranyl ion. The U—OW bond distance ranges between 1.73 Å and 1.80 Å. This places the first hydration shell a little closer (around 0.03 Å) than when using the potentials of Guilbaud and Wipff.

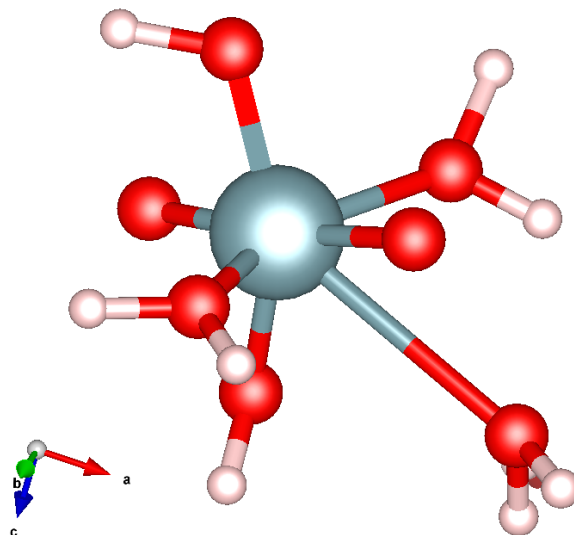


Figure 49: Uranyl ion in water at 300K, showing four coordinated water molecules and, where the bond is elongated, an exchange of the fifth coordinated water molecule (adjacent water molecules removed for clarity). Potentials as Rai *et al.*

As noted by Bardin *et al* when conducting an NMR study of the hydration of the actinyl ion, there are few comparative studies analysing the exchange of water molecules between hydration shells, in either experiment or modelling of $[\text{UO}_2(\text{H}_2\text{O})_5]^{2+}$ [210]. However, of the studies available, Wahlgren *et al* investigated uranyl complexes in alkaline solution with a combined theoretical and experimental approach and found, similarly to this work, that the four-plus-one coordination (along with five-coordinated systems) was present, involving a combination of water molecules and hydroxide ions [211]. Using X-ray scattering on the coordination environment of the uranyl ion in acidic aqueous solution allowed Neufeind *et al* to determine that the dominant species was the uranyl coordinated to five water molecules, but

that a small percentage of the uranyl ions were coordinated to four water molecules^[212]. They conclude that this is consistent with a dynamic equilibrium which favours five coordinating water molecules; they produced radial distribution functions similar to those in this work, showing peaks at 1.77 Å and 2.42 Å which correspond to four and one water molecules respectively.

5.4 Conclusions

Transferable, reliable potentials are clearly required for modelling large systems which are beyond the scope of DFT because of their size. This chapter describes and uses a methodology for generating, testing and refining these potentials without the need for computationally expensive fitting procedures. The methodology uses existing potential sets where these are available as a starting point for testing. Because computational studies have not been used previously to model many of the compounds investigated, comparison of results has been made to empirical data from physical studies and to the results of DFT calculations. The potential sets have been demonstrated to show good agreement with these results, for the purpose of producing a general and interchangeable set of potentials to use in larger mixed systems without the need for systematic fitting.

A summary of the results from this chapter, showing the cell parameters achieved when using each of the potential sets compared to experimentally determined cell parameters, is shown in Table 77:

Table 77: Summary of cell parameters for uranyl minerals, comparing the results from potential sets with experimentally determined values

Cell parameters		Mineral				
		UO ₂ Cl ₂	UO ₂ CO ₃	UO ₂ FeO ₂	UO ₂ (OH) ₂	UO ₂ SO ₄
a (Å)	Experimental	5.725	4.840	4.888	5.644	6.760
	MM output	4.692	4.788	4.883	N/A	6.677
b (Å)	Experimental	8.409	9.273	11.937	6.287	5.711
	MM output	8.009	10.459	11.928	N/A	5.743
c (Å)	Experimental	8.720	4.298	5.110	9.937	12.824
	MM output	9.327	4.340	4.996	N/A	12.787
α (°)	Experimental	90.000	90.000	90.000	90.000	90.000
	MM output	90.000	90.000	90.000	N/A	90.000
β (°)	Experimental	90.000	90.000	90.000	90.000	102.910
	MM output	90.125	90.000	89.990	N/A	102.930
γ (°)	Experimental	90.000	90.000	90.000	90.000	90.000
	MM output	90.000	90.000	90.000	N/A	89.999

The focus of the second part of this chapter was to use molecular dynamics to model the uranyl ion in water and to test existing interatomic potential sets against empirical results. It was shown that the potential sets used could replicate the coordination of water molecules in the equatorial plane of the uranyl ion, with partial charges on the uranium of the uranyl ion of +2.0 and +2.5. Partial charges of +3.0 and above were unsuccessful in producing a viable model. The potentials of Guilbaud and Wipff appear to produce a marginally better result than those of Rai *et al*, based on the slightly longer U—OW bond distance. The U—OW bond distance in the models created

was shorter than that suggested by experimental observation; further work could involve a range of smaller incremental partial charge values and possible refinement of the Lennard-Jones parameters of the model.

Having already established potentials suitable for modelling the layers of green rust, and subsequently for uranyl compounds using counterions which may be found in the interlayers of green rust, the next area to investigate was the modelling of green rust; this would involve combining potentials from the work undertaken in chapters 4 and 5. This work is detailed in the following chapter.

6 Modelling Green Rust 1 and 2 Using DFT and Interatomic Potentials

The modelling of green rust builds on the work in the previous chapter, where the less complex minerals iron (II) hydroxide ($\text{Fe}(\text{OH})_2$) and goethite ($\text{FeO}(\text{OH})$) were successfully modelled using interatomic potentials. It was decided that a green rust 1 (GR1) and a green rust 2 (GR2) compound would be modelled using the potentials developed in chapter 4 and the results compared to those from experiment and from DFT calculations. DFT calculations were particularly desirable in this case due to the lack of experimental data available for green rust compounds. Initial work was undertaken with GR2 and the results from this subsequently used to develop a model for GR1.

6.1 Green Rust 2

The anions in the interlayers of GR2 are 3D in their molecular arrangement, such as the tetrahedral arrangement of the sulfate ion SO_4^{2-} (they are planar in their molecular arrangement in GR1, for example the simple chloride anion Cl^- or the flat arrangement of the trigonal planar carbonate ion CO_3^{2-}). The sulfate anion was chosen to model GR2, which has previously been identified as having a hexagonal crystal structure with $a = b \neq c$ and cell angles of 90° , 90° and 120° .^[162,167,213] Reference was made to the International Crystal Structural Database (ICSD) to review experimentally determined structures of sulfate GR2 which may be suitable as a starting point for the geometry of

a computational model. There proved to be numerous structures composed of the desired elements though not necessarily green rust structures.

The green rust structure published by Simon *et al*^[214] (ICSD code 98534) has $a = b \neq c$ and cell angles of 90° 90° 120° and a hexagonal structure; this was an XRD study and so did not show hydrogen atom positions. This study suggested the ideal formula for sulfate green rust to be $\text{Fe}_4^{2+}\text{Fe}_2^{3+}(\text{OH})_{12}\text{SO}_4 \cdot \sim 8\text{H}_2\text{O}$ with a $P\bar{3}m1$ space group and a trigonal structure. Figure 50 shows a representation of this structure on the (0 0 1) plane.

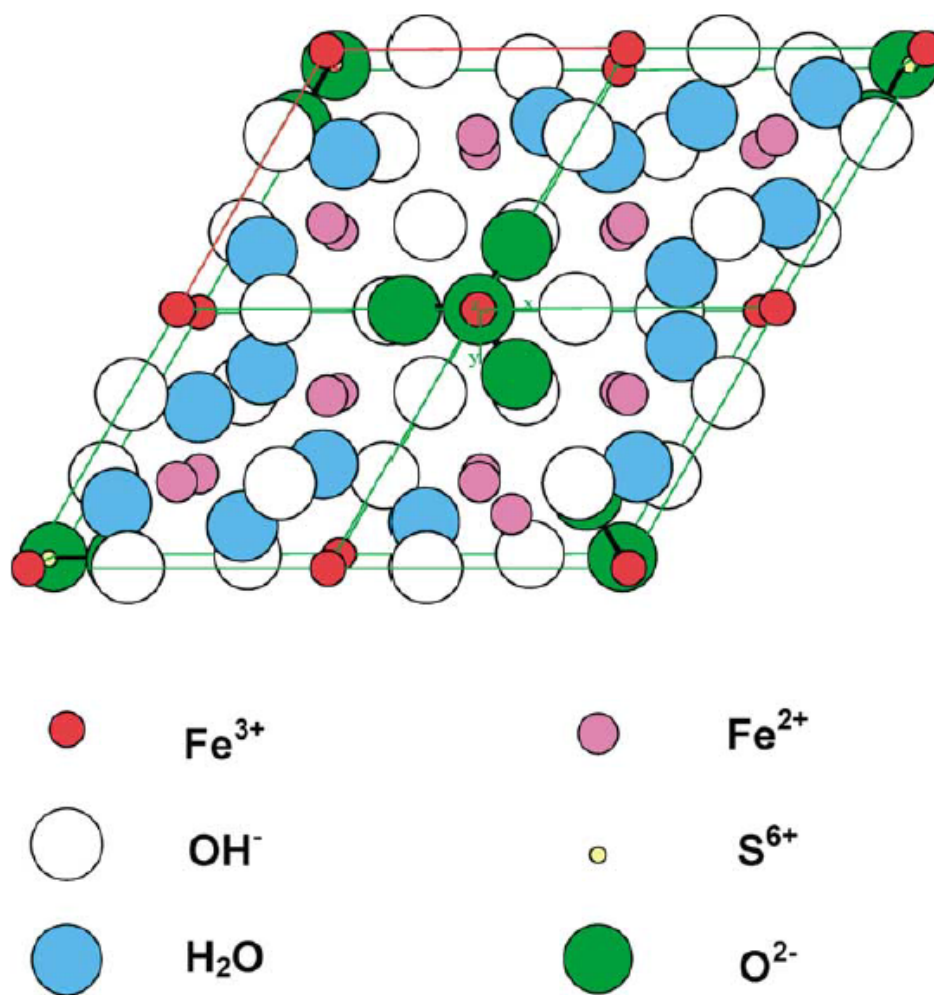


Figure 50: Projection of the lattice of sulfate GR2 on the (0 0 1) plane^[214]

The view in Figure 51 shows that Simon *et al* determined that there were two planes of sulfate anions and water in the interlayers between the planes of double hydroxide. They believed the oxygen atoms of the sulfate groups to be pointing toward the hydroxide layers in a monodentate fashion, with the other three oxygen atoms in a plane parallel to the hydroxide layers and nearer the centre of the interlayer space.

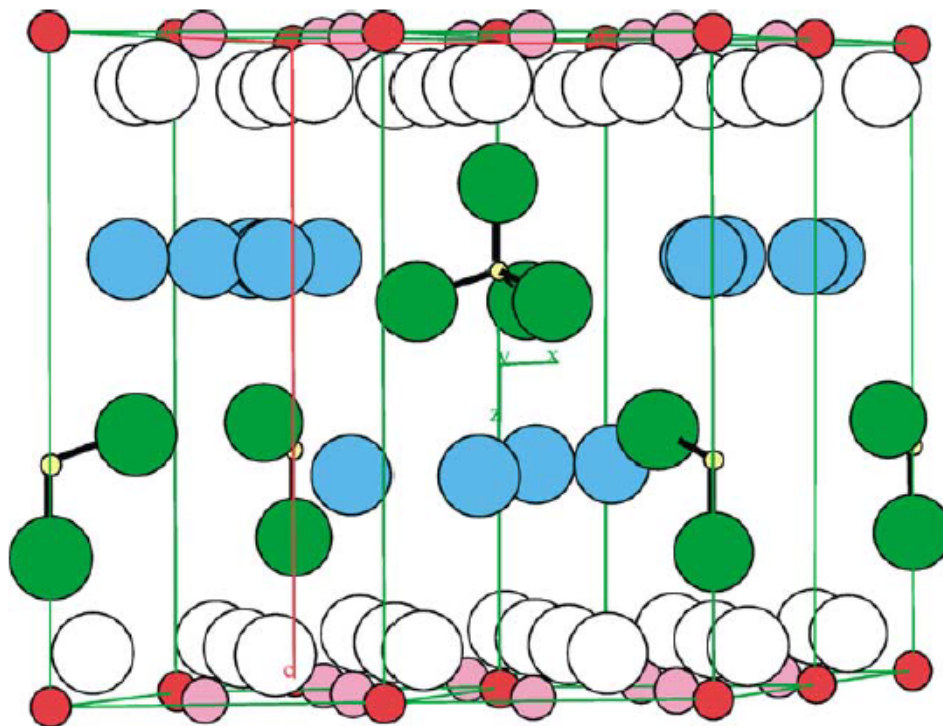


Figure 51: General view of the ordered representation of the crystal structure of sulfate GR2^[214]

Fanfani *et al* published the structure of Butlerite, $\text{Fe}(\text{SO}_4)(\text{OH})(\text{H}_2\text{O})_2$ (ICSD code 15199)^[215] and there were numerous structures for Jarosite such as those determined by Basciano *et al*^[216] (ICSD codes 157710 and 157720). Johansson, Yhland *et al*^[217] published the structure of FeOHSO_4 though this has cell angles of $a = b = c = 90^\circ$ (ICSD code 24079). Ventruti *et al* used XRD and spectroscopy to determine the structure of fibroferrite, $\text{FeOH}(\text{SO}_4) \cdot 5\text{H}_2\text{O}$ ^[218] (ICSD code 252892).

Ruby & Abdelmoula made a study of the structure and formation of aluminium substituted iron (II - III) layered double hydroxides^[219]; they had

the same general formula as the proposed ideal GR2 formula of Simon *et al*, namely $\text{Fe}_4^{2+}\text{Fe}_{(2-6y)}^{3+}\text{Al}_{6y}^{3+}(\text{OH})_{12}\text{SO}_4 \cdot 8\text{H}_2\text{O}$. This structure was also of $P\bar{3}m1$ space group

Unlike Simon *et al*, Ruby & Abdelmoula determined the oxygen atoms of the sulfate to be tridentate in their orientation toward the hydroxide layers. This can be seen in Figure 52. This orientation of the sulfate groups was supported by the findings of Chen *et al*^[220].

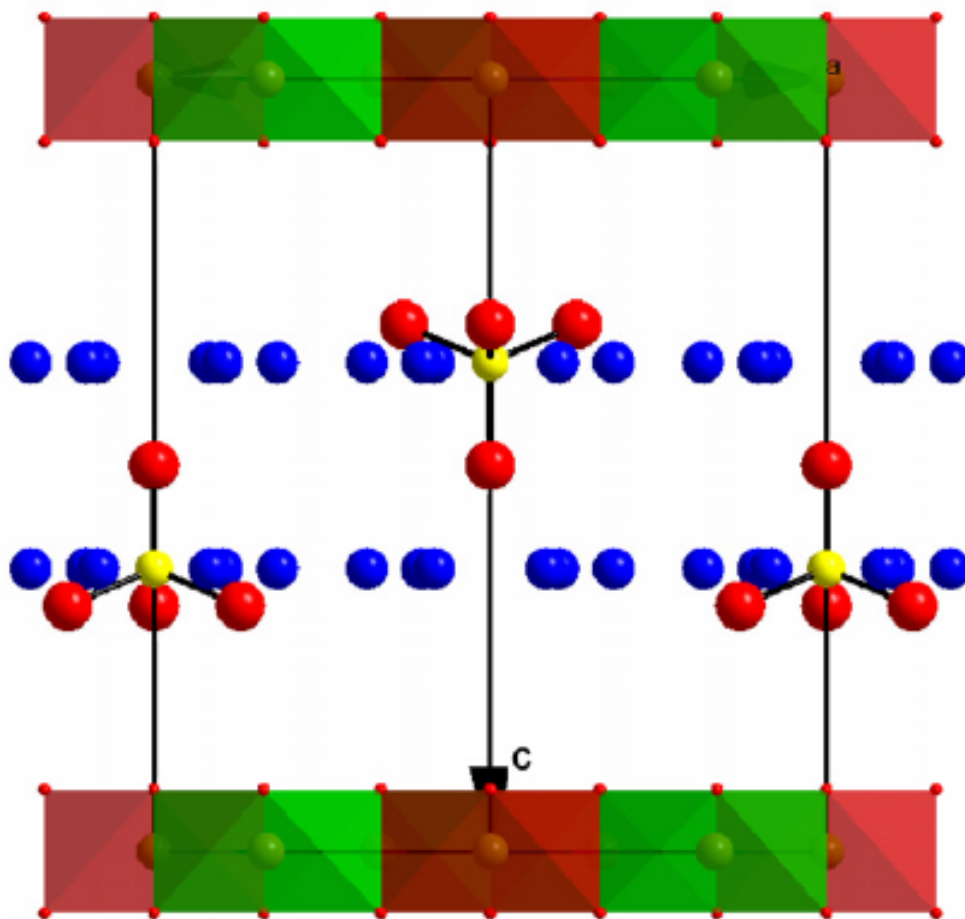


Figure 52: Projection along the (1 1 0) plane of sulfate GR2 showing sulfate tetrahedrons orientated down toward Fe^{3+} ^[219]

The layered double hydroxysulfate structure published by Ruby & Abdelmoula (ICSD code 246125) for $(\text{Fe}_2^{2+} \text{Fe}^{3+})(\text{OH})_6(\text{SO}_4)_{0.5}(\text{H}_2\text{O})_{3.85}$, which is shown in Table 78 and Figure 53, was taken as a starting point, to develop and produce a model of green rust. This structure was chosen rather than that of, for example, Simon *et al*, as the sulfate group orientation would appear more likely to be correct, although both sulfate group orientations were modelled for comparison.

Table 78: Layered double hydroxysulfate cell parameters^[219]

Layered double hydroxysulfate cell parameters	
a (Å)	5.50683
b (Å)	5.50683
c (Å)	10.9664
α (°)	90
β (°)	90
γ (°)	120

HM:P -3 1 m
a=5.507Å
b=5.507Å
c=10.966Å
α=90.000°
β=90.000°
γ=120.000°

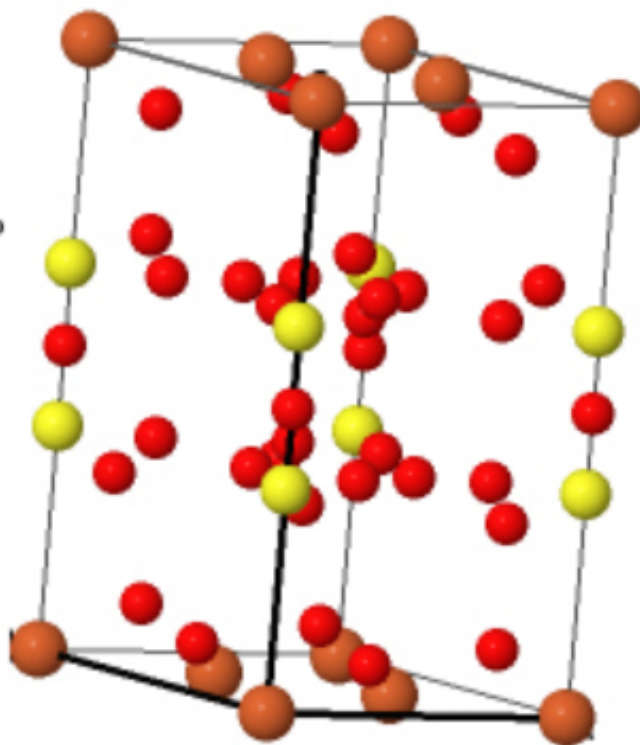


Figure 53: Layered double hydroxysulfate, $(\text{Fe}_2^{2+} \text{Fe}^{3+})(\text{OH})_6(\text{SO}_4)_{0.5}(\text{H}_2\text{O})_{3.85}$ [219]

Key: iron, brown; oxygen, red; sulfur, yellow.

The coordinates given by Ruby & Abdelmoula were used to generate a METADISE input file. Because the unit cell contained only half a sulfate group the cell was grown 2x2x1 (*i.e.* in the x and y planes only) to provide enough charge to accommodate two SO_4^{2-} groups within the cell. The published structure on the ICSD did not contain water or the hydrogen atoms of the hydroxide groups, so it was necessary to add the hydroxide hydrogen atoms. Because these H atoms point in toward the interlayer they were

positioned with the same x and y coordinates as the O atoms they were to be associated with, but with a z coordinate placing them 1Å further toward the centre of the interlayer. The expectation was that once potentials were applied the H atoms would adjust to the most energetically favourable position.

Initial positioning and orientation of the SO_4^{2-} groups was such that the oxygen atoms of the sulfate group would be monodentate in their orientation toward the hydroxide layer. Simon *et al* determined the S atoms to be positioned directly below Fe^{3+} atoms so this was replicated when constructing the model, whilst retaining the other cell parameters of Ruby & Abdelmoula. CASTEP was used to run a DFT geometry optimisation and the results can be seen in Table 79.

Table 79: sulfate green rust DFT modelling results for monodentate sulfate orientation, using PBE_pseudo_D potentials

Results from	Cell dimensions (Å)			% difference to experiment			Cell angles (°)			% difference to experiment		
	a	b	c	a	b	c	α	β	γ	α	β	γ
Experiment ^[219]	5.51	5.51	10.97	-	-	-	90.00	90.00	120.00	-	-	-
PBE_pseudo_D	5.13	5.13	9.29	-6.90	-6.90	-15.31	77.77	77.77	117.84	-13.59	-13.59	-1.80

It was noted that the monodentate sulfate orientation changed such that the oxygen atoms were closer to bidentate in their orientation toward the hydroxide layer, which can be seen in Figure 54. The $\text{O}_S\text{-H}$ bond lengths were all 1.682Å after optimisation, in the bidentate orientation, having been 1.655Å for the closest $\text{O}_S\text{-H}$ bond length in the monodentate orientation prior to optimising the cell.

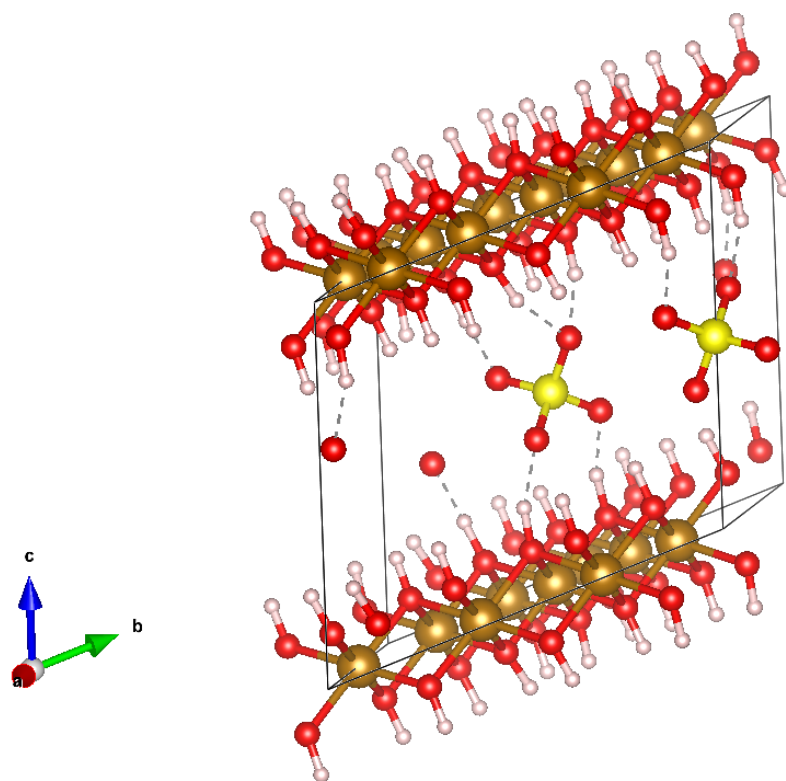


Figure 54: sulfate GR2 from DFT calculation from monodentate orientation, showing sulfate tetrahedron orientation towards hydroxide layer

Initial modelling results are for cells with no water present and are compared to experimental results which contain water. Even so, because the cell angles had changed significantly from the experimental values, optimisation of the same cell but with all the angles constrained was attempted. The geometry optimisation failed to converge with constrained angles, Table 80 shows the cell parameters at the time the calculations were suspended. The change in energy was 7.81×10^{-5} eV, the cut-off value was 2.00×10^{-5} eV, the maximum distance moved by any atom was 1.23×10^{-3} Å, the cut-off value

was 1.00×10^{-3} Å and the overall stress on the system was 3.72×10^{-1} GPa with a cut-off value of 1.00×10^{-1} GPa. The factor furthest from convergence was the maximum force acting on any atom which was 2.46×10^{-1} eV/Å compared to a cut-off value of 5.00×10^{-2} Å. This structure was also energetically unfavourable when compared to the tridentate or unrestrained monodentate structures (398.25 kJ/mol and 456.55 kJ/mol respectively).

Following the monodentate modelling, the sulfate groups were inverted to produce a tridentate orientation of the oxygen atoms toward the hydroxide layer. Running a DFT optimisation in CASTEP produced the structure detailed in Table 80.

For comparison, the same DFT calculation was submitted but with the cell angles constrained. The results from this are shown in Table 80. However, as for the monodentate structure, the geometry optimisation failed to converge for constrained angles and the table reflects the structure at the time the calculations were halted.

Table 80: sulfate green rust DFT modelling results for monodentate, tridentate and tridentate (with constrained cell angles) sulfate orientation, using PBE_pseudo_D potentials. Tridentate with constrained cell angles did not optimise.

Results from	Cell dimensions (Å)			% difference to experiment			Cell angles (°)			% difference to experiment		
	a	b	c	a	b	c	α	β	γ	α	β	γ
Experiment ^[219]	5.51	5.51	10.97	-	-	-	90.00	90.00	120.00	-	-	-
Monodentate	5.22	5.22	11.43	-5.26	-5.26	4.19	90.00	90.00	120.00	0.00	0.00	0.00
Tridentate	5.10	5.10	8.55	-7.44	-7.44	-22.06	91.76	91.76	117.27	1.96	1.96	-2.28
Tridentate (con.)	5.20	5.20	10.71	-5.63	-5.63	-2.37	90.00	90.00	120.00	0.00	0.00	0.00

The monodentate structure was not investigated further as the cell angles changed so much when unconstrained, and the structure was energetically

much less favourable than the tridentate orientation when angles were constrained.

The next step was to take the unconstrained tridentate structure from the DFT calculations and add water into the interlayer; this structure had twice the formula units of the ideal cell, so 4 water molecules were to be added. The paper of Ruby & Abdelmoula did not detail the water within the structure so could not be used for reference as a starting point. Neither was detail of the water molecule positions given in the work of Abdelmoula *et al*^[221]. Simon *et al* did show the water molecules in their structure, although the ideal structure they determined had 8 water molecules and, at variance with this project and other investigations, a monodentate orientation of the sulfate groups towards the hydroxide layer. However, they did indicate that there were two distinct layers of sulfate and water in the interlayer, as shown in Figure 51. Thus it seemed logical to introduce 2 water molecules into each of the respective z planes within the interlayer, matching the z coordinate of each sulfur atom. The oxygen atoms of the water molecules were positioned so as to avoid being centred over an iron atom, as per the findings of Simon *et al*. One water hydrogen atom was positioned in the same z plane as the oxygen, with the x coordinate altered, and the other pointing towards the centre of the interlayer.

CASTEP was used to run the DFT optimisation and the cell parameters from this are shown in Table 81.

Table 81: sulfate green rust DFT modelling results for tridentate sulfate orientation with water, using PBE_pseudo_D potentials

Results from	Cell dimensions (Å)			% difference to experiment			Cell angles (°)			% difference to experiment		
	a	b	c	a	b	c	α	β	γ	α	β	γ
Experiment ^[219]	5.51	5.51	10.97	-	-	-	90.00	90.00	120.00	-	-	-
PBE_pseudo_D	5.14	5.14	8.88	-6.72	-6.72	-19.05	88.48	87.62	117.82	-1.69	-2.64	-1.82

The optimised DFT structure with water present is shown in Figure 55. Movement of the sulfate groups from their tridentate starting position can be observed, one group more so than the other. The O_S-H bond lengths ranged from 1.655Å to 1.870Å for the H of the hydroxide layer; they ranged from 1.647Å to 1.881Å for the H of the water molecules.

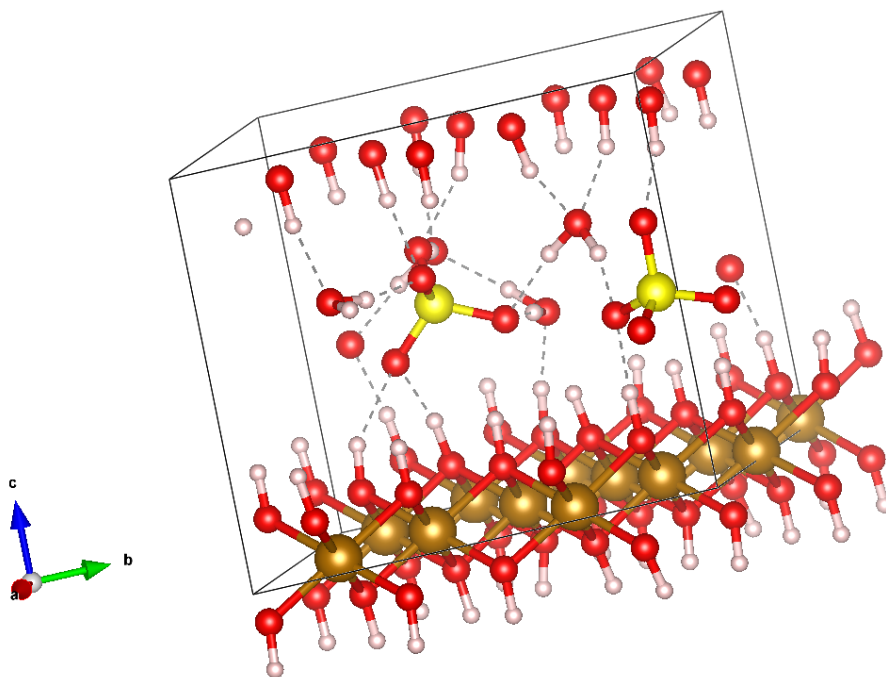


Figure 55: sulfate GR2 with water, from DFT calculation

Following the successful optimisation and addition of water using DFT, the atomic coordinates from the DFT structure were used and the model was tested using interatomic potentials. Initially the structure was modelled without water present; the charges and potentials used are shown in Tables 82 to 85.

Table 82: Partial charges (q_u) on ions used in the testing and interatomic potential modelling of sulfate green rust ($\text{Fe}_6(\text{OH})_6\text{SO}_4$)

Species	
Ion	Charge (e)
Iron (Fe)	1.2250
Hydroxide Oxygen (Oh)	-0.9500
Hydrogen (H)	0.4250
sulfur (S)	1.2075
sulfate Oxygen (Os)	-0.5644

Table 83: Lennard-Jones potentials for sulfate green rust ($\text{Fe}_6(\text{OH})_6\text{SO}_4$), modified CLAYFF potentials

Lennard-Jones potentials $A_{ij}r_{ij}^{-12} - B_{ij}r_{ij}^{-6}$		
Ion pair (ij)	A_{ij} (eV \AA^{12})	B_{ij} (eV \AA^6)
Fe-Fe	304.642804	0.021844
Oh-Oh	27290.954820	27.122570
S-S	34754.089510	34.726882
Os-Os	9355.219594	15.877562
Fe-Oh	3836.983420	0.887919
Fe-Os	2549.975919	0.723792
Fe-S	4335.012030	1.005296
S-Oh	30797.314761	30.690119
S-Os	18243.437141	23.619090
Oh-Os	16170.266760	20.876022

Table 84: Harmonic potentials for sulfate green rust ($\text{Fe}_6(\text{OH})_6\text{SO}_4$), modified CLAYFF potentials

Harmonic potentials $k_{ij}/2(r_{ij} - r_0)^2$		
Species (ij)	k_{ij} (eV \AA^{-2})	r_0 (\AA)
Oh-H	48.059	1.000
S-Os	22.788	1.487

Table 85: Three-body potentials for sulfate green rust ($\text{Fe}_6(\text{OH})_6\text{SO}_4$), modified CLAYFF potentials

Three-body potentials $k_{ijk}/2(\theta_{ijk} - \theta_0)^2$		
Species (ijk)	k_{ijk} (eV rad ⁻²)	θ_0 (deg)
Os-S-Os	6.07	109.47

GULP was used to optimise the structure, initially at constant volume; the parameters of the resultant structure are shown in Table 86, with experimental and DFT results for comparison.

Table 86: sulfate green rust experimentally determined cell parameters compared to interatomic potential modelling results, for tridentate sulfate orientation

Results from	Cell dimensions (Å)			% difference to experiment			Cell angles (°)			% difference to experiment		
	a	b	c	a	b	c	α	β	γ	α	β	γ
Experiment ^[219]	5.51	5.51	10.97	-	-	-	90.00	90.00	120.00	-	-	-
CLAYFF rigid ion	5.10	5.10	8.55	-7.44	-7.44	-22.06	91.76	91.76	117.27	1.96	1.96	-2.28
PBE_pseudo-D	5.10	5.10	8.55	-7.44	-7.44	-22.06	91.76	91.76	117.27	1.96	1.96	-2.28

The structure is shown graphically in Figure 56. The $\text{O}_\text{S}-\text{H}$ bond lengths ranged from 1.753Å to 2.037Å. It was notable that the tridentate orientation of the sulfate molecules was preserved much more than when using the DFT model; the reason for this may be that the lack of a dispersive term in the DFT model can lead to under-binding of the $\text{O}_\text{S}-\text{H}$.

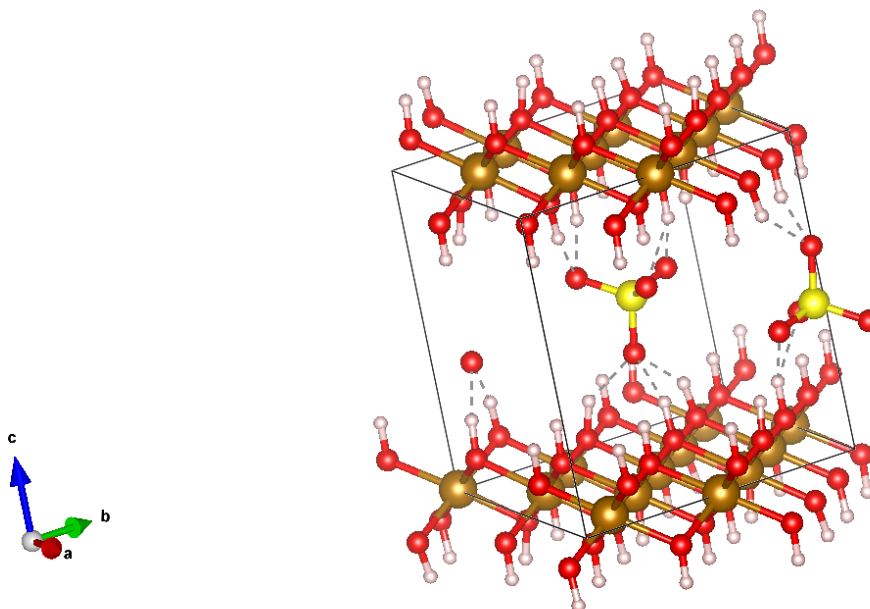


Figure 56: sulfate green rust with tridentate oxygen orientation toward hydroxide layer

Key: iron, brown; oxygen, red; sulfur, yellow; hydrogen, white.

This potential model was then tested at constant pressure and Lennard-Jones potentials for the hydrogen atoms were added. The first potential added was a H-Os potential, which was a 9-6 potential as shown in Table 87; this potential was previously used by Kerisit whilst investigating water structure at hematite-water interfaces^[222]. 9-6 potentials had also been tested previously by Kerisit, Cooke Marmier *et al*^[70], so the potentials were initially tested in this form. The partial charges on the ions and the Lennard-Jones 12-6 potentials remained unaltered, as did the harmonic and three-body potentials.

Table 87: Lennard-Jones potentials for sulfate green rust ($\text{Fe}_6(\text{OH})_6\text{SO}_4$), modified CLAYFF potentials

Lennard-Jones potentials $A_{ij}r_{ij}^{-9} - B_{ij}r_{ij}^{-6}$		
Ion pair (ij)	A_{ij} (eV \AA^{12})	B_{ij} (eV \AA^6)
H-Os	24.000000	6.000000

The structure did not optimise and was visually distorted; the structure when calculations were halted is shown in Table 88.

Table 88: sulfate green rust experimentally determined cell parameters compared to interatomic potential modelling results, for tridentate sulfate orientation with LJ 9-6 H-Os potential added

Results from	Cell dimensions (\AA)			% difference to experiment			Cell angles ($^\circ$)			% difference to experiment		
	a	b	c	a	b	c	α	β	γ	α	β	γ
Experiment ^[219]	5.51	5.51	10.97	-	-	-	90.00	90.00	120.00	-	-	-
CLAYFF rigid ion	5.65	5.64	9.75	2.54	2.36	-11.12	91.60	91.63	117.59	1.78	1.81	-2.01
PBE_pseudo_D	5.10	5.10	8.55	-7.44	-7.44	-22.06	91.76	91.76	117.27	1.96	1.96	-2.28

Because the 9-6 potentials did not produce an acceptable structure the next method tested was to add a H-H (12-6) potential, based on the modified Baram & Parker potential previously referred to in chapter 5^[163], and try the optimisation again; the H-Os (9-6) potential was converted to a H-Os (12-6) potential to make the mixing of potentials simpler. Again the ionic partial charges, harmonic and 3-body potentials remained unaltered. The Lennard-Jones potentials are listed in Table 89.

Table 89: Lennard-Jones potentials for sulfate green rust ($\text{Fe}_6(\text{OH})_6\text{SO}_4$), modified CLAYFF potentials with H-H added

Lennard-Jones potentials $A_{ij}r_{ij}^{-12} - B_{ij}r_{ij}^{-6}$		
Ion pair (ij)	A_{ij} (eV \AA^{12})	B_{ij} (eV \AA^6)
Fe-Fe	304.642804	0.021844
Oh-Oh	27290.954820	27.122570
S-S	34754.089510	34.726882
Os-Os	9355.219594	15.877562
Fe-Oh	3836.983420	0.887919
Fe-Os	2549.975919	0.723792
Fe-S	4335.012030	1.005296
S-Oh	30797.314761	30.690119
S-Os	18243.437141	23.619090
Oh-Os	16170.266760	20.876022
H-H	31.797010	2.183930
H-Fe	635.357101	0.554944
H-S	2182.884081	12.549301
H-Oh	1937.905220	11.100685
H-Os	956.511266	7.798234

The optimisation was successful and the structure parameters are shown in Table 90.

Table 90: sulfate green rust experimentally determined cell parameters compared to interatomic potential modelling results, for tridentate sulfate orientation with H-H potential added

Results from	Cell dimensions (Å)			% difference to experiment			Cell angles (°)			% difference to experiment		
	a	b	c	a	b	c	α	β	γ	α	β	γ
Experiment ^[219]	5.51	5.51	10.97	-	-	-	90.00	90.00	120.00	-	-	-
CLAYFF rigid ion	5.80	5.83	8.70	5.26	5.81	-20.69	77.93	100.07	119.29	-13.41	11.19	-0.59
PBE_pseudo_D	5.10	5.10	8.55	-7.44	-7.44	-22.06	91.76	91.76	117.27	1.96	1.96	-2.28

Whilst the optimisation completed, the cell angles in particular showed deviation from ideal (the α , β and γ angle values deviating from experimental results by -13.41%, +11.19% and -0.59% respectively) so further refinement of the H-H potential was carried out. As the (12-6) H-Os potential had begun as a (9-6) potential, a revised (12-6) H-H potential was also derived from the (9-6) potential and then mixed with the other potentials. These potentials are listed in Table 91. Ionic partial charges, harmonic and 3-body potentials were retained unaltered.

Table 91: Lennard-Jones potentials for sulfate green rust ($\text{Fe}_6(\text{OH})_6\text{SO}_4$), modified CLAYFF potentials with H-H derived from 9-6 potential added

Lennard-Jones potentials $A_{ij}r_{ij}^{-12} - B_{ij}r_{ij}^{-6}$		
Ion pair (ij)	A_{ij} (eV \AA^{12})	B_{ij} (eV \AA^6)
Fe-Fe	304.642804	0.021844
Oh-Oh	27290.954820	27.122570
S-S	34754.089510	34.726882
Os-Os	9355.219594	15.877562
Fe-Oh	3836.983420	0.887919
Fe-Os	2549.975919	0.723792
Fe-S	4335.012030	1.005296
S-Oh	30797.314761	30.690119
S-Os	18243.437141	23.619090
Oh-Os	16170.266760	20.876022
H-H	4888.303112	0.415580
H-Fe	1221.797622	0.095336
H-S	16756.942628	4.307416
H-Oh	14832.906484	3.804625
H-Os	9786.992487	3.090231

The optimisation was successful and the results are shown in Table 92. This structure is shown in Figure 57

Table 92: sulfate green rust experimentally determined cell parameters compared to interatomic potential modelling results, for tridentate sulfate orientation with H-H derived from 9-6 potential added

Results from	Cell dimensions (Å)			% difference to experiment			Cell angles (°)			% difference to experiment		
	a	b	c	a	b	c	α	β	γ	α	β	γ
Experiment ^[219]	5.51	5.51	10.97	-	-	-	90.00	90.00	120.00	-	-	-
CLAYFF rigid ion	5.94	5.94	10.64	7.80	7.80	-3.01	90.09	90.06	119.55	1.00	0.07	-0.38
PBE_pseudo-D	5.10	5.10	8.55	-7.44	-7.44	-22.06	91.76	91.76	117.27	1.96	1.96	-2.28

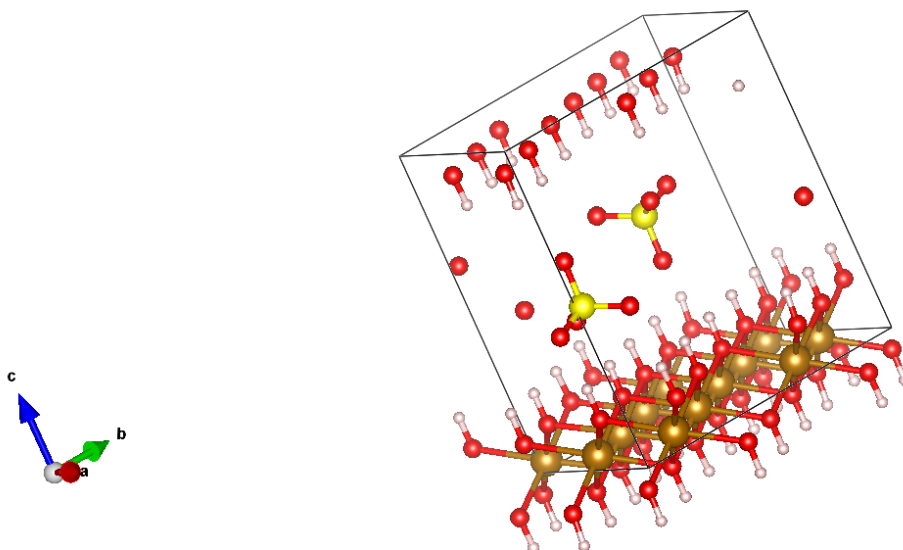


Figure 57: sulfate green rust with tridentate oxygen orientation toward hydroxide layer, with H-H derived from 9-6 potential

Key: iron, brown; oxygen, red; sulfur, yellow; hydrogen, white.

The next step was to add water into the structure; as with the DFT model, four water molecules were added. This was because the formula determined by Ruby & Abdelmoula has two water molecules per sulfate group. The water molecule positions were determined in a similar fashion to that employed

when inserting water into the DFT model. The hydrogen and oxygen atoms of the water molecules had different partial charges to those in the hydroxide and sulfate and are shown in Table 93. Harmonic and three-body bonding terms were added for the water molecules and these are detailed in tables 95 and 96 respectively. The (12-6) Lennard-Jones potentials for the hydrogen and oxygen of the water molecules were mixed with the other potentials and are listed in Table 94

Table 93: Partial charges (q_u) on ions used in the testing and interatomic potential modelling of sulfate green rust with water ($\text{Fe}_6(\text{OH})_6\text{SO}_4 \cdot 0.5\text{H}_2\text{O}$)

Species	
Ion	Charge (e)
Iron (Fe)	1.2250
Hydroxide Oxygen (Oh)	-0.9500
Hydroxide Hydrogen (H)	0.4250
sulfur (S)	1.2075
sulfate Oxygen (Os)	-0.5644
Water Oxygen (Ow)	-0.8200
Water Hydrogen (Hw)	0.4100

Table 94: Lennard-Jones potentials for sulfate green rust ($\text{Fe}_6(\text{OH})_6\text{SO}_4$), modified CLAYFF potentials with H-H derived from 9-6 potential, with water

Lennard-Jones potentials $A_{ij}r_{ij}^{-12} - B_{ij}r_{ij}^{-6}$		
Ion pair (ij)	A_{ij} (eV \AA^{12})	B_{ij} (eV \AA^6)
Fe-Fe	304.642804	0.021844

Continuation of Table 94

Ion pair (ij)	A_{ij} (eV Å ¹²)	B_{ij} (eV Å ⁶)
Oh-Oh	27290.954820	27.122570
S-S	34754.089510	34.726882
Os-Os	9355.219594	15.877562
Fe-Oh	3836.983420	0.887919
Fe-Os	2549.975919	0.723792
Fe-S	4335.012030	1.005296
S-Oh	30797.314761	30.690119
S-Os	18243.437141	23.619090
Oh-Os	16170.266760	20.876022
H-H	4888.303112	0.415580
H-Fe	1221.797622	0.095336
H-S	16756.942628	4.307416
H-Oh	14832.906484	3.804625
H-Os	9786.992487	3.090231
Ow-Ow	27290.954820	27.122570
Ow-S	30797.314761	30.690119
Ow-Os	16170.266760	20.876022
Ow-Oh	27290.954820	27.122570
Ow-Fe	3836.983420	0.887919
Ow-H	14832.906484	3.804625
Ow-Hw	14832.906484	3.804625
Hw-Hw	4888.303112	0.415580

Continuation of Table 94		
Ion pair (ij)	A_{ij} (eV Å ¹²)	B_{ij} (eV Å ⁶)
Hw-H	4888.303112	0.415580
Hw-Oh	14832.906484	3.804625
Hw-Os	9786.992487	3.090231
Hw-S	16756.942628	4.307416
Hw-Fe	1221.797622	0.095336

Table 95: Harmonic potentials for sulfate green rust with water ($\text{Fe}_6(\text{OH})_6\text{SO}_4 \cdot 0.5\text{H}_2\text{O}$), modified CLAYFF potentials

Harmonic potentials $k_{ij}/2(r_{ij} - r_0)^2$		
Species (ij)	k_{ij} (eV Å ⁻²)	r_0 (Å)
Oh-H	48.059	1.000
Ow-Hw	48.059	1.000
S-Os	22.788	1.487

Table 96: Three-body potentials for sulfate green rust with water ($\text{Fe}_6(\text{OH})_6\text{SO}_4 \cdot 0.5\text{H}_2\text{O}$), modified CLAYFF potentials

Three-body potentials $k_{ijk}/2(\theta_{ijk} - \theta_0)^2$		
Species (ijk)	k_{ijk} (eV rad ⁻²)	θ_0 (deg)
Os-S-Os	6.07	109.47
Hw-Ow-Hw	3.97	109.47

The structure optimised successfully and the cell parameter results are

shown in Table 97. This structure is shown in Figure 58

Table 97: sulfate green rust experimentally determined cell parameters compared to interatomic potential modelling results, for tridentate sulfate orientation with H-H derived from 9-6 potential and water added

Results from	Cell dimensions (Å)			% difference to experiment			Cell angles (°)			% difference to experiment		
	a	b	c	a	b	c	α	β	γ	α	β	γ
Experiment ^[219]	5.51	5.51	10.97	-	-	-	90.00	90.00	120.00	-	-	-
CLAYFF rigid ion	5.95	5.94	10.77	7.99	7.80	-1.82	90.67	86.83	119.81	0.74	-3.52	-0.16
PBE_pseudo_D	5.10	5.10	8.55	-7.44	-7.44	-22.06	91.76	91.76	117.27	1.96	1.96	-2.28

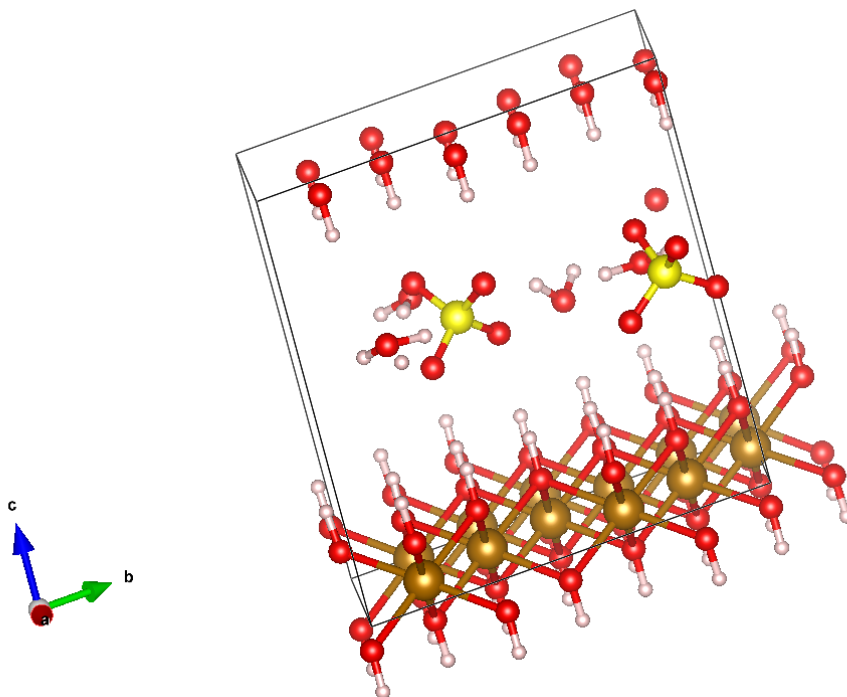


Figure 58: sulfate green rust with tridentate oxygen orientation toward hydroxide layer, with H-H derived from 9-6 potential and water added

Key: iron, brown; oxygen, red; sulfur, yellow; hydrogen, white.

This model of the bulk structure of sulfate green rust 2 was within reasonable limits of the experimentally determined structure and thus provided

a suitable basis to move on to the investigation of green rust 2 surfaces.

6.1.1 Green Rust 2 Surfaces

Having demonstrated it to be viable to model the bulk green rust 2 structure using a potential model the next stage of the project was to try and model surfaces, so these could be used to investigate interactions at the surface and thus at interlayers within the bulk structure. It was decided to start by modelling the simple low index (1 0 0), (0 0 1) and possibly the (0 1 0) surfaces, then move onto other surfaces if these were successful and time allowed. The (1 0 0) surface is perpendicular to the layers of the bulk structure (as is the (0 1 0) surface, which is rotated through 90° from the (1 0 0) surface) and the (0 0 1) surface is parallel to these layers. METADISE would be used to cut the surfaces and these surfaces would then be relaxed using GULP. The bulk structure modelled in section 6.1 was taken and the desired Miller index surface generated using METADISE.

Using the (1 0 0) surface as an example, the methodology was as described below:

The output from the bulk structure was used to provide the Cartesian lattice vectors and fractional coordinates for the cell. The atomic charges remained the same as those in the bulk structure and terms were input to identify bonded atoms (such as the Ow and Hw atoms). Running METADISE to generate the (1 0 0) surface produced no results, meaning no cut producing the (1 0 0) surface without a dipole could be found. Permitting a dipole allowed METADISE to generate a number of surfaces; the lowest dipole value in this case was 0.495468eV so a dipole tolerance value of 0.5eV was added

and METADISE re-run to generate to generate the surface cuts falling within this limit, producing a shorter list of surfaces which was more easily manageable. The cut with the lowest dipole was run through METADISE three times to produce three different outputs; a bulk, a surface and a slab. These files could then be used to create input files for GULP, which would be used to relax the structures. The METADISE output for the bulk structure was used to generate a GULP input; this input ran and optimised successfully. The structure from the GULP output is shown in Figure 59.

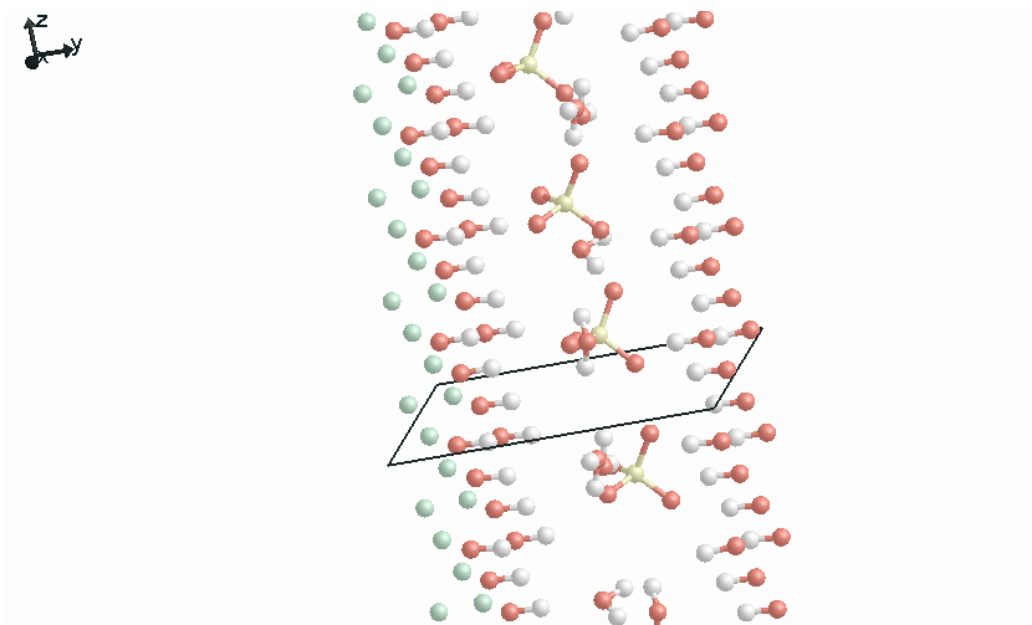


Figure 59: sulfate green rust bulk structure from (1 0 0) surface

Key: iron, green; oxygen, red; sulfur, yellow; hydrogen, white.

Once the bulk structure had been tested the (1 0 0) surface was generated using METADISE and GULP was used to relax the structure; this successfully optimised and is shown in Figure 60.

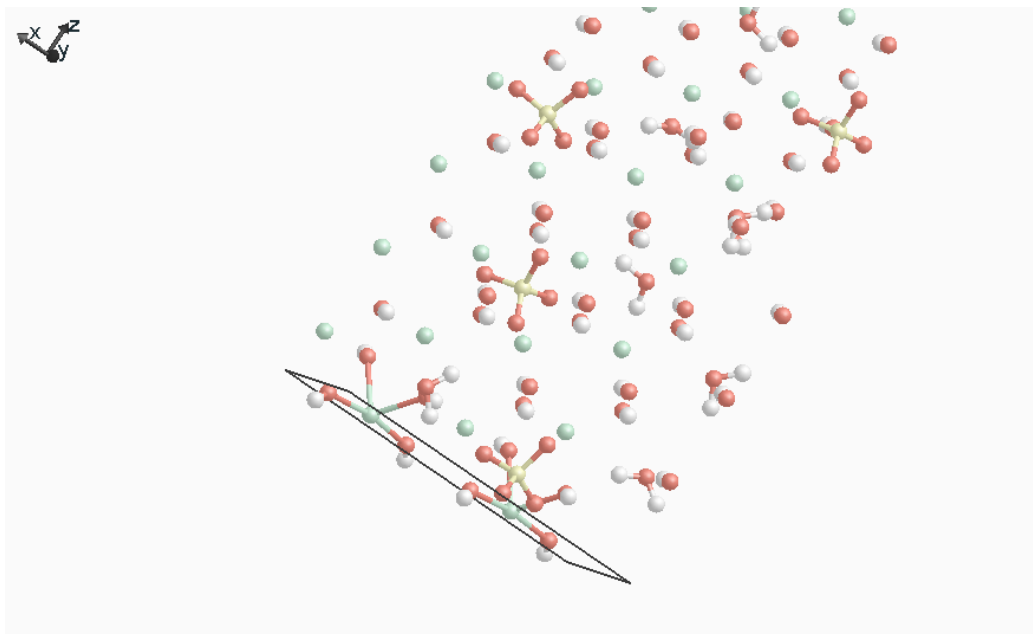


Figure 60: sulfate green rust (1 0 0) surface structure

Key: iron, green; oxygen, red; sulfur, yellow; hydrogen, white.

Because the surface was successfully modelled using this method, the slab was not generated.

The (0 0 1) surface was run using the same methodology and produced the bulk structure as shown in Figure 61.

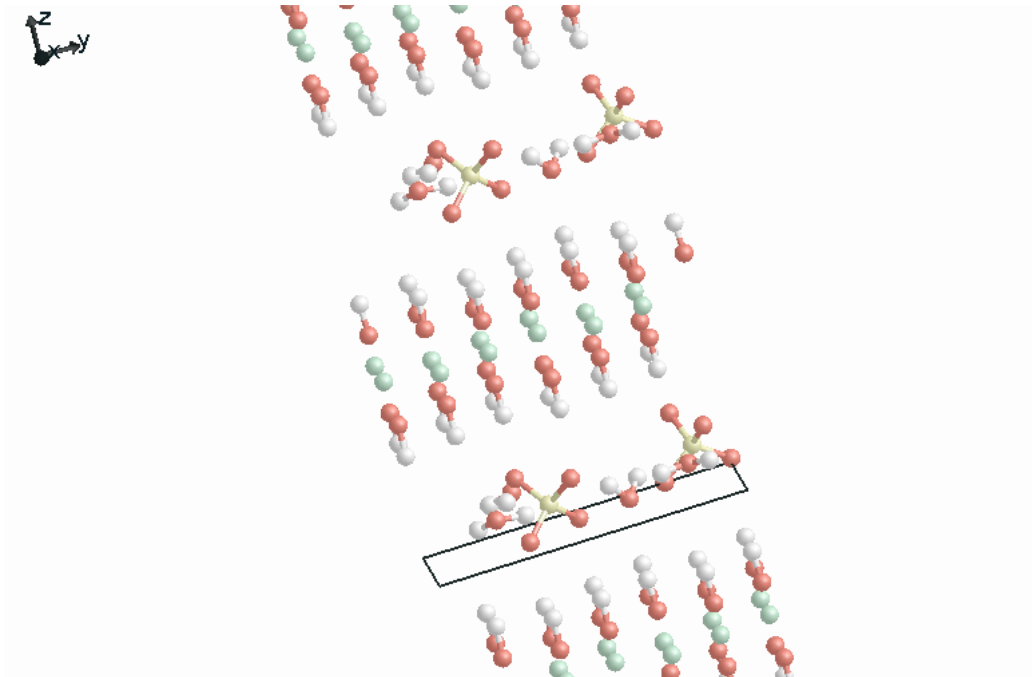


Figure 61: sulfate green rust bulk structure from (0 0 1) surface

Key: iron, green; oxygen, red; sulfur, yellow; hydrogen, white.

Going on to generate the (0 0 1) surface produced the structure shown in Figure 62.

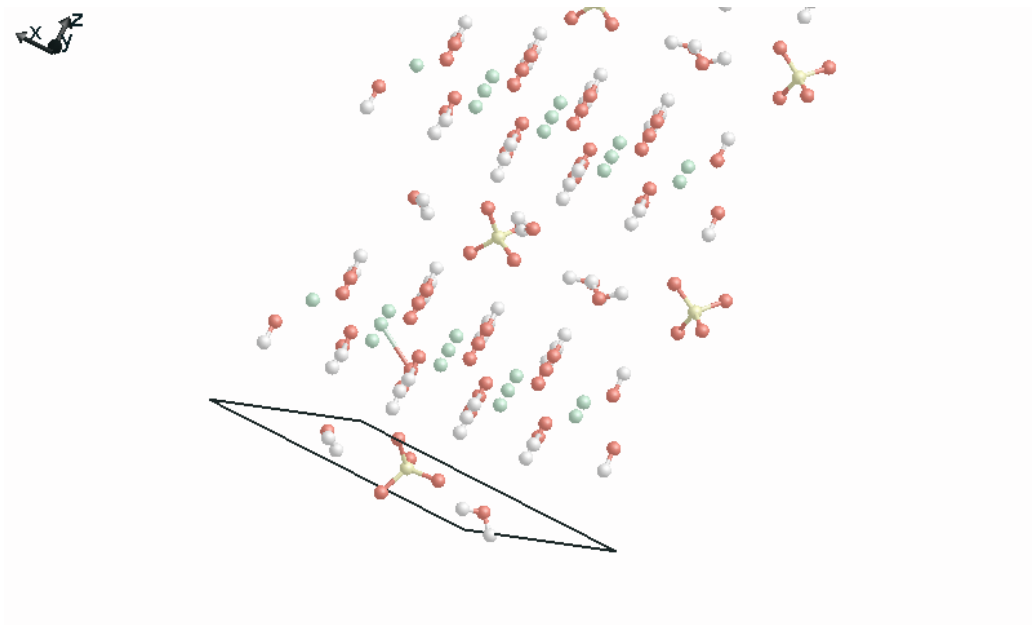


Figure 62: sulfate green rust (0 0 1) surface structure

Key: iron, green; oxygen, red; sulfur, yellow; hydrogen, white.

At the point of addressing the (0 1 0) surface the project was halted due to time restrictions.

The energies and surface area for the (1 0 0) and (0 0 1) surfaces are shown in Table 98.

Table 98: sulfate green rust surfaces: surface areas and energies

Surface	Surface area (\AA^2)	Surface energy (J/m^2)
(1 0 0)	127.930448	0.219905
(0 0 1)	122.574620	0.056578

The equilibrium morphology will likely be dominated by the surface with the lower surface energy, which in this case is the (0 0 1) surface; given how

much more stable than the (1 0 0) surface this is, it would be the surface observed in most cases. However this cannot yet be compared to the other surfaces which were not successfully modelled.

The more stable (0 0 1) surface is parallel to the channels between the double hydroxide layers of sulfate green rust; this should result in ready formation of the channels and a more easy absorption of the uranyl ion into the interlayer.

6.2 Green Rust 1

The structure of chloride GR1 was investigated using X-ray diffraction by Génin *et al* during their study of the structure of fougérite minerals^[223], finding the space group to be $R\bar{3}m$ with cell parameters $a = b \neq c$ and cell angles of 90° 90° 120° . Comparison is made to the chloride GR1 structure determined by Refait *et al* when investigating mechanisms of formation and structure of GR1^[224]; this structure is shown in Figure 63.

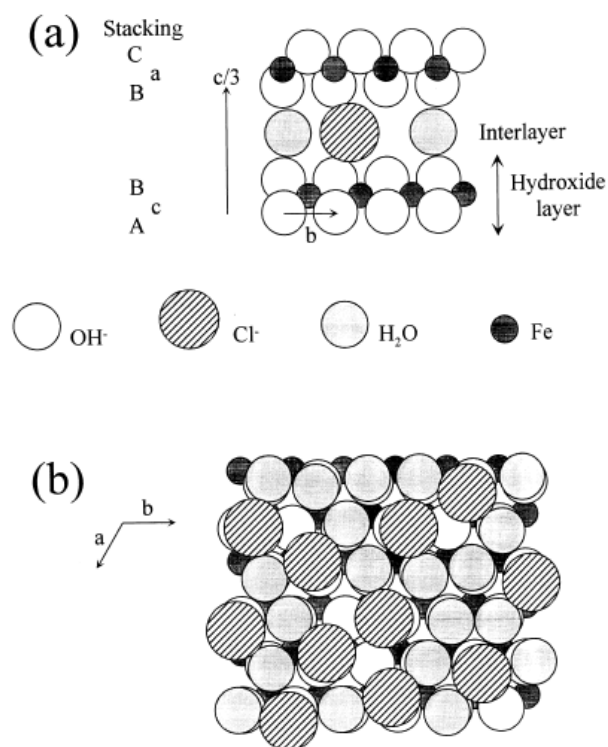


Figure 63: Crystal structure of chloride GR1. (a) Stacking sequence. (b) Disposition of chloride ions and water molecules in interlayer, viewed along (0 0 1). One interlayer, one OH⁻ and one Fe layer below shown.^[224]

The cell parameters determined by Refait *et al* are shown in Table 99. The ideal chloride GR1 formula suggested is $\text{Fe}_3^{2+}\text{Fe}^{3+}(\text{OH})_8 \text{Cl} \cdot n\text{H}_2\text{O}$, with $n \approx 2$, though it was reported that as the Cl⁻ concentration increases this can vary to $\text{Fe}_{2.2}^{2+}\text{Fe}^{3+}(\text{OH})_{6.4} \text{Cl} \cdot n\text{H}_2\text{O}$. No structural change is reported but there is an oxidation of Fe²⁺ to Fe³⁺. The structure was found equivalent to that of iowaite, which is $[\text{Mg}_3^{2+}\text{Fe}^{3+}(\text{OH})_8]^+ [\text{Cl} \cdot 2\text{H}_2\text{O}]^-$. The ideal formula stated, with $n=2$, was corroborated by Abdelmoula *et al* in a study of fougurite mineral occurrence and transformation in hydromorphic soil^[221]. Whilst Refait *et al* suggested the ideal chloride GR1 formula already men-

tioned, they also noted that the sample they studied was close to that of Abdelmoula and co-workers.

Bernal, Dasgupta and Mackay studied the oxides and hydroxides of iron and their topotaxy using X-ray diffraction and ascertained cell parameters for chloride GR1 as shown in Table 99, which compare closely with those found by Refait *et al.*

Table 99: Layered double hydroxychloride (GR1) cell parameters as reported by Refait *et al* and by Bernal *et al* using X-ray diffraction studies

Cell parameter	Refait <i>et al</i> ^[224]	Bernal <i>et al</i> ^[162]
a (Å)	3.190	3.22
b (Å)	3.190	3.22
c (Å)	2.385	2.60
α (°)	90	90
β (°)	90	90
γ (°)	120	120

The changes in $\text{Fe}^{2+}:\text{Fe}^{3+}$ ratios have been noted to occur in chloride GR1 only^[225], likely due to the unique spherical electrical charge which permits a gradual *in-situ* intercalation, which is forbidden for larger divalent anions such as SO_4^{2-} or CO_3^{2-} .

Refait *et al* were able to show the presence of chloride GR1 under varying pH using electrochemically induced corrosion of iron in KCl solutions. Their results are shown in Figure 64. Taking potential values between around -0.54V and 0V, chloride GR1 was shown to be present in the pH range of 5.5 to 12.5; this demonstrates that chloride GR1 is able to exist under both

basic and acidic conditions.

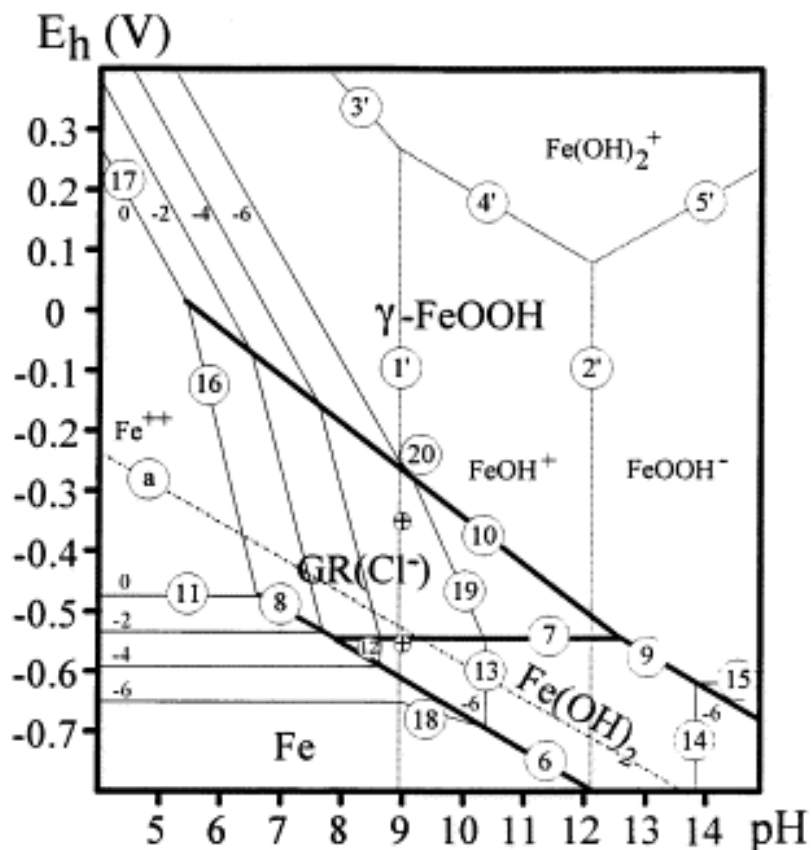


Figure 64: E -pH equilibrium diagram of the system Fe/chloride containing solution at 25°C for an activity $\alpha[\text{Cl}^-] = 0.55$, corresponding to a 1 M KCl solution^[226]. Chloride GR1 was taken at $\text{Fe}_4(\text{OH})_8\text{Cl} \cdot n\text{H}_2\text{O}$ ^[224]

The cell parameters of Refait *et al* were used as comparative values to evaluate the potential model, but rather than using their cell structure (ICSD code 56286) as a starting point, the GR2 potential model already developed was used, and the sulfate anions in the interlayer substituted with chloride anions. Because the anions in GR1 are planar rather than 3D, the chloride ions were introduced centrally in the interlayers, equidistant from each hydroxide layer.

DFT was used to optimise the structure, using PBE_pseudo_D potentials as previously, and resulted in the interlayers closing by around 1Å; this reduced interlayer dimension was anticipated due to the chloride anions being smaller than the sulfate anions they replaced. The structure is shown in Figure 65.

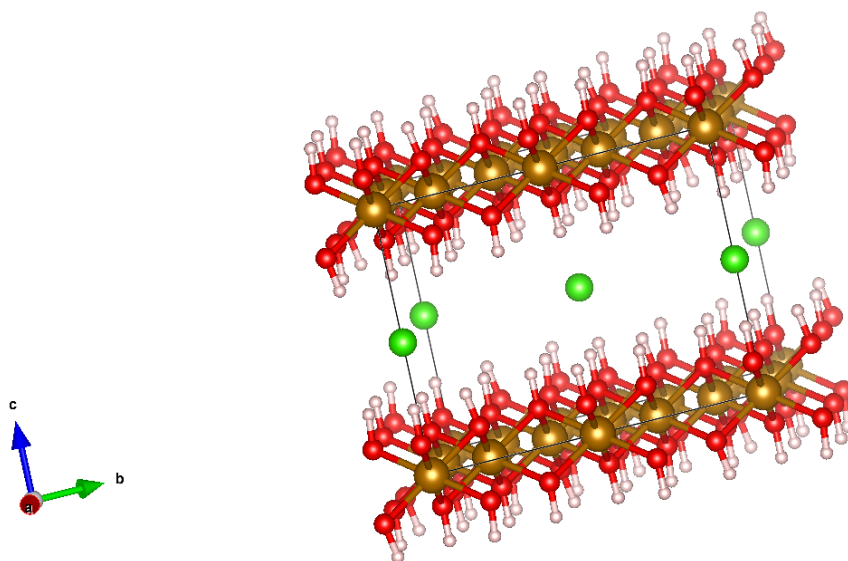


Figure 65: Crystal structure of chloride GR1 from DFT, with 2 chloride ions.

The atomic quantities in this structure were all three times the value of the ideal formula with the exception of the chloride ions, which were twice the ideal formula. In order to compare the cell with the ideal formula ratio of Refait *et al* it was therefore necessary to add a third Cl^- to this structure. The two Cl^- already present in the cell had been positioned as the two SO_4^{2-} in sulfate GR2 as previously stated, so would not be correctly positioned for a structure with three Cl^- . The CASTEP input was generated with the Cl^- ions at the fractional coordinates shown in Table 100. All three chloride ions

were placed centrally in the interlayer, thus all fractional coordinates for the z-axis were 0.50.

Table 100: Chloride ion fractional coordinates used to generate Cartesian coordinates for chloride GR1

Chloride ion	Fractional coordinates		
	x-axis	y-axis	z-axis
Cl1	0.00	0.00	0.50
Cl2	0.33	0.66	0.50
Cl3	0.67	0.34	0.50

The structure was optimised at constant pressure using DFT, again with PBE_pseudo_D potentials. The resultant structure is shown in Figure 66.

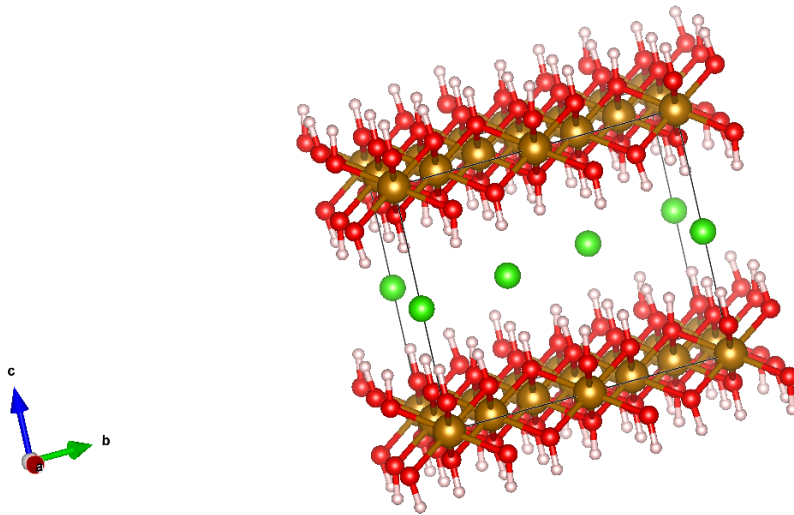


Figure 66: Crystal structure of chloride GR1 from DFT, with 3 chloride ions.

The crystal structure in Figure 66 is a hexagonal structure whereas the structure of Refait *et al* is rhombohedral, with space group $R\bar{3}m$. To compare

the DFT model and experimental structures it was necessary to divide the model structure dimensions along the x and y axes by 2, as the original cell had been grown 2x2x1; once this was done the modelled cell needed to be converted from hexagonal to a rhombohedral structure. The CRYSCON^[227] general crystallographic conversion utility was used to convert the structure and the cell parameters are detailed in Table 101.

Table 101: Chloride green rust DFT modelling results using PBE_pseudo_D potentials

Results from	Cell dimensions (Å)			% difference to experiment			Cell angles (°)			% difference to experiment		
	a	b	c	a	b	c	α	β	γ	α	β	γ
Experiment ^[224]	3.19	3.19	2.39	-	-	-	90.00	90.00	120.00	-	-	-
PBE_pseudo_D	3.96	3.85	3.92	24.14	20.69	64.02	84.28	82.85	83.96	-6.36	-7.94	-30.03

The difference in cell dimensions suggested further refinement may be required, though water was to be added to the structure so this was not considered a significant concern at this stage. Indeed the c parameter in particular is one which changes greatly in layered structures and can prove problematic for physical measurement as it may change during measuring procedures.

Before adding water to the DFT model, the structure with three Cl⁻ counterions was modelled using interatomic potentials. The atomic coordinates from the DFT model were used as a starting point for the potential model, with a -1.0 charge on the Cl⁻ ion, as used in the CLAYFF potentials. The potential parameters used are listed in Tables 102 to 104.

Table 102: Partial charges (q_u) on ions used in the testing and interatomic potential modelling of chloride green rust ($\text{Fe}_4(\text{OH})_8 \text{Cl}$)

Species	
Ion	Charge (e)
Iron (Fe)	1.3000
Hydroxide Oxygen (Oh)	-0.9500
Hydrogen (H)	0.4250
Chlorine (Cl)	-1.0000

Table 103: Lennard-Jones potentials for chloride green rust ($\text{Fe}_4(\text{OH})_8 \text{Cl}$), modified CLAYFF potentials

Lennard-Jones potentials $A_{ij}r_{ij}^{-12} - B_{ij}r_{ij}^{-6}$		
Ion pair (ij)	A_{ij} (eV \AA^{12})	B_{ij} (eV \AA^6)
Fe-Fe	304.642804	0.021844
Oh-Oh	27290.954820	27.122570
Cl-Cl	914162.129100	125.986666
H-H	31.797010	2.183930
Fe-Oh	3836.983420	0.887919
Fe-Cl	16987.462370	1.673741
Fe-H	635.357101	0.554944
Cl-Oh	185709.578409	63.384691
Cl-H	25161.283311	35.834031

Table 104: Harmonic potentials for chloride green rust ($\text{Fe}_4(\text{OH})_8\text{Cl}$), modified CLAYFF potentials

Harmonic potentials $k_{ij}/2(r_{ij} - r_0)^2$		
Species (ij)	k_{ij} (eV \AA^{-2})	r_0 (\AA)
Oh-H	48.059	1.000

GULP was used to relax the structure, the result of which is shown in Figure 67.

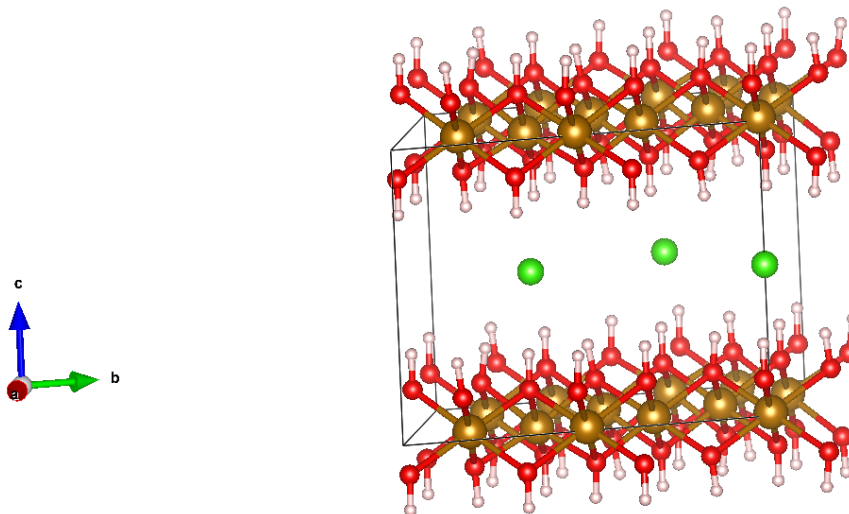


Figure 67: Crystal structure of chloride GR1 using modified CLAYFF potentials, with 3 chloride ions.

This relaxed structure produced cell angles of 90° , 90° and 120° for α , β and γ respectively, matching experimental results. The a and b parameters of the cell increased slightly, though by less than 0.1\AA in each case; the c parameter, already noted to be highly variable, decreased by 0.47\AA (a change of around 5% from the original value).

The Cl^- ions, having been introduced with a fractional coordinate of 0.5 to position them on the centreline of the interlayer, shifted slightly off the centreline, but to maximum fractional value of 0.51. Because the c parameter of the cell was slightly reduced after relaxation it might be expected that the H - Cl separations would also be reduced; this was the case, though the reduction was from 2.84Å to 2.81Å in the largest example.

To add water to the DFT model required 6 water molecules; the ideal formula contains 2 water molecules and all other atomic quantities in the DFT model were three times the ideal formula. METADISE was used to insert oxygen atoms, using the fractional coordinates in Table 105, and the structure run with no potentials.

Table 105: Oxygen atom initial fractional coordinates used to generate Cartesian coordinates for chloride GR1 with water

Oxygen atom	Fractional coordinates		
	x-axis	y-axis	z-axis
O1	0.50	0.67	0.50
O2	0.67	0.50	0.50
O3	0.50	0.33	0.50
O4	0.33	0.50	0.50
O5	0.25	0.25	0.50
O6	0.75	0.75	0.50

Visual inspection of the structure showed adjustment of some oxygen atoms was required as they were too close to the chloride ions. Iterative refinements were made this way until the final fractional coordinates shown

in Table 106 were determined. This structure is shown in Figure 68.

Table 106: Oxygen atom refined fractional coordinates used to generate Cartesian coordinates for chloride GR1 with water

Oxygen atom	Fractional coordinates		
	x-axis	y-axis	z-axis
O1	0.20	0.80	0.50
O2	0.80	0.20	0.50
O3	0.00	0.50	0.50
O4	0.50	0.00	0.50
O5	0.25	0.25	0.50
O6	0.75	0.75	0.50

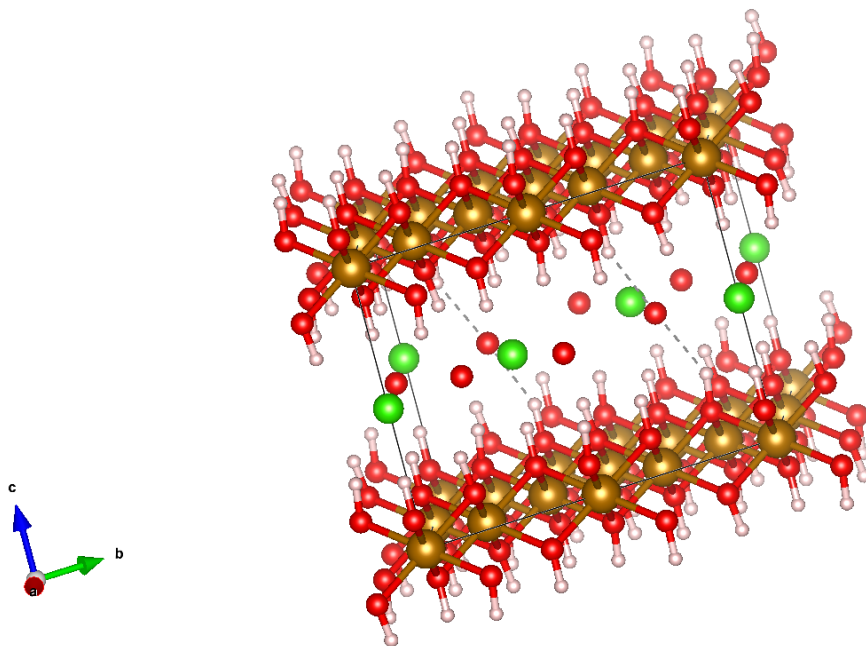


Figure 68: Chloride GR1 with oxygen atom positions refined in METADISE, without potentials.

The next step was to add two hydrogen atoms to each of these oxygen atoms to create the water molecules. The same method was used to position the first of the hydrogen atoms for each oxygen; the y and z coordinates were kept the same as the oxygen atom and the x coordinate was increased by 0.9\AA . To position the second hydrogen atom, using trigonometry and a water molecule bond angle of 109° , the y coordinate was kept unaltered and the x coordinate was decreased by 0.29\AA . The z coordinate was altered by 0.85\AA ; it was decided to begin by having half of the z coordinates in either direction (*i.e.* with the half the hydrogen atoms pointing up and half pointing down, from the centre of the interlayer), so the 0.85\AA was added to three of the hydrogen atom z coordinates and subtracted from the other three. This

resulted in the structure shown in Figure 69.

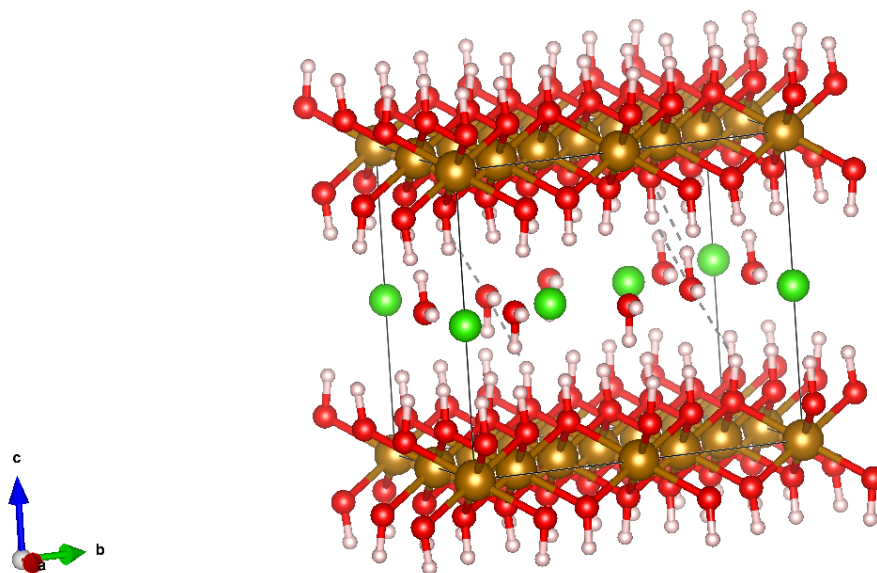


Figure 69: Chloride GR1 with oxygen and hydrogen atom positions refined in METADISE, without potentials.

This structure was used to generate a CASTEP input file and DFT was used to optimise the cell at constant pressure using PBE_pseudo_D potentials. The orientation of the water molecules changed, as expected, and can be seen in Figure 70.

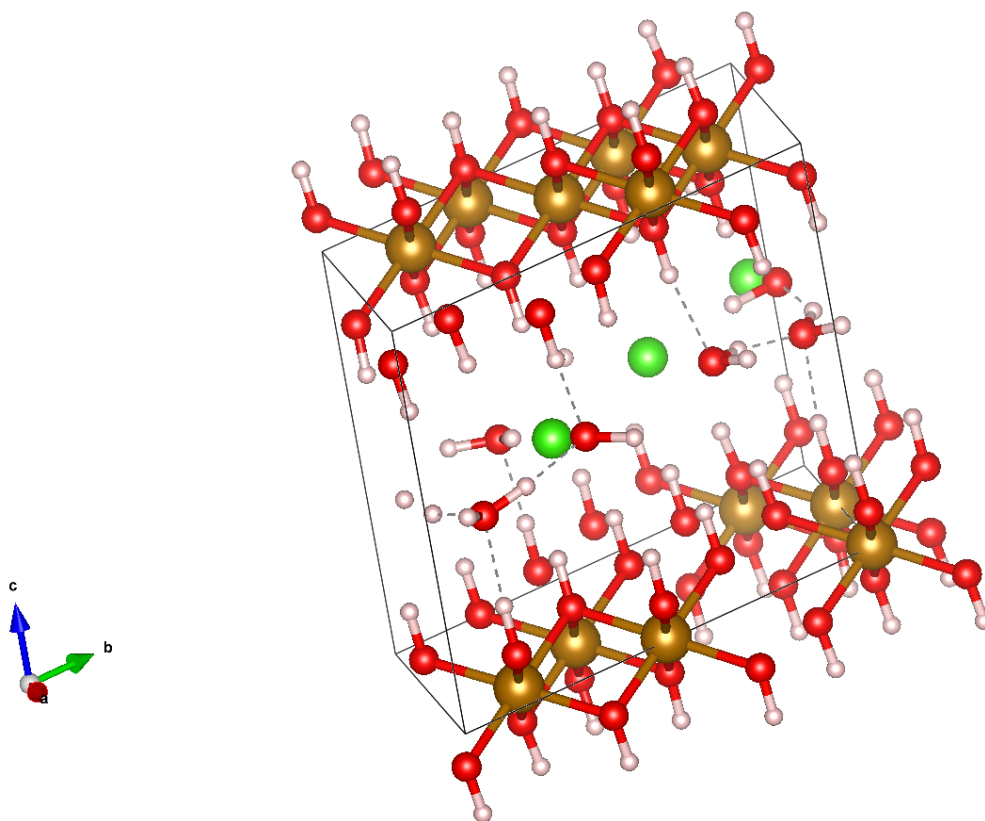


Figure 70: Crystal structure of Chloride GR1 from DFT, with 3 chloride ions and water added.

The three Cl^- ions again remained close to the centreline of the interlayer, with just one of them shifting to a fractional position of 0.49 (the other two remained on the centreline, with a fractional coordinate of 0.50). The position of the six water molecules changed, though in quite a uniform fashion; three moved slightly above the centreline of the interlayer and three moved slightly below (the range of the fractional coordinates was between 0.46 and 0.54). Each of the water molecule oxygen atoms formed a hydrogen bond to a hydrogen atom in the hydroxide layer. These hydrogen bonds can be seen in Figure 70, which also shows which side of the centreline each water molecule

shifted to. This hydrogen bonding would appear the most likely reason for the shifting of each water molecule from the centreline of the interlayer.

The orientation of the water molecules changed, producing a consistent arrangement with both H atoms shifted to the same side of the interlayer centreline as the O atom. However, each of the H atoms was pointing toward the centreline of the interlayer, relative to the O atom of the water molecule. The fractional coordinates of the H atoms ranged from 0.47 to 0.53, though each pair (associated with one water molecule) were always slightly different to each other in regard to this coordinate *i.e.* the orientation was never exactly planar in relation to the centreline plane of the interlayer. This would seem logical as the attractive charges between the O of each water molecule and the H of the hydroxide layer would also mean there would be a repulsive force between the H of the water molecules and the H of the hydroxide layer. There was also some hydrogen bonding between water molecules in the interlayer, which is shown in figure 70.

This cell was converted to rhombohedral using CRYSCON to allow the comparison to experimental cell parameters, as shown in Table 107.

Table 107: Chloride green rust DFT with water modelling results using PBE_pseudo_D potentials.

Results from	Cell dimensions (Å)			% difference to experiment			Cell angles (°)			% difference to experiment		
	a	b	c	a	b	c	α	β	γ	α	β	γ
Experiment ^[224]	3.19	3.19	2.39	-	-	-	90.00	90.00	120.00	-	-	-
PBE_pseudo_D	4.32	4.06	3.84	35.42	27.27	60.67	86.21	85.74	119.60	-4.21	-4.73	-0.33

Following the DFT modelling of chloride GR1 with water, the interatomic potential model with water was tested. The final coordinates of the DFT

structure were used as the basis for the potential model. The potential parameters used are shown in Tables 108 to 110.

Table 108: Partial charges (q_u) on ions used in the testing and interatomic potential modelling of chloride green rust with water ($\text{Fe}_4(\text{OH})_8 \text{Cl} \cdot 2 \text{H}_2\text{O}$)

Species	
Ion	Charge (e)
Iron (Fe)	1.3000
Hydroxide Oxygen (Oh)	-0.9500
Water Oxygen (Ow)	-0.820
Hydroxide Hydrogen (oH)	0.4250
Water Hydrogen (Hw)	0.410
Chlorine (Cl)	-1.0000

Table 109: Lennard-Jones potentials for chloride green rust ($\text{Fe}_4(\text{OH})_8 \text{Cl} \cdot 2 \text{H}_2\text{O}$), modified CLAYFF potentials

Lennard-Jones potentials $A_{ij}r_{ij}^{-12} - B_{ij}r_{ij}^{-6}$		
Ion pair (ij)	A_{ij} (eV \AA^{12})	B_{ij} (eV \AA^6)
Fe-Fe	304.642804	0.021844
Oh-Oh	27290.954820	27.122570
Ow-Ow	27290.954820	27.122570
Cl-Cl	914162.129100	125.986666
oH-oH	31.797010	2.183930
Hw-Hw	31.797010	2.183930
Fe-Oh	3836.983420	0.887919
Fe-Ow	3836.983420	0.887919
Fe-Cl	16987.462370	1.673741
Fe-oH	635.357101	0.554944
Fe-Hw	635.357101	0.554944
Cl-Oh	185709.578409	63.384691
Cl-Ow	185709.578409	63.384691
Cl-oH	25161.283311	35.834031
Cl-Hw	25161.283311	35.834031
Oh-Ow	27290.954820	27.122570
Oh-oH	1937.905220	11.100685
Oh-Hw	1937.905220	11.100685
Ow-oH	1937.905220	11.100685
Ow-Hw	1937.905220	11.100685
Hw-oH	31.797010	2.183930

Table 110: Harmonic potentials for chloride green rust ($\text{Fe}_4(\text{OH})_8 \text{Cl} \cdot 2 \text{H}_2\text{O}$), modified CLAYFF potentials

Harmonic potentials $k_{ij}/2(r_{ij} - r_0)^2$		
Species (ij)	k_{ij} (eV \AA^{-2})	r_0 (\AA) e
Oh-oH	48.059	1.000
Ow-Hw	48.059	1.000

Table 111: Three-body potentials for chloride green rust ($\text{Fe}_4(\text{OH})_8 \text{Cl} \cdot 2 \text{H}_2\text{O}$), modified CLAYFF potentials

Three-body potentials $k_{ijk}/2(\theta_{ijk} - \theta_0)^2$		
Species (ijk)	k_{ijk} (eV rad^{-2})	θ_0 (deg)
Hw-Ow-Hw	3.97	109.47

GULP was used to relax the structure at constant pressure and initial results were problematic. Some interactions between Cl and Fe appeared too strong and pulled both atoms out of position, one hydrogen atom dissociated from the relative hydroxide oxygen and the cell angles and dimensions became overly distorted. Optimising the cell at constant volume produced similar problems. An example of the H dissociation and Fe layer distortion can be seen in Figure 71.

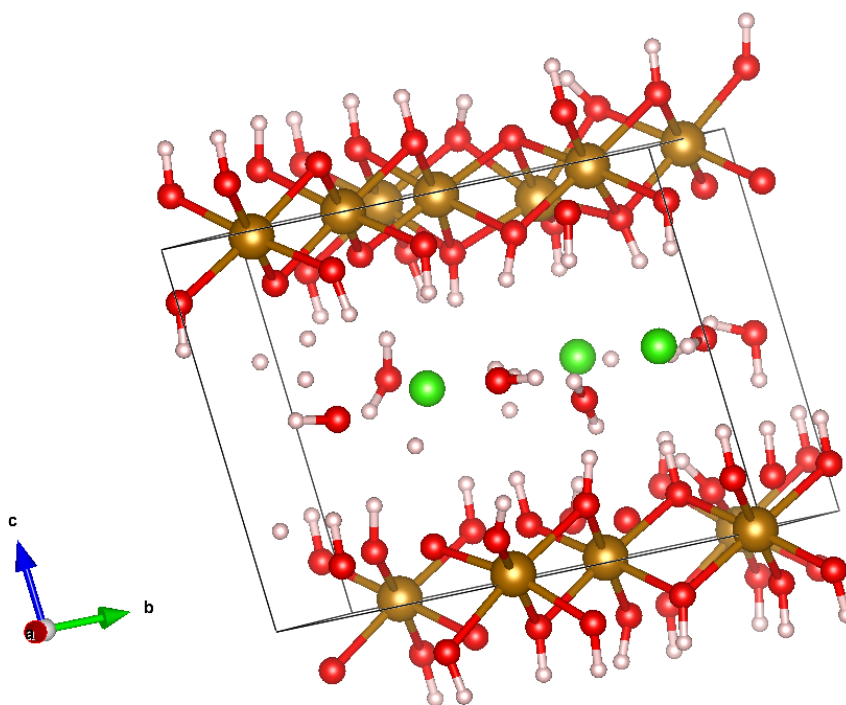


Figure 71: Crystal structure of Chloride GR1 with water, showing H dissociation and Fe layer distortion.

Fixing the a, b and c parameters of the cell whilst allowing the angles to change prevented the dissociation and distortion, as shown in Figure 72, but this was not a structure which had been fully relaxed.

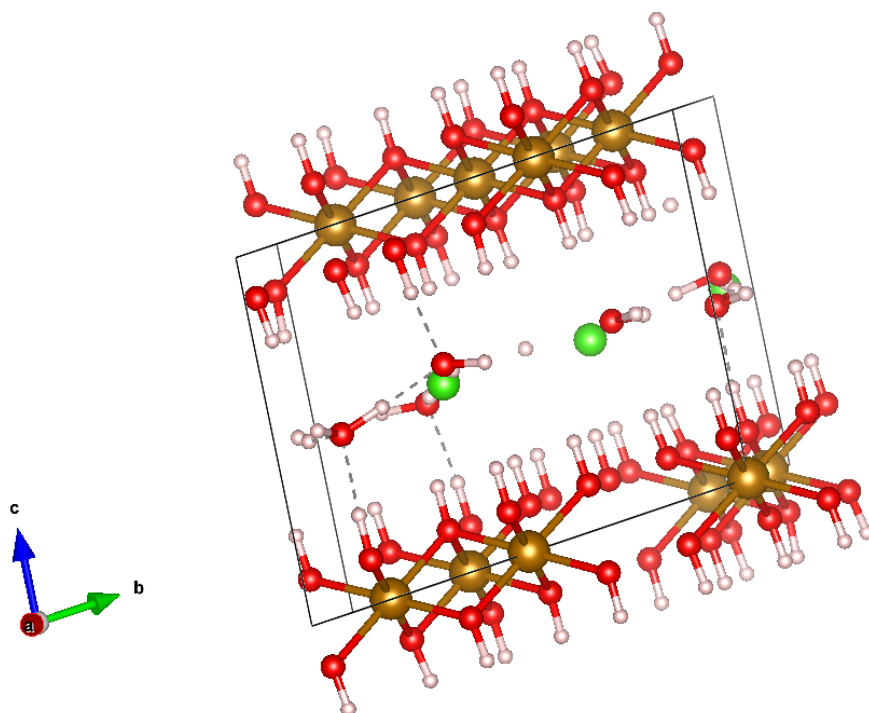


Figure 72: Crystal structure of Chloride GR1 with water, with fixed cell dimensions.

Because the potential model of chloride GR1 with water began with cell parameters from the DFT output, which had distorted already when compared to experimental measurements, it was decided to run the DFT calculations again but with constraints applied to fix certain aspects of cell geometry; this would provide alternative input cells to re-investigate the potential model. Two DFT inputs with fixed cell angles were prepared, one allowing a , b and c to relax independently and one allowing a , b and c to relax but with a equal to b .

At this point in the project the research time came to an end so further modelling could not be undertaken.

6.3 Conclusions

The work in this chapter set out to model green rust 1 and 2, using and developing the potentials already tested with iron hydroxide and goethite in chapter 4. DFT modelling was utilised for an additional comparison to experimental data.

A sulfate green rust was chosen to be modelled as an example of green rust 2; it was demonstrated that the potentials used could successfully model the bulk structure of GR2 (without water) and that the orientation of the sulfate molecules towards the hydroxide layer was most likely to be tridentate, with regard to the oxygen atoms of the sulfate group. Adding water to the model demonstrated that the potential model was able to produce a structure closer to experimentally determined measurements than was DFT, particularly with respect to the c parameter and also the α and γ angles. Cutting the bulk structure to model some of the low index surfaces of GR2 did not produce a viable representation of the $(0\ 1\ 0)$ surface, but was able to successfully model the $(1\ 0\ 0)$ and $(0\ 0\ 1)$ surfaces; the $(0\ 0\ 1)$ appeared to be the more stable of these two surfaces. The $(0\ 0\ 1)$ surface is parallel to the interlayers of sulfate green rust which could be expected to aid formation of the channels and assist absorption of the uranyl ion into the interlayer.

For a green rust 1 example the chloride was chosen. Modelling in DFT was able to produce a chloride GR1 structure without water and a structure with water added; conversion of the cell from hexagonal to rhombohedral allowed comparison with experimental results. The potential model without water presented problems when water was added to the cell; there was some

dissociation of the H atoms from the hydroxide layer and the Fe layer suffered some distortion. There were plans for refinement using alternative input cells and further investigation of the results from modelling these cells, but at this point the research time came to an end and the project had to be halted.

7 Conclusions

The work in this thesis has used a combination of electronic structure calculations and atomistic simulation using interatomic potentials. The aim was to develop interatomic potential models, which do not currently exist, for green rust and a range of uranyl minerals, to enable the study of interactions with uranyl ions at surfaces and interlayers of green rust. Furthering knowledge of such interactions will lead to a better understanding of the potential for green rusts to be used as remediation or long-term storage options with regard to uranyl ions, for example by reducing U(VI) to U(IV). It was intended that reliable, transferable potential models be developed so that they could additionally be used in alternative or further studies.

Chapter 4 focused on modelling $\text{Fe}(\text{OH})_2$ and goethite to test and refine the CLAYFF interatomic potential sets that would later be developed to model the more complex structure of green rust. These potential sets are required to model larger systems, which are beyond the reach of DFT calculation due to their computational expense. There are few experimentally reported structures for pure $\text{Fe}(\text{OH})_2$ but those documented were reproduced with excellent results using the potential model, with a, b and c parameters all within 0.7% of experimental results and the cell angles an exact match. Results from the DFT calculations, which used the PBE_pseudo_D potentials, were also very good, though they could not match experimental data quite as well as the potential model; cell dimensions were within 5% and cell angles within 0.1%. The CLAYFF potentials were demonstrated suitable for modelling the bulk structure of $\text{Fe}(\text{OH})_2$ so were then used to model five of

the low index Miller surfaces of the same compound. Following convergence testing for the slab thicknesses each surface was relaxed to the minimum energy state to allow the surface energy trends to be compared. The DFT results presented anomalies, perhaps due to the inability of DFT to account for van der Waals forces, but the potential sets tested all revealed the (0 0 1) surface to be the most stable, followed by the (0 1 0) and (0 1 1) surfaces which were closely matched. The (1 1 0) surface was found to be the least stable of those investigated using potentials. It was demonstrated that interatomic potentials can model the bulk of $\text{Fe}(\text{OH})_2$ with greater accuracy than DFT calculation, and that they can successfully model the low index Miller surfaces of $\text{Fe}(\text{OH})_2$. The results showed that existing CLAYFF potential sets can be used in this modelling; this is ideal for ease of mixing potentials later in the project, where uranyl compounds and green rust are investigated. The second part of chapter 4 involved further testing the potentials in the modelling of goethite, a mineral formed from green rust in an oxidising environment; the results were compared to experimental data and results from DFT calculations. The results confirmed that interatomic potentials based on the CLAYFF potential set were transferable to the modelling of the bulk and low index Miller surfaces of goethite. For the bulk structure of goethite the interatomic potential results again produced a closer match to experimental data than DFT was able to produce, with cell dimensions within around 1% of empirical measurements and cell angles an exact match. When viewed alongside the results from the modelling of $\text{Fe}(\text{OH})_2$ this demonstrated that the potential sets investigated show good interchangeability for use in the modelling of larger systems, such as green rust, and that complex fitting

procedures are not required.

Chapter 5 continued the development of interatomic potentials based on the CLAYFF potential set by developing potentials for a range of uranyl minerals, namely the chloride, carbonate, iron oxide, hydroxide and sulfate. Existing Lennard-Jones potentials were used where possible; if potentials were only available as Buckingham potentials these were initially recast as Lennard-Jones potentials to make mixing of potentials easier. If no existing potentials could be found for testing then they were created from other potentials using standard Lorentz-Berthelot mixing rules. These potentials were systematically adjusted and refined as required; if no acceptable result was attained using Lennard-Jones potentials then Buckingham potentials were used, mixed where necessary. Many of the compounds investigated had not been previously modelled in computational studies so the potential model results were compared to experimental data and to DFT calculation results; it was demonstrated that the potential sets showed good agreement with these results. This established further the viability of the potential sets used, to produce a general and interchangeable set of potentials which could be used in modelling larger mixed systems without the need for systematic fitting.

Chapter 6 focused on using the potentials developed in chapter 4 and chapter 5 to model the more complex structure of green rust, using a sulfate green rust and a chloride green rust as examples of a GR2 and GR1 structure respectively. DFT calculations were also run to provide an additional comparison to experimental data. It was demonstrated that the bulk structure of sulfate green rust 2, without water, could be successfully modelled. Some experimental studies concluded that the sulfate groups in the interlayer were

monodentate in their orientation towards the hydroxide layer, with regard to the oxygen atoms; the work in this study disagreed with those findings and found a tridentate orientation to be the more likely arrangement. Once water was added to the bulk structure the potential model produced cell parameters closer to experimental measurements than DFT could achieve. Modelling low index Miller surfaces of sulfate green rust produced successful models of the (1 0 0) and (0 0 1) surfaces, with the (0 0 1) surface the lowest in energy and therefore, of the surfaces modelled, the most stable and most likely surface to form. A chloride green rust was modelled, both with and without water, as an example of GR1. Conversion of the resultant cell to a rhombohedral structure allowed comparison with experimental data and showed that the cell without water could successfully be modelled using the potential sets developed. Addition of water to the cell caused some hydrogen atom dissociation from the hydroxide layers and some distortion in the Fe layer of the GR1 model, though the energy minimisation was successful which suggested refinement of the potentials may well produce a structure without such artefacts. The refinement of this structure and the investigation of alternative input cells was halted by the research time coming to an end.

The work in section 5.3 of chapter 5 investigated the use of molecular dynamics in modelling the aqueous uranyl ion. Two different potential sets were tested and their results evaluated. The potentials developed by Guilhaud and Wipff were demonstrated to be the better of those tested and produced satisfactory results when compared with experimental data. The possibilities for future development and refinement of these potentials were

identified and could form part of further study.

This work has investigated interatomic potential modelling of green rust systems which are too large and complex to be practically investigated using DFT calculations. The work has demonstrated that these potential models are effective and useful tools and has developed models of green rust systems not previously modelled using interatomic potentials. This work has been done by using and refining existing potential sets, which negates the need for expensive fitting procedures and greatly aids the mixing of potentials to form larger and more complex systems. Whilst effective potential models have been developed using partial charges on ions, it should be noted that no consistent pattern could be determined concerning the value of these charges in different systems. There are pitfalls in the process of fitting potentials when attempting to develop a potential model; it is a challenging process trying to fit to a range of properties that have either been calculated from a QM method or measured experimentally. There are parameter sets for a large number of materials in the scientific literature which can often be used as a starting point, though if these are transferred into a different system they may not work well without refinement. They may work for certain properties of a system but not for others, so could be described as partially transferable. To better fit the potentials to the system of interest may involve varying only the partial charges but, as in this work, may also require a systematic variation of the Lennard-Jones or Buckingham potential parameters. Even then, there may not be an easily attainable set of parameters to produce an effective potential model, such as with the chloride GR1 model at the point reached in this project. The fitting process in this work

focused primarily on reproducing the unit cell parameters a , b , c , α , β and γ ; additional considerations could be to fit other parameters such as thermal expansion, cohesion and elastic properties. The more parameters that are fitted, the more the likelihood that the potential model will be transferable, but the more complex the fitting process becomes. If it is not for a simple model, sophisticated optimisation or machine learning methods may be necessary to produce useful potentials.

The work in this thesis can be taken further by refining the potential sets to produce an acceptable bulk model of chloride GR1 and modelling the low index Miller surfaces of this structure. This would finalise the modelling of all the components of the green rust systems under investigation. The system could then be studied using molecular dynamics to determine the adsorption and absorption behaviour of the uranyl ion onto and into green rust, as a function of chemical conditions and concentration. Whilst the work in this project has focused on the development of potentials using rigid ion models, primarily for the simplicity of potential mixing and time constraints, it would be worthwhile developing shell models to investigate the effects of ionic polarisability on the interactions between species. The mechanical stability of the models could be investigated and compared to results from physical experiment and alternative models; this could involve properties such as the bulk modulus, Young's modulus and elastic constants of the system. Indeed in this project a good deal of work was undertaken in determining elastic constants from the DFT results for the uranyl minerals modelled in chapter 5, so that these could be compared with the results available from the potential models; however, this was a lengthy process and time constraints

prevented completion and inclusion in this thesis.

The relationship between structure and properties of uranyl based minerals, and thus the potential for the immobilisation of uranium, can be investigated using the methods described, and is an area with great potential for contribution to knowledge.

References

- [1] L. W. Shemilt and G. Sheng, *Energy Exploration & Exploitation*, 1983, **2**, 41–56.
- [2] D. Bodansky, *Physics Today*, 2006, **59**, 80–81.
- [3] D. Lochbaum, *Bulletin of the Atomic Scientists*, 2014, **70**, 26–36.
- [4] D. Hambley, *EPJ Nuclear Sciences & Technologies*, 2016, **2**, 21.
- [5] J. Cruickshank, *The Sellafield Contaminated Land and Groundwater Management Project: Characterisation of a Complex Nuclear Facility*, Nuclear energy agency of the oecd (nea) technical report, 2012.
- [6] Nuclear Decommissioning Authority, *Magnox Fuel Strategy Position Paper*, Nuclear decommissioning authority technical report, 2012.
- [7] N. C. Hyatt, *Energy Policy*, 2017, **101**, 303–309.
- [8] H. McKenzie, D. Coughlin, F. Laws and A. Stamper, *Groundwater Monitoring at Sellafield Annual Data Review 2011*, Sellafield ltd technical report, 2011.
- [9] A. Bleise, P. R. Danesi and W. Burkart, *Journal of Environmental Radioactivity*, 2003, **64**, 93–112.
- [10] J. L. Domingo, *Reproductive and developmental toxicity of natural and depleted uranium: A review*, 2001.
- [11] K. B. Gongalsky, *Environmental Monitoring and Assessment*, 2003, **89**, 197–219.

- [12] A. S. Paschoa and F. Steinhäusler, in *Radioactivity in the Environment*, Elsevier, 2010, vol. 17, pp. 29–85.
- [13] J. Li and Y. Zhang, *Procedia Environmental Sciences*, 2012, **13**, 1609–1615.
- [14] C. Noubactep, G. Meinrath and B. J. Merkel, *Environmental Chemistry*, 2005, **2**, 235.
- [15] S. Dushenkov, *Plant and Soil*, 2003, pp. 167–175.
- [16] M. Kalin, W. N. Wheeler and G. Meinrath, *Journal of Environmental Radioactivity*, 2005, **78**, 151–177.
- [17] F. Malekzadeh, A. Farazmand, H. Ghafourian, M. Shahamat, M. Levin and R. R. Colwell, *World Journal of Microbiology and Biotechnology*, 2002, pp. 295–302.
- [18] J. Yao, Y. Ma and H. He, *Environment of Sichuan*, 2010, **29**, 48–51.
- [19] S. Dushenkov, D. Vasudev, Y. Kapulnik, D. Gleba, D. Fleisher, K. C. Ting and B. Ensley, *Environmental Science and Technology*, 1997, **31**, 3468–3474.
- [20] J. Pratas, N. Rodrigues and C. Paulo, *Uranium in the Environment: Mining Impact and Consequences*, 2006, pp. 477–482.
- [21] P. Chang, K.-W. Kim, S. Yoshida and S.-Y. Kim, *Environmental Geochemistry and Health*, 2005, **27**, 529–538.

- [22] H. Shahandeh and L. R. Hossner, *Water, Air, and Soil Pollution*, 2002, **141**, 165–180.
- [23] J. W. Huang, M. J. Blaylock, Y. Kapulnik and B. D. Ensley, *Environmental Science and Technology*, 1998, **32**, 2004–2008.
- [24] L. Tang, Y. Bai and C. Deng, *Nuclear Technology*, 2009, **32**, 136–140.
- [25] Q. Y. Zhou, K. X. Tan and S. Zeng, *Atomic Energy Science & Energy*, 2009, **43**, 808–812.
- [26] Z. J. Tang, P. Zhang and S. Zuo, *Industry water and waste*, 2003, **4**, 9–12.
- [27] C. M. Chen, G. M. Zeng and C. Tang, *Metal Mine*, 2009, **5**, 135–137.
- [28] R. K. Allada, A. Navrotsky, H. T. Berbeco and W. H. Casey, *Science*, 2002, **296**, 721–723.
- [29] D. Sparks, *Environmental Soil Chemistry*, Academic Press, 2nd edn., 2003.
- [30] F. Trolard and G. Bourrié, *Chapter 5 Geochemistry of Green Rusts and Fougérite. A Reevaluation of Fe cycle in Soils*, 2008.
- [31] C. Ruby, M. Usman, S. Naille, K. Hanna, C. Carteret, M. Mullet, M. François and M. Abdelmoula, *Applied Clay Science*, 2010, **48**, 195–202.
- [32] K. Hosni and E. Srasra, *Applied Clay Science*, 2009, **43**, 415–419.
- [33] Q. Wang and D. O’Hare, *Chemical Reviews*, 2012, **112**, 4124–4155.

- [34] W. Lv, Q. Mei, H. Fu, J. Xiao, M. Du and Q. Zheng, *Journal of Materials Chemistry A*, 2017, **5**, 19079–19090.
- [35] C. Nyambo, P. Songtipya, E. Manias, M. M. Jimenez-Gasco and C. A. Wilkie, *Journal of Materials Chemistry*, 2008, **18**, 4827–4838.
- [36] C. Manzi-Nshuti, J. M. Hossenlopp and C. A. Wilkie, *Polymer Degradation and Stability*, 2009, **94**, 782–788.
- [37] J. Plank, D. Zhimin, H. Keller, F. v. Hössle and W. Seidl, *Cement and Concrete Research*, 2010, **40**, 45–57.
- [38] A. C. Alcântara, P. Aranda, M. Darder and E. Ruiz-Hitzky, *Journal of Materials Chemistry*, 2010, **20**, 9495–9504.
- [39] F. Millange, R. I. Walton, L. Lei and D. O’Hare, *Chemistry of Materials*, 2000, **12**, 1990–1994.
- [40] I. C. Chisem and W. Jones, *Journal of Materials Chemistry*, 1994, **4**, 1737–1744.
- [41] A. M. Fogg, J. S. Dunn, S. G. Shyu, D. R. Cary and D. O’Hare, *Chemistry of Materials*, 1998, **10**, 351–355.
- [42] F. Leroux and J. Besse, *Chemistry of Materials*, 2001, **13**, 3507–3515.
- [43] X. Xu, R. Lu, X. Zhao, S. Xu, X. Lei, F. Zhang and D. G. Evans, *Applied Catalysis B: Environmental*, 2011, **102**, 147–156.
- [44] Q. Wang, J. Luo, Z. Zhong and A. Borgna, *Energy and Environmental Science*, 2011, **4**, 42–55.

- [45] Q. Wang, Z. Wu, H. H. Tay, L. Chen, Y. Liu, J. Chang, Z. Zhong, J. Luo and A. Borgna, *Catalysis Today*, 2011, pp. 198–203.
- [46] Q. Wang, H. H. Tay, Z. Guo, L. Chen, Y. Liu, J. Chang, Z. Zhong, J. Luo and A. Borgna, *Applied Clay Science*, 2012, **55**, 18–26.
- [47] Q. Wang, H. H. Tay, D. J. W. Ng, L. Chen, Y. Liu, J. Chang, Z. Zhong, J. Luo and A. Borgna, *ChemSusChem*, 2010, **3**, 965–973.
- [48] Q. Wang, H. H. Tay, L. Chen, Y. Liu, J. Chang, Z. Zhong, J. Luo and A. Borgna, *Journal of Nanoengineering and Nanomanufacturing*, 2012, **1**, 298–303.
- [49] J. M. R. Genin and C. Ruby, *Solid State Sciences*, 2004, **6**, 705–718.
- [50] L. H. G. Chaves, *Revista Brasileira de Engenharia Agrícola e Ambiental*, 2005, **9**, 284–288.
- [51] R. T. Cygan, J.-J. Liang and A. G. Kalinichev, *Journal of Physical Chemistry B*, 2004, **108**, 1255–1266.
- [52] M. C. Payne, M. P. Teter, D. C. Allan, T. A. Arias and J. D. Joannopoulos, *Reviews of Modern Physics*, 1992, **64**, 1045–1097.
- [53] B. Christiansen, H. Geckeis, C. Marquardt, A. Bauer, J. Römer, T. Wiss, D. Schild and S. Stipp, *Geochimica et Cosmochimica Acta*, 2011, **75**, 1216–1226.
- [54] M. S. Kim, T. H. Kim, Y. S. Seo, J. M. Oh and J. K. Park, *Dalton Transactions*, 2017, **46**, 7656–7659.

- [55] M. Usman, J. M. Byrne, A. Chaudhary, S. Orsetti, K. Hanna, C. Ruby, A. Kappler and S. B. Haderlein, *Magnetite and Green Rust: Synthesis, Properties, and Environmental Applications of Mixed-Valent Iron Minerals*, 2018.
- [56] J. K. Fredrickson, J. M. Zachara, D. W. Kennedy, H. Dong, T. C. Onstott, N. W. Hinman and S. M. Li, *Geochimica et Cosmochimica Acta*, 1998, **62**, 3239–3257.
- [57] J. M. Génin, A. A. Olowe, B. Resiak, M. Confente, N. Rollet-Benbouzid, S. L’Haridon and D. Prieur, *Hyperfine Interactions*, 1994, **93**, 1807–1812.
- [58] A. Géhin, C. Ruby, M. Abdelmoula, O. Benali, J. Ghanbaja, P. Refait and J. M. R. Génin, *Solid State Sciences*, 2002, **4**, 61–66.
- [59] S. Loyaux-Lawniczak, P. Refait, J.-J. Ehrhardt and P. Lecomte, *Environmental Science & Technology*, 1999, **34**, 438–443.
- [60] S. Drissi, P. Refait, M. Abdelmoula and J. Génin, *Corrosion Science*, 1995, **37**, 2025–2041.
- [61] J. M. R. Génin, C. Ruby and C. Upadhyay, *Solid State Sciences*, 2006, **8**, 1330–1343.
- [62] C. Helling, O. Nitzsche, B. Ullrich and B. Merkel, *Mine Water and the Environment*, 1998, **17**, 41–51.
- [63] H. C. B. Hansen, O. K. Borggaard and J. Sorensen, *Geochimica et Cosmochimica Acta*, 1994, **58**, 2599–2608.

- [64] S. C. Myneni, *Science*, 1997, **278**, 1106–1109.
- [65] A. Sumoondur, S. Shaw, I. Ahmed and L. G. Benning, *Mineralogical Magazine*, 2008, **72**, 201–204.
- [66] W. L. Jorgensen, J. Chandrasekhar, J. D. Madura, R. W. Impey and M. L. Klein, *The Journal of Chemical Physics*, 1983, **79**, 926–935.
- [67] D. J. Cooke, S. E. Redfern and S. C. Parker, *Physics and Chemistry of Minerals*, 2004, **31**, 507–517.
- [68] A. Chroneos, K. Desai, S. E. Redfern, M. O. Zacate and R. W. Grimes, *Journal of Materials Science*, 2006, **41**, 675–687.
- [69] A. Chroneos, N. J. Ashley, K. H. Desai, J. F. Maguire and R. W. Grimes, *Journal of Materials Science*, 2007, **42**, 2024–2029.
- [70] S. Kerisit, D. J. Cooke, A. Marmier and S. C. Parker, *Chemical Communications*, 2005, **0**, 3027.
- [71] D. Spagnoli, D. J. Cooke, S. Kerisit and S. C. Parker, *Journal of Materials Chemistry*, 2006, **16**, 1997.
- [72] M. Born and K. Huang, *Dynamical theory of crystal lattices*, Clarendon Press, 1988, p. 420.
- [73] N. H. de Leeuw and T. G. Cooper, *Geochimica et Cosmochimica Acta*, 2007, **71**, 1655–1673.
- [74] B. G. Dick and A. W. Overhauser, *Physical Review*, 1958, **112**, 90–103.

- [75] W. Mackrodt, *Philosophical Transactions of the Royal Society of London. Series A: Physical and Engineering Sciences*, 1992, **341**, 301–312.
- [76] V. Coustet and J. Jupille, *Surface and Interface Analysis*, 1994, **22**, 280–283.
- [77] T. J. Godin and J. P. Lafemina, *Physical Review B*, 1994, **49**, 7691–7696.
- [78] I. Manassidis and M. J. Gillan, *Journal of the American Ceramic Society*, 1994, **77**, 335–338.
- [79] M. A. Nygren, D. H. Gay and C. R. Catlow, *Surface Science*, 1997, **380**, 113–123.
- [80] A. M. Smith, K. A. Hudson-Edwards, W. E. Dubbin and K. Wright, *Geochimica et Cosmochimica Acta*, 2006, **70**, 608–621.
- [81] M. C. Wander, K. M. Rosso and M. A. Schoonen, *Journal of Physical Chemistry C*, 2007, **111**, 11414–11423.
- [82] A. Vakis, V. Yastrebov, J. Scheibert, L. Nicola, D. Dini, C. Minfray, A. Almqvist, M. Paggi, S. Lee, G. Limbert, J. Molinari, G. Ancaux, R. Aghababaei, S. Echeverri Restrepo, A. Papangelo, A. Cammarata, P. Nicolini, C. Putignano, G. Carbone, S. Stupkiewicz, J. Lengiewicz, G. Costagliola, F. Bosia, R. Guarino, N. Pugno, M. Müser and M. Ciavarella, *Tribology International*, 2018, **125**, 169–199.
- [83] *Periodic Boundary Conditions*, <http://isaacs.sourceforge.net/phys/psc.html>.

- [84] G. W. Watson, E. T. Kelsey, N. H. de Leeuw, D. J. Harris, S. C. Parker and G. Thornton, *Journal of the Chemical Society, Faraday Transactions*, 1996, **92**, 433.
- [85] M. Born and R. Oppenheimer, *Annalen der Physik*, 1927, **389**, 457–484.
- [86] S. J. Clark, M. D. Segall, C. J. Pickard, P. J. Hasnip, M. I. J. Probert, K. Refson and M. C. Payne, *Zeitschrift für Kristallographie - Crystalline Materials*, 2005, **220**, 567–570.
- [87] M. E. Foster and K. Sohlberg, *Physical Chemistry Chemical Physics*, 2010, **12**, 307–322.
- [88] V. Fock, *Zeitschrift für Physik*, 1930, **61**, 126–148.
- [89] P. Hohenberg and W. Kohn, *Physical Review*, 1964, **136**, B864–B871.
- [90] W. Kohn and L. J. Sham, *Physical Review*, 1965, **140**, A1133.
- [91] J. G. Lee, *Computational materials science : an introduction*, CRC Press, 2nd edn., 2016.
- [92] J. P. Perdew, K. Burke and M. Ernzerhof, *Physical Review Letters*, 1996, **77**, 3865–3868.
- [93] J. P. Perdew, J. A. Chevary, S. H. Vosko, K. A. Jackson, M. R. Peder-son, D. J. Singh and C. Fiolhais, *Physical Review B*, 1992, **46**, 6671–6687.

- [94] L. He, F. Liu, G. Hautier, M. J. Oliveira, M. A. Marques, F. D. Vila, J. J. Rehr, G. M. Rignanese and A. Zhou, *Physical Review B - Condensed Matter and Materials Physics*, 2014, **89**, 064305.
- [95] J. P. Perdew, A. Ruzsinszky, G. I. Csonka, O. A. Vydrov, G. E. Scuseria, L. A. Constantin, X. Zhou and K. Burke, *Physical Review Letters*, 2008, **100**, 136406.
- [96] Z. Wu and R. E. Cohen, *Physical Review B - Condensed Matter and Materials Physics*, 2006, **73**, 235116.
- [97] P. Haas, F. Tran and P. Blaha, *Physical Review B - Condensed Matter and Materials Physics*, 2009, **79**, 085104.
- [98] P. F. Weck, E. Kim, J. A. Greathouse, M. E. Gordon and C. R. Bryan, *Chemical Physics Letters*, 2018, **698**, 195–199.
- [99] S. Grimme, *Journal of Computational Chemistry*, 2004, **25**, 1463–1473.
- [100] S. Grimme, *Journal of Computational Chemistry*, 2006, **27**, 1787–1799.
- [101] S. Grimme, A. Hansen, J. G. Brandenburg and C. Bannwarth, *Chemical Reviews*, 2016, **116**, 5105–5154.
- [102] F. Bloch and Felix, *Zeitschrift fur Physik*, 1929, **52**, 555–600.
- [103] H. J. Monkhorst and J. D. Pack, *Physical Review B*, 1976, **13**, 5188–5192.
- [104] M. D. Segall, P. J. Lindan, M. J. Probert, C. J. Pickard, P. J. Hasnip,

- S. J. Clark and M. C. Payne, *Journal of Physics Condensed Matter*, 2002, **14**, 2717–2744.
- [105] C. R. Catlow, K. M. Diller and M. J. Norgett, *Journal of Physics C: Solid State Physics*, 1977, **10**, 1395.
- [106] G. V. Lewis and C. R. A. Catlow, *Journal of Physics C: Solid State Physics*, 1985, **18**, 1149–1161.
- [107] D. Cheshmedzhieva, S. Ilieva, B. Hadjieva and B. Galabov, *Journal of Physical Organic Chemistry*, 2021, **34**, e4258.
- [108] H. T. Ta, A. K. Tieu, H. Zhu, H. Yu, T. D. Ta, S. Wan, N. V. Tran and H. M. Le, *Journal of Physical Chemistry C*, 2018, **122**, 635–647.
- [109] M. Zhou and G. Frenking, *Accounts of Chemical Research*, 2021, **54**, 3071–3082.
- [110] B. Wang, S. L. Li and D. G. Truhlar, *Journal of Chemical Theory and Computation*, 2014, **10**, 5640–5650.
- [111] M. Schauperl, P. S. Nerenberg, H. Jang, L. P. Wang, C. I. Bayly, D. L. Mobley and M. K. Gilson, *Communications Chemistry 2020 3:1*, 2020, **3**, 1–11.
- [112] M. I. Chaudhari, J. R. Nair, L. R. Pratt, F. A. Soto, P. B. Balbuena and S. B. Rempe, *Journal of Chemical Theory and Computation*, 2016, **12**, 5709–5718.
- [113] P. P. Ewald, *Annalen der Physik*, 1921, **369**, 253–287.

- [114] B. J. Alder and T. E. Wainwright, *The Journal of Chemical Physics*, 1957, **27**, 1208–1209.
- [115] B. J. Alder and T. E. Wainwright, *The Journal of Chemical Physics*, 1959, **31**, 459–466.
- [116] P. W. Tasker, *A Guide to MIDAS, AERE Report No. R9130*, Aere technical report, 1978.
- [117] T. E. Ferrin, C. C. Huang, L. E. Jarvis and R. Langridge, *Journal of Molecular Graphics*, 1988, **6**, 13–27.
- [118] D. Frenkel and B. Smit, *Understanding molecular simulation : from algorithms to applications*, Academic Press, 2002, p. 638.
- [119] D. Parry, *Surface Science*, 1976, **54**, 195.
- [120] D. Parry, *Surface Science*, 1975, **49**, 433–440.
- [121] D. M. Heyes, M. Barber and J. H. Clarke, *Journal of the Chemical Society, Faraday Transactions 2: Molecular and Chemical Physics*, 1977, **73**, 1485–1496.
- [122] J. E. Jones, *Proceedings of the Royal Society A: Mathematical, Physical and Engineering Sciences*, 1924, **106**, 463–477.
- [123] R. A. Buckingham, *Proceedings of the Royal Society A: Mathematical, Physical and Engineering Sciences*, 1938, **168**, 264–283.
- [124] B. Widom, *Statistical Mechanics*, Cambridge University Press, 2002.

- [125] D. A. D. A. McQuarrie, *Statistical mechanics*, Harper & Row, New York, 1975, p. 641.
- [126] G. W. Watson, S. C. Parker and A. Wall, *Journal of Physics: Condensed Matter*, 1992, **4**, 2097–2108.
- [127] N. L. Allan, A. L. Rohl, D. H. Gay, C. R. A. Catlow, R. J. Davey and W. C. MacKrodt, *Faraday Discussions*, 1993, **95**, 273–280.
- [128] P. M. Oliver, S. C. Parker, J. Purton and D. W. Bullett, *Surface Science*, 1994, **307-309**, 1200–1205.
- [129] G. V. Paolini, P. J. D. Lindan and J. H. Harding, *The Journal of Chemical Physics*, 1997, **106**, 3681–3687.
- [130] D. C. Sayle, S. A. Maicaneanu and G. W. Watson, *Physical Chemistry Chemical Physics*, 2002, **4**, 5189–5198.
- [131] R. Takagi, F. Hutchinson, P. A. Madden, A. K. Adya and M. Gaunescard, *Journal of Physics: Condensed Matter*, 1999, **11**, 645–658.
- [132] J. D. Gale, *Journal of the Chemical Society, Faraday Transactions*, 1997, **93**, 629–637.
- [133] I. T. Todorov, W. Smith, K. Trachenko, M. T. Dove, W. Smith, M. Pruneda and E. Artacho, *Journal of Materials Chemistry*, 2006, **16**, 1911.
- [134] P. Debye, *Mathematische Annalen*, 1909, **67**, 535–558.

- [135] J.-L. Chabert and E. E. Barbin, *A history of algorithms : from the pebble to the microchip*, Springer, 1999, p. 524.
- [136] R. Fletcher and M. J. D. Powell, *The Computer Journal*, 1963, **6**, 163–168.
- [137] C. G. Broyden, *IMA Journal of Applied Mathematics*, 1970, **6**, 76–90.
- [138] F. H. Stillinger and A. Rahman, *The Journal of Chemical Physics*, 1974, **61**, 4973–4980.
- [139] L. Verlet, *Physical Review*, 1967, **159**, 98–103.
- [140] R. W. Hockney, in *Methods in Computational Physics*, ed. B. Alder, S. Fernbach and M. Rotenberg, Academic Press Inc., New York, Volume 9 edn., 1970, ch. Plasma Phy, pp. 134–210.
- [141] C. K. Birdsall and A. B. Langdon, *Plasma physics via computer simulation*, Taylor & Francis, 2005, p. 479.
- [142] *Leapfrog integration*, <http://cvarin.github.io/CSci-Survival-Guide/leapfrog.html>.
- [143] P. Ehrenfest, *Zeitschrift für Physik*, 1927, **45**, 455–457.
- [144] L. Boltzmann, *Über die mechanische Bedeutung des zweiten Hauptsatzes der Wärmetheorie*, Wiener Berichte, 1866.
- [145] M. P. Allen and D. J. Tildesley, *Computer simulation of liquids*, Oxford University Press, 2nd edn., 2017.
- [146] W. G. Hoover, *Physical Review A*, 1985, **31**, 1695–1697.

- [147] S. Melchionna, G. Ciccotti and B. L. Holian, *Molecular Physics*, 1993, **78**, 533–544.
- [148] *Dictionary of Gems and Gemology*, ed. M.-D. M, Springer Berlin Heidelberg, 2009, pp. 572–573.
- [149] F. Bertaut, *Compt. Rendu.*, 1958, **246**, 3447.
- [150] P. W. Tasker, *Journal of Physics C: Solid State Physics*, 1979, **12**, 4977–4984.
- [151] H. F. Wardenga and A. Klein, *Applied Surface Science*, 2016, **377**, 1–8.
- [152] R. Plass, J. Feller and M. Gajdardziska-Josifovska, *Surface Science*, 1998, **414**, 26–37.
- [153] P. M. Oliver, S. C. Parker and W. C. Mackrodt, *Modelling and Simulation in Materials Science and Engineering*, 1993, **1**, 755.
- [154] N. H. De Leeuw, *Computer simulations of surfaces and interfaces: a case study of the hydration and dissolution of α -quartz SiO_2* , University college london technical report, 2006.
- [155] V. Fiorentini and M. Methfessel, *Journal of Physics: Condensed Matter*, 1996, **8**, 6525–6529.
- [156] R. H. P. Devamani and M. Alagar, *Elixir NanoTechnology*, 2013, **1**, 16845–16848.
- [157] M. F. Parveen, S. Umapathy, V. Dhanalakshmi and R. Anbarasan, *Journal of Applied Polymer Science*, 2010, **118**, 1728–1737.

- [158] F. L. Theiss, G. A. Ayoko and R. L. Frost, *Applied Surface Science*, 2016, **383**, 200–213.
- [159] M. Molano-Mendoza, D. Donneys-Victoria, N. Marriaga-Cabrales, M. A. Mueses, G. Li Puma and F. Machuca-Martínez, *MethodsX*, 2018, **5**, 915–923.
- [160] R. M. Cornell, U. Schwertmann and John Wiley & Sons., *The iron oxides : structure, properties, reactions, occurrences, and uses*, Wiley-VCH, 2003, p. 664.
- [161] R. W. G. Wyckoff, *Crystal Structures I*, Interscience Publishers, 2nd edn., 1963, p. 263.
- [162] J. D. Bernal, D. R. Dasgupta and A. L. Mackay, *Clay Minerals*, 1959, **4**, 15–30.
- [163] P. S. Baram and S. C. Parker, *Philosophical Magazine B*, 1996, **73**, 49–58.
- [164] S. Kerisit, D. J. Cooke, D. Spagnoli and S. C. Parker, *Journal of Materials Chemistry*, 2005, **15**, 1454.
- [165] J. F. W. Bowles, *Encyclopedia of Geology (Second Edition). Oxides*, Academic Press, 2021, pp. 428–441.
- [166] J. W. Anthony, R. A. Bideaux, K. W. Bladh and M. C. Nichols, *Handbook of Mineralogy: Halides, Hydroxides, Oxides*, Mineral Data Publishing, 1997, pp. 2001–2001.

- [167] L. Legrand, L. Mazerolles and A. Chaussé, *Geochimica et Cosmochimica Acta*, 2004, **68**, 3497–3507.
- [168] T. Nagai, H. Kagi and T. Yamanaka, *American Mineralogist*, 2003, **88**, 1423–1427.
- [169] S. Fernando, M. Baynes, B. Chen, J. F. Banfield and H. Zhang, *RSC Advances*, 2012, **2**, 6768–6772.
- [170] A. E. Gleason, R. Jeanloz and M. Kunz, *American Mineralogist*, 2008, **93**, 1882–1885.
- [171] E. Zepeda-Alarcon, H. Nakotte, A. F. Gualtieri, G. King, K. Page, S. C. Vogel, H.-W. Wang and H.-R. Wenk, *Journal of Applied Crystallography*, 2014, **47**, 1983–1991.
- [172] C. Klein, C. S. C. S. Hurlbut and J. D. Dana, *Manual of Mineralogy*, J. Wiley, 1999, p. 681.
- [173] J. Rakovan, U. Becker and M. F. Hochella, *American Mineralogist*, 1999, **84**, 884–894.
- [174] G. J. Martin, R. S. Cutting, D. J. Vaughan and M. C. Warren, *American Mineralogist*, 2009, **94**, 1341–1350.
- [175] J. D. Kubicki, K. W. Paul and D. L. Sparks, *Geochemical Transactions*, 2008, **9**, 1–16.
- [176] L. Zhou, F. Xiu, M. Qiu, S. Xia and L. Yu, *Applied Surface Science*, 2017, **392**, 760–767.

- [177] J. D. Gale, *Philosophical Magazine B*, 1996, **73**, 3–19.
- [178] M. S. Read and R. A. Jackson, *Journal of Nuclear Materials*, 2010, **406**, 293–303.
- [179] R. Salomon-Ferrer, D. A. Case and R. C. Walker, *Wiley Interdisciplinary Reviews: Computational Molecular Science*, 2013, **3**, 198–210.
- [180] D. A. Case, T. E. Cheatham, T. Darden, H. Gohlke, R. Luo, K. M. Merz, A. Onufriev, C. Simmerling, B. Wang and R. J. Woods, *Journal of computational chemistry*, 2005, **26**, 1668–1688.
- [181] B. R. Brooks, C. L. Brooks, A. D. Mackerell, L. Nilsson, R. J. Petrella, B. Roux, Y. Won, G. Archontis, C. Bartels, S. Boresch, A. Caffisch, L. Caves, Q. Cui, A. R. Dinner, M. Feig, S. Fischer, J. Gao, M. Hodoscek, W. Im, K. Kuczera, T. Lazaridis, J. Ma, V. Ovchinnikov, E. Paci, R. W. Pastor, C. B. Post, J. Z. Pu, M. Schaefer, B. Tidor, R. M. Venable, H. L. Woodcock, X. Wu, W. Yang, D. M. York and M. Karplus, *Journal of Computational Chemistry*, 2009, **30**, 1545–1614.
- [182] C. L. Kong, *The Journal of Chemical Physics*, 2003, **59**, 2464.
- [183] K.-P. Schröder, J. Sauer, M. Leslie, C. Richard, A. Catlow and J. M. Thomas, *Chemical Physics Letters*, 1992, **188**, 320–325.
- [184] C. L. Freeman, J. H. Harding, D. J. Cooke, J. A. Elliott, J. S. Lardge and D. M. Duffy, *Journal of Physical Chemistry C*, 2007, **111**, 11943–11951.

- [185] *ICSD Inorganic Crystal Structural Database*, <http://icsd.cds.rsc.org1>.
- [186] A. F. Gehlen, *Neues allgemeines Journal der Chemie*, Frolich, 1804.
- [187] Finch, M. Cooper, F. Hawthorne and R. Ewing, *Canadian Mineralogist*, 1999, **37**, 929–938.
- [188] E. Bacmann, M.; Bertaut, *Bulletin de la Societe Francaise de Mineralogie et de Cristallographie*, 1967, **90**, 257–258.
- [189] H. Taylor, J.C.; Hurst, *Acta Crystallographica B*, 0, **24,38,27**, 2018–2022.
- [190] J. D. Gale, *Journal of Physical Chemistry B*, 1998, **102**, 5423–5431.
- [191] J. C. Taylor, P. W. Wilson and IUCr, *Acta Crystallographica Section B Structural Crystallography and Crystal Chemistry*, 1973, **29**, 1073–1076.
- [192] P. Guilbaud and G. Wipff, *Journal of Molecular Structure: THEOCHEM*, 1996, **366**, 55–63.
- [193] T. L. Gilbert, *The Journal of Chemical Physics*, 1968, **49**, 2640–2642.
- [194] S. Kerisit and C. Liu, *Environmental Science & Technology*, 2014, **48**, 3899–3907.
- [195] S. Kerisit, A. R. Felmy and E. S. Ilton, *Environmental Science & Technology*, 2011, **45**, 2770–2776.
- [196] S. Kerisit and S. C. Parker, *Chemical Communications*, 2004, **4**, 52–53.

- [197] S. Fleming, A. Rohl, M.-Y. Lee, J. Gale and G. Parkinson, *Journal of Crystal Growth*, 2000, **209**, 159–166.
- [198] N. P. Brandenburg, B. O. Loopstra and IUCr, *Acta Crystallographica Section B Structural Crystallography and Crystal Chemistry*, 1978, **34**, 3734–3736.
- [199] C. D. Williams, N. A. Burton, K. P. Travis and J. H. Harding, *Journal of Chemical Theory and Computation*, 2014, **10**, 3345–3353.
- [200] W. R. Cannon, B. M. Pettitt and J. A. McCammon, *The Journal of Physical Chemistry*, 1994, **98**, 6225–6230.
- [201] M. Åberg, D. Ferri, J. Glaser and I. Grenthe, *Inorganic Chemistry*, 1983, **22**, 3986–3989.
- [202] R. D. Rogers, L. K. Kurihara and M. M. Benning, *Journal of Inclusion Phenomena*, 1987, **5**, 645–658.
- [203] N. W. Alcock and S. Esperås, *Journal of the Chemical Society, Dalton Transactions*, 1977, 893–896.
- [204] S. Pérez-Conesa, F. Torrico, J. M. Martínez, R. R. Pappalardo and E. Sánchez Marcos, *The Journal of Chemical Physics*, 2016, **145**, 224502.
- [205] P. Guilbaud and G. Wipff, *The Journal of Physical Chemistry*, 1993, **97**, 5685–5692.
- [206] J. S. Craw, M. A. Vincent, I. H. Hillier and A. L. Wallwork, *The Journal of Physical Chemistry*, 1995, **99**, 10181–10185.

- [207] S. Kerisit and S. C. Parker, *Journal of the American Chemical Society*, 2004, **126**, 10152–10161.
- [208] T. L. Hill, *Statistical Mechanics: Principles and Selected Applications*, McGraw-Hill, New York, 1956.
- [209] N. Rai, S. P. Tiwari and E. J. Maginn, *The Journal of Physical Chemistry B*, 2012, **116**, 10885–10897.
- [210] N. Bardin, P. Rubini and C. Madie, *ract*, 1998, **83**, 189–194.
- [211] U. Wahlgren, H. Moll, I. Grenthe, B. Schimmelpfennig, L. Maron, V. Vallet and O. Gropen, *Journal of Physical Chemistry A*, 1999, **103**, 8257–8264.
- [212] J. Neufeind, L. Soderholm and S. Skanthakumar, *Journal of Physical Chemistry A*, 2004, **108**, 2733–2739.
- [213] J. M. Génin, P. Refait, L. Simon and S. H. Drissi, *Hyperfine Interactions*, 1998, **111**, 313–318.
- [214] L. Simon, M. François, P. Refait, G. Renaudin, M. Lelaurain and J.-M. R. Génin, *Solid State Sciences*, 2003, **5**, 327–334.
- [215] L. Fanfani, A. Nunzi and P. F. Zanazzi, *American Min*, 1971, **56**, 751–757.
- [216] L. C. Basciano and R. C. Peterson, *American Mineralogist*, 2007, **92**, 1464–1473.

- [217] G. Johansson, M. Yhland, R. Dahlbom, J. Sjövall, O. Theander and H. Flood, *Acta Chemica Scandinavica*, 1962, **16**, 1234–1244.
- [218] G. Ventruti, G. D. Ventura, N. Corriero, D. Malferrari, A. F. Gualtieri, U. Susta, M. Lacalamita and E. Schingaro, *Physics and Chemistry of Minerals*, 2016, **43**, 587–595.
- [219] C. Ruby, M. Abdelmoula, R. Aissa, G. Medjahdi, M. Brunelli and M. François, *Journal of Solid State Chemistry*, 2008, **181**, 2285–2291.
- [220] M. Chen, R. Zhu, X. Lu, J. Zhu and H. He, *Inorganic Chemistry*, 2018, **57**, 7299–7313.
- [221] M. Abdelmoula, F. Trolard, G. Bourrié and J.-M. Génin, *Hyperfine Interactions*, 1998, **112**, 235–238.
- [222] S. Kerisit, *Geochimica et Cosmochimica Acta*, 2011, **75**, 2043–2061.
- [223] J.-M. R. Génin, P. Refait, G. Bourrié, M. Abdelmoula and F. Trolard, *Applied Geochemistry*, 2001, **16**, 559–570.
- [224] P. Refait, M. Abdelmoula and J.-M. Génin, *Corrosion Science*, 1998, **40**, 1547–1560.
- [225] U. Schwertmann and H. Fechter, *Clay Minerals*, 1994, **29**, 87–92.
- [226] P. Refait, C. Bon, L. Simon, G. Bourrié, F. Trolard, J. Bessière and J.-M. R. Génin, *Clay Minerals*, 1999, **34**, 499–510.
- [227] E. Dowty, *CRYSCON version 1.2.1 Shape Software*, Kingsport, USA, 2006.